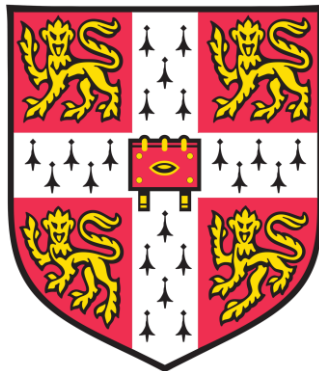


# **A Multi-functional Touch Panel for Multi- Dimensional Sensing in Interactive Displays**

October 2017

**Shuo Gao**



Department of Engineering  
**University of Cambridge**

A thesis presented for the degree of  
**Doctor of Philosophy**

# **Declaration**

I, Shuo Gao, hereby declare that I am the sole author of this thesis, and confirm that the work presented in this thesis is my own. Where information has been derived from other sources, I confirm that this has been indicated in the thesis.

**Shuo Gao**

# Abstract

This thesis presents a flexible graphene/polyvinylidene difluoride (PVDF)/graphene sandwich for three-dimensional touch interactivity. Here, an x-y plane touch is sensed using graphene capacitive elements, while force sensing in the z-direction is by a piezoelectric PVDF/graphene sandwich. By employing different frequency bands for the capacitive- and force-induced electrical signals, the two stimuli are detected simultaneously, achieving three-dimensional touch sensing. Static force sensing and elimination of propagated stress are achieved by augmenting the transient piezo output with the capacitive touch, thus overcoming the intrinsic inability of the piezoelectric material in detecting non-transient force signals and avoiding force touch mis-registration by propagated stress. As a capacitive signal is important for force touch interpretation, optimization algorithms have been developed and implemented. With correlated double sampling (CDS) and spatial low-pass filtering (SLPF) based techniques, the signal-to-noise ratio (SNR) of the capacitive touch signal is boosted by 15.6 dB, indicating improved detection accuracy. In terms of the readout speed, fixed pattern and random pattern related down-sampling techniques are applied, giving rise to reductions in both readout time (11.3 ms) and power consumption (8.79 mW).

# Acknowledgements

I would like to sincerely express my gratitude to my supervisor, Professor Arkia Nathan, who has offered me this great opportunity to work in the field of human-machine interactive systems, providing me enthusiastic guidance, encouragement and support throughout the past three-year doctoral study. His broad vision and keen scientific insight have guided me to think carefully, critically, creatively and most importantly, grow as an independent researcher.

Also, I would like to express my appreciation to all present and past members of our group, The Hetero-Genesys Laboratory, especially Dr Sungsik Lee, Dr Hanbin Ma and Mr Xiang Cheng, whose expertise were highly beneficial to this work.

Thank Cambridge Touch Technologies Ltd. (Cambridge, UK) for providing experimental touch data and access to measurement equipment and readout architectures.

Thank Chinese Scholarship Council for financially supporting my study and maintenance during my PhD.

Last but not least, I thank my parents, Jiaping Gao and Chunli Wang. Thanks for creating the best possible living conditions for me, and for supporting me both morally and financially to study at the University of Cambridge. My wife, Di Ge: thanks for choosing me, believing in me and spending the rest of your life with me. I dedicate this thesis to you.

# Table of Contents

<b>Declaration .....</b>	<b>2</b>
<b>Abstract .....</b>	<b>3</b>
<b>Acknowledgements .....</b>	<b>4</b>
<b>Table of Contents.....</b>	<b>5</b>
<b>List of Figures .....</b>	<b>8</b>
<b>List of Tables.....</b>	<b>12</b>
<b>Abbreviations.....</b>	<b>13</b>
<b>Chapter 1 Human-machine Interaction Related Technologies in Interactive Displays.....</b>	<b>14</b>
1.1 Touch Interactivity Architectures.....	15
1.2 Touch-Free Interactivity Architecture.....	17
1.3 Objectives .....	18
1.4 Thesis Outline and Contributions.....	19
Bibliography .....	21
<b>Chapter 2 Reviews on Capacitive Touchscreen and Piezoelectric Related Technologies.....</b>	<b>24</b>
2.1 A Brief Overview of Projected Capacitance Touchscreen.....	24
2.1.1 Working Principle and Panel Architecture .....	24
2.1.2 Touch Screen Construction.....	29
2.1.3 Capacitance Measurement Methods .....	30
2.1.4 Characteristics of Capacitive Touch Signals .....	32
2.2 Brief Overview of Piezoelectric Material .....	35
2.2.1 Principle and Characterization of Piezoelectric Material.....	35
2.2.2 Berlincourt Method for Piezoelectric $d_{33}$ Coefficient Measurement.....	40
2.2.3 Challenges of Piezoelectric Material Based Force Touch Detection in Interactive Displays ...	43

2.2.4 Readout Circuit for Piezoelectric Material Based Force Touch Signal .....	46
2.3 Proposed Multi-functional Touch Panel .....	50
2.4 Conclusion .....	50
Bibliography .....	54
<b>Chapter 3 Mechanical and Electrical Analysis of Interactive Stack-ups .....</b>	<b>61</b>
3.1 Mechanical Analysis of Proposed Touch Panels.....	62
3.2 Electrical Analysis of Proposed Touch Panels.....	71
3.3 Separation of Force and Capacitive Combined Touch Signals .....	75
3.4 Conclusion .....	80
Bibliography .....	83
<b>Chapter 4 Fabrication and Measurement of Multi-Functional Touch Panel.....</b>	<b>85</b>
4.1 Touch Panel Fabrication .....	85
4.2 Touch Panel Measurement .....	88
4.2.1 Capacitive Response to Human Finger Touch.....	88
4.2.2 Force Response to Machine Stylus Touch.....	90
4.3 Conclusion .....	97
Bibliography .....	98
<b>Chapter 5 Algorithms for Force Touch Signal .....</b>	<b>100</b>
5.1 Algorithms for Force Touch Interpretation .....	101
5.2 Energy Harvesting.....	108
5.2.1 Piezoelectric Based Energy Harvesting System .....	108
5.3 Conclusion .....	114
Bibliography .....	116
<b>Chapter 6 Signal Processing Algorithms for Capacitive Touch Signal Optimization .....</b>	<b>119</b>
6.1 Reduction of Common Mode Noise and Global Multi-valued Offset in Touch Screen Systems by Correlated Double Sampling.....	119

6.2 Reduction of Noise Spikes in Touch Screen Systems by Spatial Low-pass Filtering.....	131
6.3 Down-sampling Techniques for Capacitive Touch Panels.....	140
6.4 Conclusion .....	152
Bibliography .....	153
<b>Chapter 7 Conclusion.....</b>	<b>160</b>
7.1 Conclusion .....	160
7.2 Future Work .....	162
<b>Publications .....</b>	<b>163</b>
<b>Appendix I.....</b>	<b>165</b>

# List of Figures

Figure 1. 1 Interactivity based on (a) – (e): resistive, capacitive, surface acoustic wave, acoustic pulse recognition and infrared touch architectures, and (f): touch-free interactive display based on image sensor. .... 16

Figure 2. 1 (a) Multi-pad structure in self-capacitance TSP;  $P_1$  to  $P_{16}$  indicate the number of the touch pads. The yellow point represents the touch location. (b) Working principle of multi-pad structured self-capacitance TSP.  $C_{P6}$  is the capacitance between touch-pad  $P_6$  to ground and  $C_F$  is the finger touch induced capacitance. (c) Ghost points in row-and-column structured self-capacitance.  $S_{R1}$  to  $S_{R7}$  and  $S_{C1}$  to  $S_{C7}$  indicate the row and column sensing electrode 1 to 7, respectively. The yellow points and black block signs are the real touch locations and ghost points locations. .... 25

Figure 2. 2 (a) – (b) Mutual-capacitance diamond structure and bar structure. The yellow points indicate the touch locations. (c) – (d) Working principle of mutual-capacitance structure. .... 26

Figure 2. 3 (a) – (b) Working principle of mutual-capacitance structure. .... 27

Figure 2. 4 Structure of a typical two-layer projected capacitive touch panel. .... 28

Figure 2. 5 Working principles of (a) charge amplifier and (b) relaxation oscillator techniques based touch detection. .... 34

Figure 2. 6 (a) Single touch event related image and (b) multi-touch event related image. .... 36

Figure 2. 7 (a)-(b) The change of polarization in Centrosymmetric and non-Centrosymmetric structures. (c) Structure of PVDF  $\beta$ -phase, modified from [30]. .... 37

Figure 2. 8 Directions of poling and mechanical deformation. .... 39

Figure 2. 9 Main factors affecting force touch sensing in a piezoelectric material based interactive display. .... 45

Figure 2. 10 Main factors affecting force touch sensing in a piezoelectric material based interactive display. .... 47

Figure 2. 11 Equivalent circuit of piezoelectric film based force sensor. (a) current source, (b) voltage source and (c) with input resistance. .... 48

Figure 2. 12 (a) Signals from piezoelectric film and commercial force sensor. (b) Readout circuit. (c) An LED is lit by force touch induced electric power. .... 51

Figure 2. 13 Force touch signals in (a) time domain and (b) frequency domain. .... 52

Figure 2. 14 Proposed multi-functional stack-up. .... 53

Figure 3. 1 Four proposed stack-ups of touch panels (a) – (d), the electrodes are on and underneath the piezoelectric film layer. (e) Conceptual force touch event applied on one of the stack-ups.....	64
Figure 3. 2 (a) Stress vs. Displacement when thickness is 0.5mm at location L <sub>5</sub> . (b) Stress [Pa] distribution of the touch panel. In the simulation, only one layer of PVDF is used, hence the displacement contributed by normal strain is much smaller than the curvature. ....	66
Figure 3. 3 Resolution results for stackup 1: displacement and stress of stack-up 1, location L <sub>1</sub> (a) and stack-up 1, location L <sub>5</sub> (b). 0.1:0.1:1 indicates from 0.1 N to 1 N, with a step of 0.1 N. ....	68
Figure 3. 4 (a) Original touch panel. (b) Touch panel laminated with PVDF and ITO coated PET.....	69
Figure 3. 5 Voltage response of a 1N perpendicular force at the center edge of the piezo film laminated touch panel. The red point indicates the touch location. The actual contact area is 1mm <sup>2</sup> .....	71
Figure 3. 6 (a) Equivalent circuit of piezoelectric film based force sensor; (b) charge amplifier based readout circuit; (c) noise sources of the circuit and (d) input referred noise source includes all the noise sources. ....	74
Figure 3. 7 Frequency bands of force touch signal and capacitive touch signal. Block diagram of low-pass and band-pass filtering based force touch and capacitive touch signal interpretation circuit. ....	76
Figure 3. 8 Capacitive touch signal and force touch signal and their combination in time domain. ....	77
Figure 3. 9 (a) Readout circuit for force and capacitive touch signals. (b) Capacitive and force touch combined signal in time domain.....	81
Figure 3. 10 Frequency bands of force touch signal and capacitive touch signal.....	82
Figure 4. 1 (a) Fabrication process of the graphene/PVDF based multi-functional touch panel. ....	86
Figure 4. 2 Experimental results of (a) tapping touch and (b) hover touch related events. ....	89
Figure 4. 3 Experimental results of hover touch events with (a) one, (b) two, and (c) three layers of plain microscope slides. ....	91
Figure 4. 4 (a) Test-bed for force touch experiment, and (b) three-motor controlled positioning system. .	92
Figure 4. 5 Experimental results of (a) charger noise; (b) force touch signal with charger noise; (c) force touch signal after charger noise cancellation. ....	94
Figure 4. 6 Experimental results of force touch signal with “stabilized” plate.....	96
Figure 4. 7 Conceptual descriptions of touch events from different directions. ....	96
Figure 5. 1 Two issues of piezoelectric-based force touch sensing in a touch panel. (a) Static force touch is not detected. (b) Propagated stress induced charge may result in force touch mis-registration. The red circles indicate the force touch positions. The forces are static force and dynamic force in (a) and (b), respectively.....	103
Figure 5. 2 Conceptual output of the static force detection algorithm. ....	104

Figure 5. 3 Conceptual outputs of the fake force touch signal before and after the algorithm. ....	104
Figure 5. 4 Flow chart of the force detection algorithm. ....	105
Figure 5. 5 (a)–(b) System diagram and interface circuit. ....	106
Figure 5. 6 (a)–(b) Force and capacitive signals output from a single channel of the system. (c)–(d) Force and capacitive signals output from two adjacent channels of the system before the propagated stress elimination algorithm is applied. (e) Screen capture of the software. ....	107
Figure 5. 7 Conceptual piezoelectric based finger touch signal. ....	109
Figure 5. 8 (a) Single diode based rectifier circuit; (b) four diodes based bridge rectifier circuit; (c) Practical rectifier circuit. ....	110
Figure 5. 9 (a) Charging and discharging period; (b) Details of the charging period. ....	111
Figure 5. 10 (a) Circuit for force detection and energy harvesting. (b) Configuration of the touch panel, circuit, and oscilloscope. ....	113
Figure 5. 11 Simultaneous force touch signal and energy harvesting. ....	114
Figure 5. 12 Three functions in the touch panel are position detection (by capacitive sensing), force detection and energy harvesting. ....	115
Figure 6. 1 (a) Noise sources of touchscreen systems and concept of CDS algorithm. (b) The detection threshold ( $V_T$ ) is set by the highest offset value to avoid detection errors, resulting in increased power consumption. ....	120
Figure 6. 2 Images of (a) single touch, (b) multi-touch, and (c) noise pattern. Red indicates high value region. ....	121
Figure 6. 3 Conceptual outputs from an electrode of mutual capacitance TSP without and with touch. (a) Original output comprising offset and common-mode noise, and (b) the output after CDS. $V_s$ is the signal voltage and $V_{\text{offset}}$ is the offset voltage. ....	122
Figure 6. 4 Conceptual relationship between characterization factor $\alpha$ and sampling interval. ....	122
Figure 6. 5 Flowchart of the CDS based common-mode noise and global multi-valued offset reduction method. ....	125
Figure 6. 6 The touch related images before and after CDS. (a) and (c) are raw images based on one and two touch events. (b) and (d) are the CDS processed images. ....	128
Figure 6. 7 Normalized PSD plots of the original output and CDS outputs with sampling frequency at (a) 60Hz and (b) 30Hz. ....	129
Figure 6. 8 Noise in touch screen systems; the CDS based technique for common-mode noise and global multi-valued offset cancellation; noise spikes attenuation by a spatial LPF and the corresponding smoothing effect. ....	132

Figure 6. 9 Algorithm description of a spatially based average low-pass filter.....	134
Figure 6. 10 Conceptual top-view of a finger touch on a mutual row-and-column capacitance TSP. $A$ , $B_1$ to $B_4$ , $C_1$ , to $C_4$ and $N_1$ to $N_{40}$ indicate the values over the electrodes intersections. The average spatial filter is applied to the touch position pixel $A$ (left) and the adjacent pixel $B_1$ (right).....	135
Figure 6. 11 Flowchart of the CDS and spatial LPF based noise reduction algorithm.....	138
Figure 6. 12 Normalized PSD plots of the original output, CDS output with sampling frequency at 60Hz and spatial average LPF output with mask size of $3 \times 3$ . .....	139
Figure 6. 13 Four Gaussian distribution based masks with different bandwidths (represented by standard deviations). (a) $\sigma = 0.5$ ; (b) $\sigma = 1$ ; (c) $\sigma = 2$ ; (d) $\sigma = 4$ . .....	139
Figure 6. 14 Results of signal and noise spike attenuation by applying spatial LPFs with different standard deviations. (b) is the dashed part of (a).....	141
Figure 6. 15 Merits and drawbacks of the down-sampled signal, and compressive sensing based fast readout technique. ....	142
Figure 6. 16 (a) The distance from one pixel $(i,j)$ to other pixels (e.g. $(i+1, j+1)$ )can be expressed by Euclidean distance. The unit of the distance is pixel. (b) Regional scan method for the multi-pad capacitance TSP. Red pads will be scanned rapidly after the reconstruction. The yellow point is the reconstructed touch position. ....	143
Figure 6. 17 Flowchart of the down-sampling based fast readout technique. ....	144
Figure 6. 18 (a) Original signal; (b), (c) and (d) are reconstructed signals with 50%, 30% and 10% of original electrode pads.....	146
Figure 6. 19 (a) Distribution of the reconstructed touch positions; X-Y coordinates indicate the distance between the reconstructed touch position and original touch position. (b) The cross-section with the largest variance of (a). ....	147
Figure 6. 20 (a) original swipe touch based frame, (b) down-sampled touch signal, (c) reconstructed touch signal by using low-pass spatial filtering, (d) regional scanned touch signal.....	150
Figure 6. 21 (a) Distribution of the reconstructed touch positions; X-Y coordinates indicate the distance between the reconstructed touch position and original touch position. (b) The cross-section with the largest variance of (a). ....	151

# List of Tables

Table 2. 1 Main Distinctions between self-capacitance and mutual-capacitance structures, modified from [2]-[6]. .....29

Table 2. 2 Main Distinctions between self-capacitance and mutual-capacitance structures, modified from [2][3]...... 31

Table 2. 3 Symbols and meanings of different stack-ups, modified from [6]. ..... 31

Table 2. 4 Estimators for sub-pixel interpolation, modified from [28].  $r_i$  indicates the capacitance value at the  $i$ th row..... 33

Table 2. 5 Definitions of  $d$  and  $g$  in direct effect and converse effect. .... 38

Table 3. 1 Dimension parameters of the proposed stack-ups. .... 63

Table 3. 2 Mechanical and piezoelectrical properties of the proposed stack-ups. [4]-[7] ..... 63

Table 4. 1 Conceptual descriptions of touch events from different directions. .... 97

Table 5. 1 Truth table of force and capacitive touch signals. .... 105

Table 6. 1 The ranges of characterization factor  $\alpha$  and corresponding implications.  $f_S$  and  $f_H$  are the sampling frequency and waveform frequency, respectively. In reality,  $f_H$  is the highest noise frequency within a system's noise bandwidth. If the system is a one-pole low-pass filter,  $f_H = (\pi/2)f_{3dB}$ , where  $f_{3dB}$  is system's -3dB bandwidth. .... 124

Table 6. 2 Parameters of the test bed..... 124

Table 6. 3 Relationship between sampling percentage and regional scan range. .... 148

# Abbreviations

TSP	Touchscreen Panel
PVDF	Polyvinylidene fluoride
DC	Direct Current
AC	Alternating Current
PET	Polyethylene terephthalate
SNR	Amorphous Silicon
LPF	Low Pass Filtering
CS	Compressive Sensing
CVD	Chemical Vapor Deposition
CDS	Correlated Double Sampling
PD	Photon Detector
ITO	Indium Tin Oxides
KEITHLEY	The Company Name on the Semiconductor Analyzer
LCD	Liquid Crystal Displays
OLED	Organic Light Emitting Diodes
TFT	Thin Film Transistor
HMI	Human Machine Interactivity/Human Machine Interface
OSA	Optical Clearance Adhesive
DSP	Digital Signal Processing
EMI	Electro-magnetic Interference
Op-amp	Operational Amplifier
TIA	Transimpedance Amplifier

# Chapter 1 Human-machine Interaction

## Related Technologies in Interactive Displays

---

Visual display of information is an obvious requirement in today's highly digital world, and constitutes a powerful means of conveying complex information. This stems from the ability of the human eye and brain to perceive and process vast quantities of data in parallel. The history of visualizing information can be traced to the ancient era, when our ancestors carved images on cave walls and monuments (around 30000 BC [1]). Mosaic art form emerged in the 3rd millennium BC [2], using small pieces of glass, stone, or other materials in combination to display information. These pieces are similar to pixels in the modern electronic display. The electronic display has become the primary human-machine interface in most applications, ranging from mobile phones, tablets, laptops, and desktops to TVs, signage and domestic electrical appliances, not to mention industrial and analytical equipment.

In the meantime, user interaction with the display has progressed significantly. Through sophisticated hand gestures [3]-[11], the display has evolved to become a highly efficient information exchange device. While interactive displays are currently very popular in mobile electronic devices such as smart phones and tablets, the development of large-area, flexible electronics, offers great opportunities for interactive technologies on an even larger scale. Indeed, technologies that were once considered science fiction are now becoming a reality; the transparent display and associated smart surface being a case in point. These technologically significant developments beg the question, "What will be the development trend of interactive technology?" This chapter will review

current mainstream interactivity techniques and predict what we believe will be future interactive technologies. This section will first review current mainstream interactivity techniques, and then predict the future trend of interactive display. Based on the review and the prediction, the motivation and contribution of this dissertation are provided.

Human-machine interactivity can be categorized based on touch or touch-free gestures. The former is primarily employed in the small and medium-scale screens used in smart phones and tablets, while the latter is more popular in larger displays [12]. Various techniques for interactivity have been developed. Currently these are mainly based on resistive, capacitive, surface acoustic wave, acoustic pulse recognition and infrared schemes [3]. Recently, touch-free (e.g. gesture recognition by optical imaging) and force-touch have emerged and are now in commercial devices. These advanced features bring human-machine interactivity to a new level of user experience.

## **1.1 Touch Interactivity Architectures**

The first generation of touch screens employed resistive based architectures [4], in which two transparent electrically resistive layers are separated by spacer dots and connected to conductive bars in the horizontal (x-axis) and the vertical (y-axis) sides, respectively. A voltage applied on one layer can be sensed by the other layer, and vice versa. When the user touches the screen, the two layers are connected at the touch point and work as voltage dividers, and the touch location is then calculated. These first generation devices were limited to locating a single point, restricting their use for complex gestures.

In capacitive-based touch panels, electrodes are arranged as rows and columns and are separated by an insulating material such as glass or thin film dielectric. When a conductive object comes in contact with the screen surface, the electric field is perturbed hence changing the capacitance between electrodes [5][6]. Capacitive touch

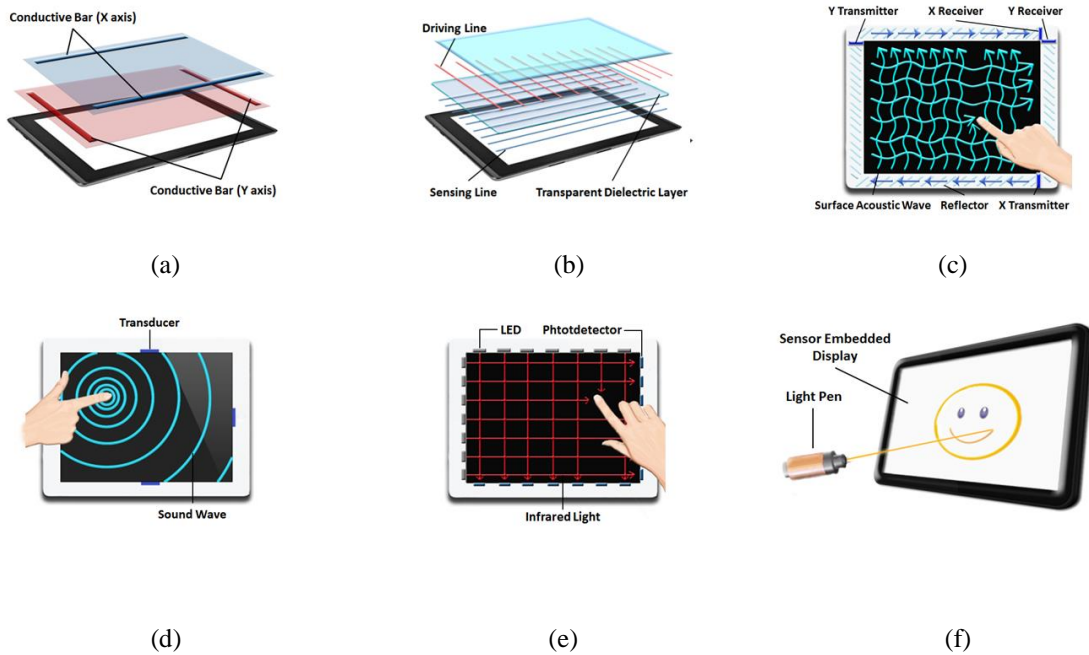


Figure 1. 1 Interactivity based on (a) – (e): resistive, capacitive, surface acoustic wave, acoustic pulse recognition and infrared touch architectures, and (f): touch-free interactive display based on image sensor.

panels are most commonly used in smart phones because they support multi-touch without altering the visibility and transparency of the display.

In surface acoustic wave and acoustic pulse recognition interactivity schemes, the touch position is detected by acoustic waves [7][8]. In the former, ultrasonic waves are transmitted and reflected in the x- and y-directions. By measuring the touch-induced absorption of the waves, the location can be determined. In acoustic pulse recognition, transducers are fitted at the edges of the touch panel. A touch action on the screen surface generates a sound wave that is then detected by the transducers, digitalized and subsequently processed to determine the touch position.

In the infrared-based architecture, two adjacent sides of a touch screen are equipped with light emitting diodes, which face photodetectors on the opposite sides, forming an

infrared grid pattern [9][10]. The touch object (e.g. finger or stylus) disrupts the grid pattern, from which the touch location is determined.

The techniques described above detect two-dimensional single- or multi-touch, i.e. touch locations on an x-y plane. Recently, commercial products released by Apple support force sensing, expanding touch interactivity to 3-D [11]. Here, screen deflection, and hence the corresponding change in capacitance, serves as a measure of the extent of applied force, which is then augmented with a haptic response.

## **1.2 Touch-Free Interactivity Architecture**

Whilst a variety of touch technologies are currently in use in products, touch-free gesture recognition has emerged recently. One current technique relies on locating discrete infrared sources and detectors at different positions on the display edges to construct the touch event. However, imaging is not possible because of the discrete nature of the sensors. The pixelated approach reported recently employs an image sensor integrated at every display pixel. This way the display is actually able to view the underlying gestures of the user. Alternately the event can be remotely triggered by a light pen [13-17]. The interactive display can be transparent using, e.g. oxide semiconductor technology, and be able to carry out invisible image capture. This development has the potential for high technological impact in human interfaces.

Voice recognition is another technique for remote interactivity [18]. Tremendous progress has been made in this area with very impressive results. Existing commercial products include Siri and Echo from Apple and Amazon respectively. Despite that, challenges remain in voice signal processing and machine limitations of speech perception. This is particularly true with differently spelled but similar sounding words, and signal recognition in a noisy acoustic background. These problems can be eventually overcome with use of much faster processors and more memory to bring into consideration contextual information.

### **1.3 Objectives**

Current mainstream human-machine interactive (HMI) technology-touch screen panel (TSP) has two shortcomings. First, recent TSPs employ a single sensing technique to detect one certain type of physical signal (one-dimensional sensing), as explained above and illustrated in Fig. 1.1 (a)–(f). Thus, multiple discrete devices with different sensing capabilities must be embedded into a single system to allow multi-dimensional sensing. For example, optical, temperature and force sensors are integrated into commercial mobile phones to provide multi-dimensional signal detection functions for customers. However, this results in increased component costs, circuitry complexity and power consumption. Second, although the energy cost is tiny for the individual touch sensors in a TSP, their total energy consumption is huge considering numerous touch panels are intensively used worldwide. Besides optimizing the product design to reduce power consumption, which approaches the limits of current technology, harvesting the environmental energy is essential to enhance the lifetime of the battery.

Thus, in this project, the key task is to design and implement a multi-functional TSP prototype for multi-dimensional sensing along with possible applications to energy harvesting. First, multi-dimensional signals must be detected concurrently, providing customers with a similar user experience to when multiple mono-dimensional sensors are used. Second, since TSP is a highly commercialized product, the proposed technique should well fit to existing TSP techniques, to avoid/reduce changes to production lines. Third, potential issues of the proposed technique need to be analyzed and addressed.

To achieve these objectives, functional materials must first be employed. More specifically, piezoelectric materials will be used, due to their intrinsic ability of converting mechanical stress to electric charges, providing the functions of force touch detection and energy harvesting. Second, the piezoelectric materials will be combined

with capacitive touch panels, which dominate the TSP market [19]. Third, algorithms on how to interpret these two signals will be developed.

## **1.4 Thesis Outline and Contributions**

This thesis charts the author's work on the understanding of capacitive TSP and piezoelectric materials, and the development of a multi-functional touch panel from theoretical analysis to touch panel fabrication and algorithm design. Chapter 2 provides literature reviews on capacitive touch panel and piezoelectric materials. The multi-functional touch panel for concurrently sensing force and capacitive stimuli is proposed at the end of this chapter. In Chapter 3, a theoretical analysis is conducted of the proposed technique in mechanical and electrical terms. Secondly, preliminary experiments are performed for the purpose of validating the concept. The proposed multi-functional touch panel is fabricated and measured in Chapter 4. The experimental results demonstrate its good mechanical and electric response to touch events. Chapter 5 focuses on design and implementation of the algorithm for interpreting the force touch signal. Two practical issues facing force touch sensing are first addressed with the help of the capacitive touch signal: static force touch detection and stress propagation. Second, an algorithm is developed to achieve concurrent force touch detection and energy harvesting. As the capacitive touch signal is vital for interpreting the force touch signal, its detection accuracy and readout speed must be improved. In Chapter 6, noise reduction and fast readout related techniques are developed. Finally, The conclusions, technological outlook and planned future work are described in Chapter 7.

The novel contributions of this thesis can be summarised as follows:

- A simple structured multi-functional touch panel system for concurrent multi-dimensional sensing is demonstrated for the first time.
- Mechanical analysis and experiments are given for a piezoelectric material based touch panel. First, we provide a possible means for achieving high sensitivity in force touch detection in an interactive display. Second, the challenges of using

piezoelectric materials are analyzed, such as detection uniformity across the panel.

- Interpretation algorithms are proposed and implemented for static force touch detection and elimination of force touch interference.
- A smart algorithm is proposed and implemented for obtaining force touch detection and energy harvesting at the same time.
- Image based noise reduction and fast readout techniques are developed for capacitive touch signals. Correlated-double sampling and spatial low-pass filtering based techniques are employed to reduce the noise power. Down-sampling techniques with fixed and random patterns are used to speed up the readout.
- The above contributions have been reported in a series of peer-reviewed IEEE and ACS publications.

## Bibliography

- [1] Chauvet, J.M., Brunel Deschamps, E. and Hillaire, C., 1996. *Dawn of art: the Chauvet Cave: the oldest known paintings in the world*. HN Abrams.
- [2] Aruz, J. and Wallenfels, R., 2003. *Art of the First Cities: the Third Millennium BC from the Mediterranean to the Indus*. Metropolitan Museum of Art.
- [3] Walker, G., 2012. A review of technologies for sensing contact location on the surface of a display. *Journal of the Society for Information Display*, 20(8), pp.413-440.
- [4] Colwell Jr William, C., Elographics Inc, 1975. *Discriminating contact sensor*. U.S. Patent 3,911,215.
- [5] Barrett, G. and Omote, R., 2010. Projected-capacitive touch technology. *Information Display*, 26(3), pp.16-21.
- [6] Johnson, E.A., 1965. Touch display--a novel input/output device for computers. *Electronics Letters*, 1(8), pp.219-220.
- [7] Adler, R. and Desmares, P.J., 1987. An economical touch panel using SAW absorption. *IEEE transactions on ultrasonics, ferroelectrics, and frequency control*, 34(2), pp.195-201.
- [8] North, K. and D Souza, H., 2006. Acoustic pulse recognition enters touch-screen market. *Information Display*, 22(12), p.22.
- [9] Cohen, N., 2011. Timeline: a history of touch-screen technology. *National Public Radio. Natl. Public Radio*, 26.

- [10] Butler, A., Izadi, S. and Hodges, S., 2008, October. SideSight: multi-touch interaction around small devices. In *Proceedings of the 21st annual ACM symposium on User interface software and technology* (pp. 201-204). ACM.
- [11] Raymudo, O. 2015, 13th October. Iphone 6S display teardown reveals how 3D touch sensors actually work. *Message posted to Macworld*.
- [12] Nathan, A. and Gao, S., 2016. Interactive Displays: The Next Omnipresent Technology [Point of View]. *Proceedings of the IEEE*, 104(8), pp.1503-1507.
- [13] Jeon, S., Ahn, S.E., Song, I., Kim, C.J., Chung, U.I., Lee, E., Yoo, I., Nathan, A., Lee, S., Ghaffarzadeh, K. and Robertson, J., 2012. Gated three-terminal device architecture to eliminate persistent photoconductivity in oxide semiconductor photosensor arrays. *Nature materials*, 11(4), pp.301-305.
- [14] Ahn, S.E., Song, I., Jeon, S., Jeon, Y.W., Kim, Y., Kim, C., Ryu, B., Lee, J.H., Nathan, A., Lee, S. and Kim, G.T., 2012. Metal oxide thin film phototransistor for remote touch interactive displays. *Advanced materials*, 24(19), pp.2631-2636.
- [15] Jeon, S., Ahn, S.E., Song, I., Jeon, Y., Kim, Y., Kim, S., Choi, H., Kim, H., Lee, E., Lee, S. and Nathan, A., 2011, December. Dual gate photo-thin film transistor with high photoconductive gain for high reliability, and low noise flat panel transparent imager. In *Electron Devices Meeting (IEDM), 2011 IEEE International* (pp. 14-3). IEEE.
- [16] Jeon, S., Park, S., Song, I., Hur, J.H., Park, J., Kim, H., Kim, S., Kim, S., Yin, H., Chung, U.I. and Lee, E., 2010. Nanometer-scale oxide thin film transistor with potential for high-density image sensor applications. *ACS applied materials & interfaces*, 3(1), pp.1-6.

- [17] Lee, S., Jeon, S., Chaji, R. and Nathan, A., 2015. Transparent semiconducting oxide technology for touch free interactive flexible displays. *Proceedings of the IEEE*, 103(4), pp.644-664.
- [18] Hua, Z. and Ng, W.L., 2010, November. Speech recognition interface design for in-vehicle system. In *Proceedings of the 2nd International Conference on Automotive User Interfaces and Interactive Vehicular Applications* (pp. 29-33). ACM.
- [19] Romero, C. The Technology of Touch Screens - Part 2. Available online: <https://www.linkedin.com/pulse/20140711010513-103266825-the-technology-of-touch-screens-2>.

# **Chapter 2 Reviews on Capacitive Touchscreen and Piezoelectric Related Technologies**

---

In the previous section, the need for a simple-structured multi-functional touch panel was explained, along with the design requirements of the multi-functional touch panel. In order to develop a piezoelectric material based capacitive touch panel, it is necessary to develop an understanding of the capacitive touch panel and piezoelectric materials

In this section, brief literature reviews are provided first in terms of the working principles of projected capacitive touch panels and piezoelectric materials. Following this, the design considerations of embedding piezoelectric material into capacitive touch panels are given through theoretical analysis and practical experiments. Finally, a multi-layered stack-up is proposed to achieve multi-functionality.

## **2.1 A Brief Overview of Projected Capacitance Touchscreen**

### **2.1.1 Working Principle and Panel Architecture**

Projected capacitance touchscreen system measures the change of capacitance at electrodes to detect the touch event [1][2]. When a conductive object (human figure or stylus) touches the screen, the original electromagnetic field will be affected hence the capacitance is changed. This can be sensed by electrodes as a signal and sent to the processor to determine the touch location. Two options are provided here, self-capacitance and mutual capacitance.

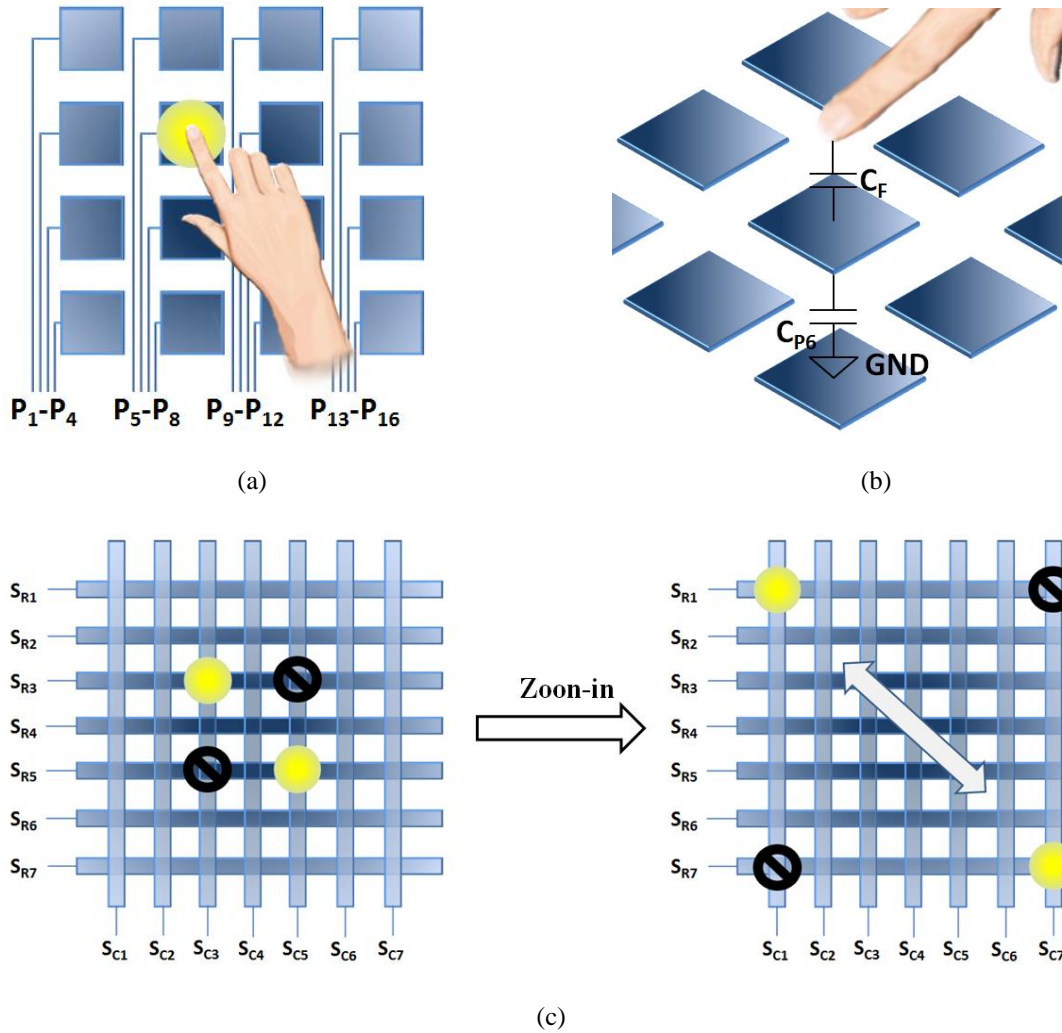


Figure 2. 1 (a) Multi-pad structure in self-capacitance TSP;  $P_1$  to  $P_{16}$  indicate the number of the touch pads. The yellow point represents the touch location. (b) Working principle of multi-pad structured self-capacitance TSP.  $C_{P6}$  is the capacitance between touch-pad  $P_6$  to ground and  $C_F$  is the finger touch induced capacitance. (c) Ghost points in row-and-column structured self-capacitance.  $S_{R1}$  to  $S_{R7}$  and  $S_{C1}$  to  $S_{C7}$  indicate the row and column sensing electrode 1 to 7, respectively. The yellow points and black block signs are the real touch locations and ghost points locations.

In self-capacitance TSP, the capacitance between electrodes to ground is measured [3][4][5][6]. When a human finger is close to the electrode, the capacitance between the electrode to the ground is increased, hence a touch event is detected. Two types of self-capacitance are constructed, which are multi-pad and row-and-column [4] as shown in

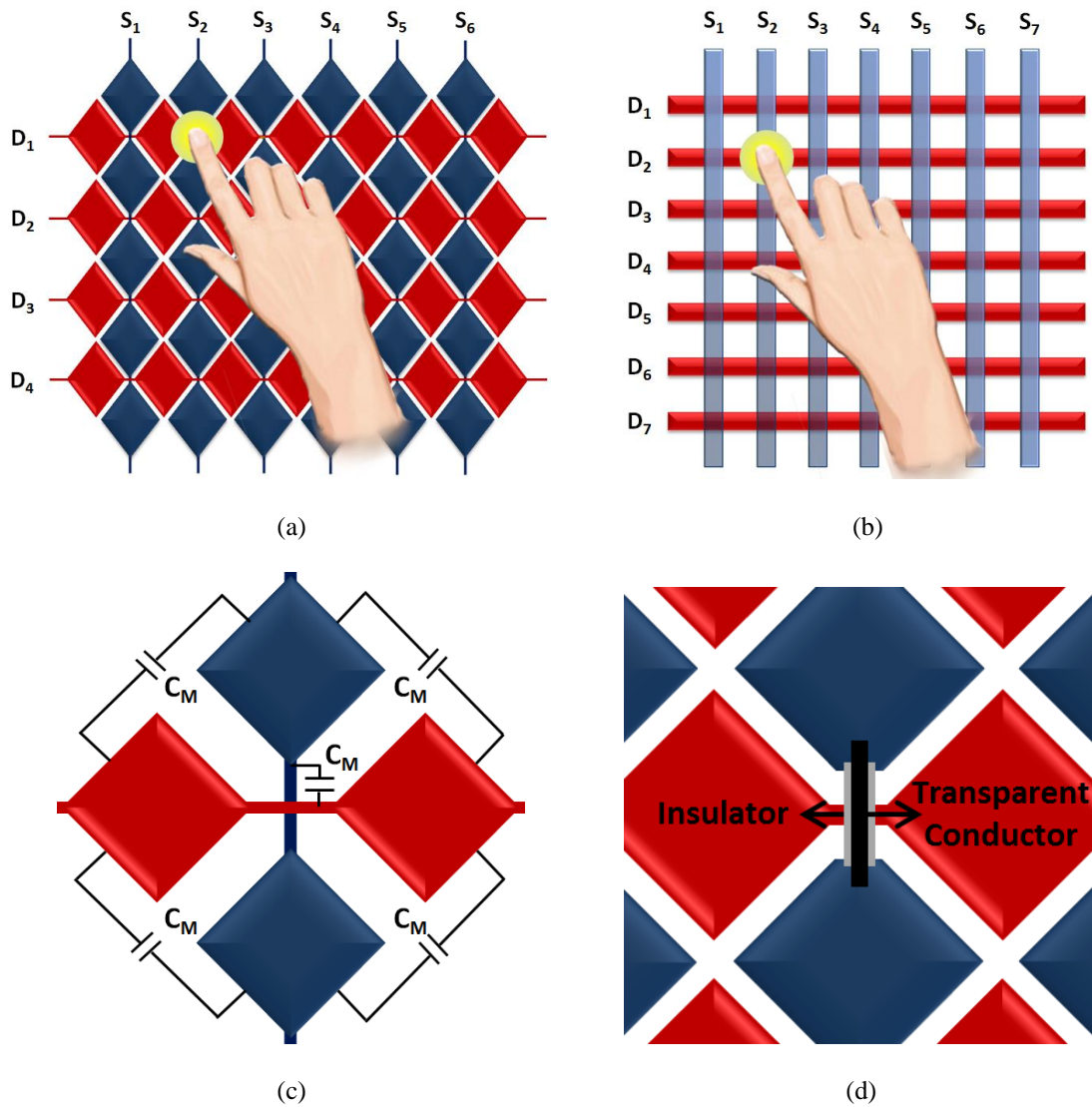
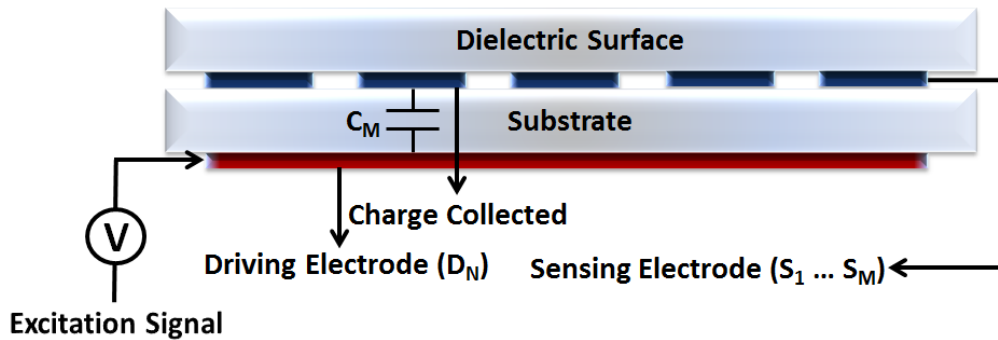
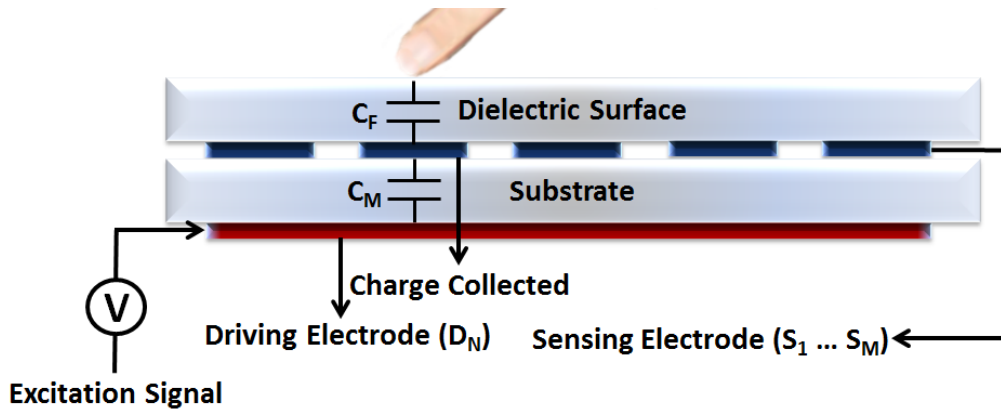


Figure 2. 2 (a) – (b) Mutual-capacitance diamond structure and bar structure. The yellow points indicate the touch locations. (c) – (d) Working principle of mutual-capacitance structure.

Fig. 2.1. In a multi-pad structure, each pad is connected with the controller individually, thus multi-touch is supported. In a row-and-column structure, each of the rows and columns is an electrode, instead of a pad as in a multi-pad structure, and individually connected with the processor. Although each intersection of rows and columns indicates a unique location on touch screen, it cannot support multi-touch. This is because each electrode is measured, instead of each intersection. Thus when multi-touch is



(a)



(b)

Figure 2. 3 (a) – (b) Working principle of mutual-capacitance structure.

performed, ghost points are made as illustrated in Fig. 2.1 (c). However, zoom-in/zoom-out function still works, as the distances between the interpreted touch locations are calculated by software. When the distance increases, a zoom-in action can be interpreted. In contrast, a decrement of distance between registered touch locations indicates a zoom-out action. One advantage of the self-capacitance structure is its ability in detecting hover touch and glove touch, since long-distance field projection is normally used [6].

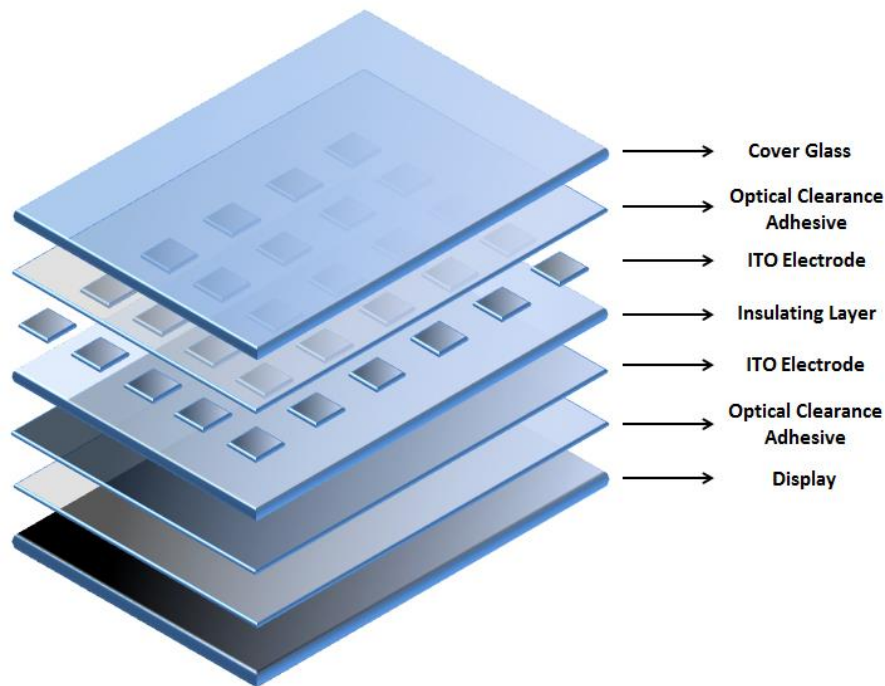


Figure 2. 4 Structure of a typical two-layer projected capacitive touch panel.

Alternatively, in mutual-capacitance TSP, the mutual capacitance between two electrodes is measured [6][7]. In mutual capacitance, electrodes are normally placed as rows and columns [7]. Electrodes in rows work as driving lines and those in columns act as sensing lines, or vice versa. Each intersection of rows and columns represents a unique location, and each intersection will be measured individually. By periodically the scanning electrodes' intersections, multi-touch is supported. As shown in Fig. 2.2, electrodes in rows are arranged from  $D_0$  to  $D_N$ , after each of them is powered separately, the intersections with the sensing lines from  $S_1$  to  $S_M$  will be measured in sequence to realize multi-touch detection. When a human finger touches the panel cover, the mutual capacitance is decreased, as charges are stolen by the human finger. One obvious drawback of mutual-capacitance TSP is that more time is needed for a full screen measurement compared with that of the self-capacitance TSP. Current commercial products have a sensing rate from 20Hz to 200Hz [2], while some lab-used and

developed touch panels can achieve higher sensing rate, up to 6400Hz [8]-[15].

<b>Characteristic</b>	<b>Self-Capacitance</b>	<b>Mutual-Capacitance</b>
<b>Electrode Type</b>	Sensing	Driving and Sensing
<b>Number of Layers</b>	1 or 2	1 or 2
<b>Electrode Design</b>	Multi-pad/ Row-and-Column	Any design with unique electrode intersections
<b>Scanning Method</b>	Each electrode	Each electrode intersection
<b>Whole Panel Scanning Time</b>	⌘	⌘⌘
<b>Measured capacitance</b>	Capacitance of electrode to ground	Capacitance between electrodes
<b>Ghost point</b>	Yes for Row-and- Column Structure	No
<b>EMI Robustness</b>	Bad	Good

Table 2. 1 Main Distinctions between self-capacitance and mutual-capacitance structures, modified from [2]-[6].

The main distinctions between self-capacitance and mutual-capacitance structures are summarized in Table 2.1.

### 2.1.2 Touch Screen Construction

Almost all the projected capacitive touch screens share two basic features in their construction [6]. First the touch surface is above the sensing circuits, and second all the components are fixed which means no moving part. A typical two layers projected capacitance construction concept is shown in Fig. 2.4. Two transparent thin-film ITO conductors are separated by a thin-film insulator (normally glass or PET), and a touch surface is set on top of them.

The sheet resistance and line widths of the patterned ITO layer are normally  $150 \Omega/\square$  and  $20\mu\text{m}$ , when glass is used as substrate [2]. In contrast, when PET is employed as a substrate, the line widths are typically  $100\text{-}200 \mu\text{m}$  [2], due to the reduced flatness compared to glass. For glass substrate related ITO patterning, photolithographic

methods are widely used. As to the PET substrate, more techniques can be applied for ITO patterning, such as screen-printing [2]. Although the sheet resistance and line widths of the PET substrate based patterning are higher and larger than those of the glass substrate based patterning. The advantage of using a PET substrate is its thinness. The thickness of a PET substrate is usually from 50  $\mu\text{m}$  to 100  $\mu\text{m}$  [2][3][16][17]. Alternatively, glass substrate's thickness is from 0.2 mm to 0.4 mm [2][3]. The detailed comparison of a PET substrate vs. glass substrate is given in Table 2.2. Optical clearance adhesive (OCA) is widely used to glue the multi-layered structure [2][6].

Besides the stack-up shown in Fig. 2.3, there are many other stack-ups widely used in industry. The reasons for touch-module makers to select one but not others are based on the considerations such as transmissivity, thickness, weight and cost. The symbols and meanings for different stack-ups are summarized in Table 2.3.

### **2.1.3 Capacitance Measurement Methods**

Capacitance can be measured by a variety of methods. In general, touch induced capacitance can be detected by measuring the change of RC constant, impedance and amount of transferred charges. The main methods are relaxation oscillator [18], charge time vs voltage [19], voltage divider [20] and charge transfer [21]. Among them, the details of relaxation oscillator based and transferred charge based methods are discussed in this section.

In transferred charge based methods, a current source (or a voltage source) is employed to provide a stable periodic signal [22]. As shown in the black components in Fig. 2.5 (a), by integrating the charges accumulated on the electrode capacitor ( $C_{\text{Electrode}}$ ), the charge amplifier consisted of an operational amplifier and feedback components (feedback resistor  $R_F$  and feedback capacitor  $C_F$ ) outputs a voltage signal ( $V_{\text{Out}}$ ). The amplitude of the output is positively proportional to the ratio of the  $C_{\text{Electrode}}$  to the  $C_F$ . When a touch event happens, a touch induced capacitor ( $C_{\text{Touch}}$ ) is paralleled to the

<b>Characteristic</b>	<b>PET</b>	<b>Glass</b>
<b>Glass Transition Temperature</b>	70 °C	570 °C
<b>Aging Effects</b>	Yellowing, curling, surface deformation	No known effect
<b>Transparency</b>	85%	=>90%
<b>Resolution</b>	10-30 µm	1 µm
<b>Stack-up</b>	Thinner	Thicker
<b>Weight</b>	Lighter	Heavier
<b>Lamination Yield</b>	Excellent	Good
<b>Cost</b>	\$\$ (was < glass)	\$

Table 2. 2 Main Distinctions between self-capacitance and mutual-capacitance structures, modified from [2][3].

<b>Symbol</b>	<b>Meaning</b>
<b>(G)</b>	Cover-glass (or plastic)
<b>G</b>	Cover glass or sensor glass with ITO on one side, or plain glass for film lamination
<b>GG</b>	Cover glass + one sensor glass
<b>GGG</b>	Cover glass + two sheets of sensor glass
<b>G#</b>	# = Number of ITO layers on one side of sensor glass
<b>G1F</b>	F = Sensor film with ITO on one side, laminated to glass
<b>GFF</b>	FF = Two sensor films, laminated to glass
<b>GF#</b>	1. Two ITP layers on one side of sensor film, laminated to glass (also called GF-Single) 2. One ITO layer on each side of sensor-film, laminated to glass (also called GFxy with metal mesh)
<b>SITO</b>	ITO on one side of substrate (single-sided); usually includes metal bridges for Y to cross X
<b>DITO</b>	ITO on both sides of substrate

Table 2. 3 Symbols and meanings of different stack-ups, modified from [6].

original electrode capacitor ( $C_F$ ), as shown in the grey components in Fig. 2.5 (a). Thus the input capacitance increases, resulting in a boost in the output voltage. In this way, a touch event is detected.

As to the relaxation oscillator based capacitance measurement, a non-linear electronic circuit is used to generate a periodic non-sinusoidal (e.g. triangular wave or square wave) signal. As shown in the black components in Fig. 2.5 (b), through the feedback resistor ( $R_F$ ), the input capacitor ( $C_{\text{Electrode}}$ ) is charged. When the voltage across the input capacitor  $C_{\text{Electrode}}$  exceeds a certain threshold, the inverter is triggered, and then the output becomes zero. This process happens periodically, and the period is controlled by the feedback resistor  $R_F$  and input capacitor  $C_{\text{Electrode}}$ . When a touch event happens, the touch induced capacitor  $C_{\text{Touch}}$  increases the RC constant, hence decreases the frequency of the output signal, as shown in grey part of Fig 2.5 (b).

#### **2.1.4 Characteristics of Capacitive Touch Signals**

To accurately interpret capacitive touch signals in terms of position and presence, and avoid touch mis-registrations, digital signal processing (DSP) algorithms [7][23][24] are normally applied to the digitized touch signals. To design and implement high efficiency DSP algorithms, the first thing to consider should be the capacitive touch signal's characteristics. In practice, the characteristics of the touch signals are different case by case. They are highly dependent up on the structure of the touch panel, measurement methodology, environmental noise and user behaviour. However, there are still some shared factors for most of capacitive touch signals. Below we provide a detailed analysis on the shared human finger touch signal characteristics of mutual-capacitance architecture, which is intensively used in current commercial mobile phones.

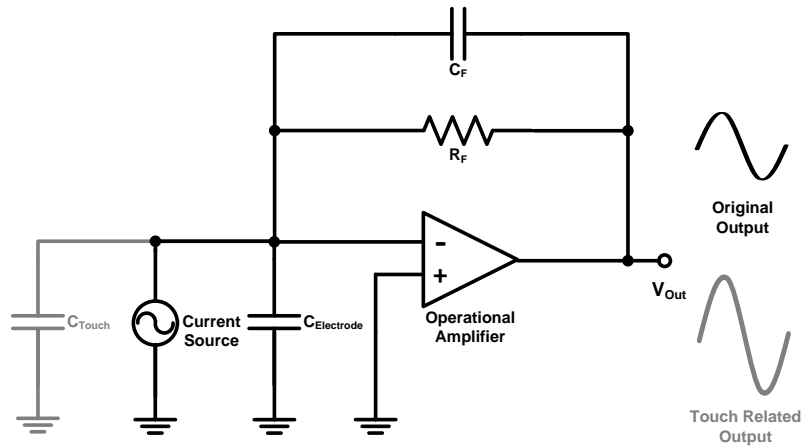
The property analysis of capacitive touch signals can be based on a single electrode intersection or a whole scan of touch panel. If the capacitance value of each electrode intersection is assumed as a pixel value, and the data associated with a whole scan of the

touch panel is treated as an image, then the property analysis is equivalent to the analysis on a touch event related pixel and a touch event related image. Time domain analysis is widely applied on the touch event related pixel [7][23]. In the time domain, human touch is a low frequency signal, whose bandwidth is normally below 10 Hz [7]. Based on this property, many low-pass filtering based techniques [7][25] are applied to remove noise, in order to improve signal to noise ratio (SNR).

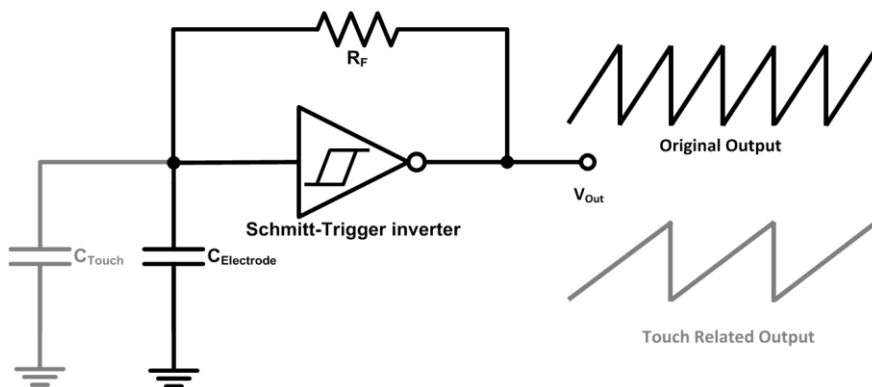
As to the analysis on the touch event related image, spatial domain analysis is performed. In spatial domain, first touch signals are viewed as low spatial frequency signals [24]. This is because the size of the human finger is normally 7mm to 15mm, and traditionally, spacing of two adjacent electrode intersections is around 5mm [26]. When a finger touch is performed, normally 3×3 electrode intersections are affected [27]. As the spacing in recent touch panels is becoming smaller and smaller, more electrode intersections are affected. In our experiment carried out with an 80×80 Blackberry lab touch panel, the spacing for sensing array is only 2mm, thus more electrode intersections (~11×11) are affected as shown in Fig. 2.6. Within the touch event affected region, the capacitance values of adjacent electrode intersections are similar; hence the touch signal offers a low spatial character. This character is important for smoothing noise spikes.

<b>Estimator</b>	<b>Equation</b>
<b>Gaussian</b>	$\frac{1}{2} \frac{\ln r_{i-1} - \ln r_{i+1}}{\ln r_{i-1} - 2 \ln r_i + \ln r_{i+1}}$
<b>Center of Mass</b>	$\frac{r_{i+1} - r_{i-1}}{r_{i-1} + r_i + r_{i+1}}$
<b>Linear</b>	$\frac{r_{i+1} - r_{i-1}}{r_i - \min\{r_{i-1}, r_{i+1}\}}$
<b>Parabolic</b>	$\frac{r_{i-1} - r_{i+1}}{r_{i-1} - 2r_i + r_{i+1}}$

Table 2. 4 Estimators for sub-pixel interpolation, modified from [28].  $r_i$  indicates the capacitance value at the  $i$ th row.



(a)



(b)

Figure 2. 5 Working principles of (a) charge amplifier and (b) relaxation oscillator techniques based touch detection.

Second, the capacitance intensities of electrode intersections within the touch affected area follow a certain distribution (e.g. Gaussian) [26][27][28]. This is due to the shape of the human finger. Various sub-pixel interpolation algorithms [24][27] for detecting accurate touch positions are developed based on this characteristic. Some widely used subpixel estimators are summarized in Table 2.4. Furthermore, algorithms for avoiding

mis-touch registrations are also based on this characteristic. For example, when a user's cheek touches the touch panel, although the capacitance intensity exceeds the touch determination threshold, the cheek touch activity is not registered due to its intensity distribution; hence an important phone call will not be disturbed by a user's unintentional operations.

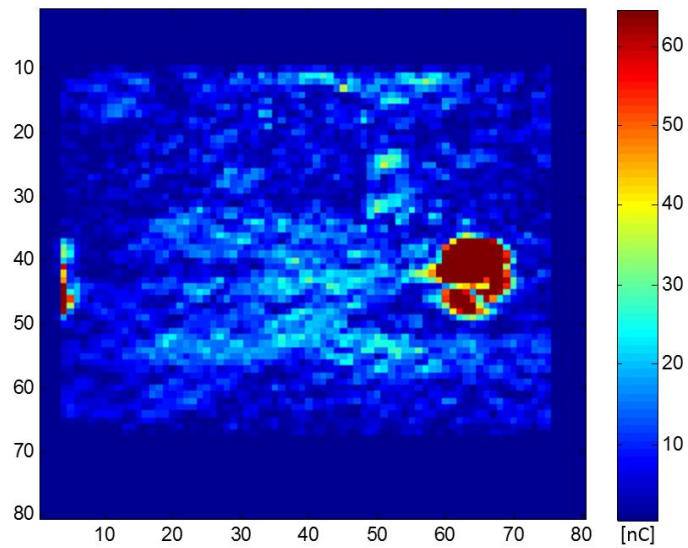
Third, touch signals also exhibit sparse property (only limited number of touch signals exist simultaneously) in the spatial domain [24][29]. Under practical situations, only one or two touch events happen simultaneously. In fact, although a touch panel scans all its electrode intersections periodically, it normally only supports a few touch events during one scan period. For example, by employing a multi-touch testing software (MultiTouch), we learn that iPhone 6S and iPad Pro can support 5 and 17 simultaneous touch events, respectively.

## **2.2 Brief Overview of Piezoelectric Material**

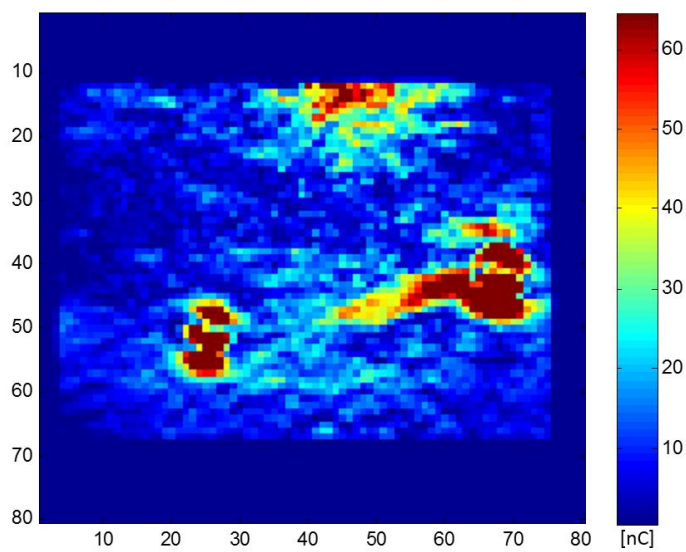
### **2.2.1 Principle and Characterization of Piezoelectric Material**

Piezoelectricity is the phenomenon by which charges are generated in some solid materials when mechanical stress is applied [30][31]. It was first demonstrated in 1880 by C. Linnaeus and F. Aepinus. The working principle of piezoelectric materials is based on their non-centrosymmetric structures. [32] When a load force is applied to a centrosymmetric material, its polarization remains intact. In contrast, the polarization of a non-centrosymmetric material becomes either positive or negative according to the direction of the applied force, inducing a charge in the material. This is illustrated in Fig. 2.7 (a)-(b). The structure of a specific piezoelectric material, PVDF in its  $\beta$ -phase, is shown in Fig. 2.7 (c) to provide a direct view of how the polarization changes due to the structure of the material. Piezoelectric materials also demonstrate the inverse piezoelectric phenomenon, in which a mechanical deformation is induced when an external electric field is applied [33]. The phenomenon of force induced charge is a designated direct effect, and its counterpart is known as the motor effect [33]. To

quantify piezoelectric performance, piezoelectric equations and coefficients can be used. The piezoelectric equations and coefficients are summarised below. The measurement of the main coefficient is discussed in the next section.



(a)



(b)

Figure 2. 6 (a) Single touch event related image and (b) multi-touch event related image.

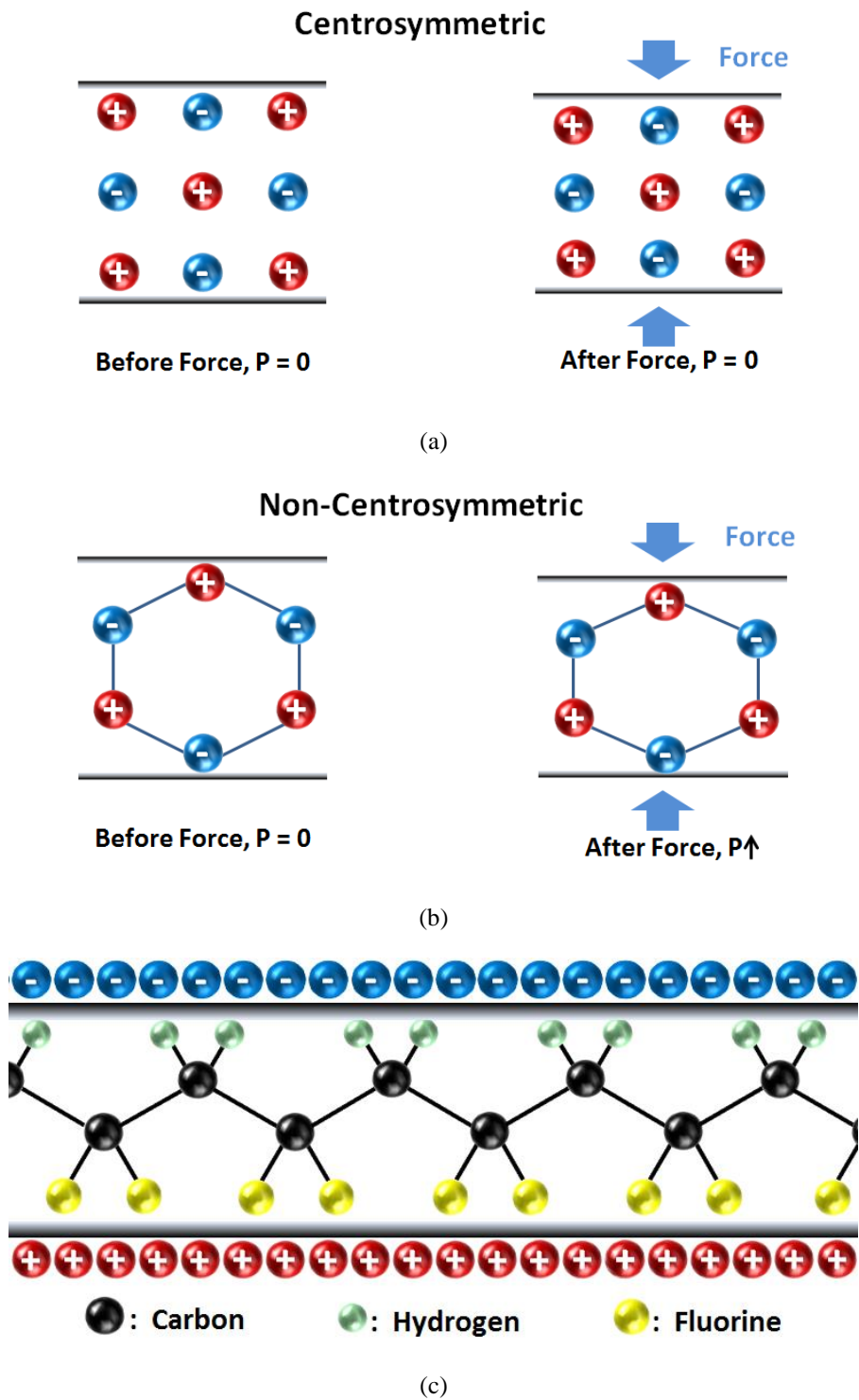


Figure 2. 7 (a)-(b) The change of polarization in Centrosymmetric and non-Centrosymmetric structures. (c) Structure of PVDF  $\beta$ -phase, modified from [30].

The charge and voltage piezoelectric constants are denoted as  $d$  and  $g$ , respectively. Their relationship is expressed as [34]:

$$d = \varepsilon_0 \varepsilon_r g ; \quad (2.1)$$

where  $\varepsilon_0$  is the vacuum permittivity (8.85 pF/m), and  $\varepsilon_r$  is the relative permittivity (dielectric constant) of the piezoelectric material. Electrically,  $d$  and  $g$  represent short and open circuit conditions for the piezoelectric materials. In direct and converse effects,  $d$  and  $g$  are defined as [34]:

<b>Direct Effect</b>	<b>Converse Effect</b>
$d = \frac{\text{charge density developed}}{\text{applied mechanical stress}}$	$d = \frac{\text{strain developed}}{\text{applied electric field}}$
$g = \frac{\text{electric field developed}}{\text{applied mechanical stress}}$	$g = \frac{\text{strain developed}}{\text{applied charge density}}$

Table 2. 5 Definitions of  $d$  and  $g$  in direct effect and converse effect.

The generalised form of the interaction between mechanical and electrical behaviour, based on a linear approximation, can be expressed as:

$$\varepsilon = \varepsilon^E \sigma + dE; \quad (2.2)$$

$$D = \varepsilon^\sigma E + d\sigma; \quad (2.3)$$

here  $S$  and  $T$  denote the strain and the applied stress,  $E$  and  $D$  represent the electric field strength and the dielectric displacement, and  $s$  and  $\varepsilon$  indicate the compliance and the permittivity.

As the directions of poling and mechanical deformation can be varied, it is desirable to identify the axes of a sample when specifying the parameters. Normally a model similar to that shown in Fig. 2.8 is used to indicate the directions of poling and mechanical

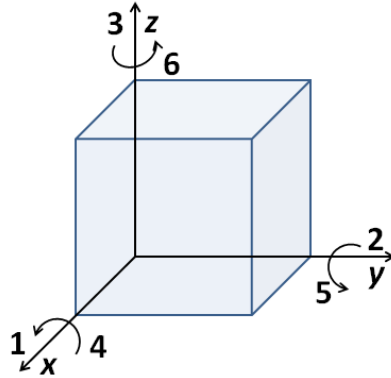


Figure 2. 8 Directions of poling and mechanical deformation.

deformation [35]. Here the three axes ( $x$ ,  $y$  and  $z$ ) are perpendicular to each other. Of these, the “3-axis” ( $z$ ) usually represents the poled direction. Shear strains related to directions 1, 2 and 3 are denoted as 4, 5 and 6. From this coordinate system, the generalised form incorporates directional notation. Thus, when a piezoelectric sample is poled in the “3-direction”, and stress is also applied in the “3-direction”, the relationship between  $d$ ,  $D$  and  $T$  becomes:

$$d_{33} = [\delta D_3 / \delta T_3]_E ; \quad (2.4)$$

The electrodes are on the faces in the “3-direction” and the external electric field is constant. Eq. 4 can be rewritten as:

$$d_{33} = (Q / F) ; \quad (2.5)$$

where  $Q$  is the charge developed, and  $F$  is the applied force. Equation 2.5 offers a means to measure  $d_{33}$  using the direct method.  $d_{33}$  can also be measured using the indirect method, which can be explained by rewriting Eq. 2.1 as:

$$d_{33} = [\delta S_3 / \delta E_3]_T ; \quad (2.6)$$

In this case, the experiment is carried out under constant stress. The direct (Berlincourt) method is introduced below in detail, as force touch detection is similar to the inverse procedure of the direct method.

## **2.2.2 Berlincourt Method for Piezoelectric $d_{33}$ Coefficient**

### **Measurement**

The Berlincourt method uses the direct effect for quasi-static measurement of the piezoelectric  $d_{33}$  coefficient [36]. It is named after Don Berlincourt, who made an important contribution to designing and fabricating the first commercial  $d_{33}$  measurement system [34]. A Berlincourt method based piezoelectric coefficient measurement system normally comprises two parts: the force head and the control electronics. The force head consists of the loading actuator and a reference sample, and the control electronics include the force control (strength and frequency) system, the charge measurement system, and the piezoelectric coefficient ( $d_{33}$ ) calculation system. There are many factors affecting the accuracy of  $d_{33}$  measurement using the Berlincourt method. These factors are summarized and explained below.

#### *AC Measuring Force*

The AC measuring force can be described according to its strength (magnitude) and frequency. The magnitude does not significantly influence the measurement result, unless the piezoelectric material works in a non-linear regime. The merit of applying a stronger AC force is to generate more charges, giving rise to a higher signal to noise ratio (SNR). However, this may result in the piezoelectric material operating in a non-linear regime.

In contrast, the frequency does result in different  $d_{33}$  measurement results. Due to thermal drift and charge dissipation, a static force cannot be applied. The frequency range is approximately 10 Hz to 1 kHz, governed by the charge measurement system, the stability of the generated charge during the measurement, and the load application

method. Furthermore, the measurement frequency should avoid the mains power frequencies and corresponding harmonics, because it is normally difficult to completely shield electro-magnetic interference (EMI) from surrounding electronic instruments.

Besides the system performance, the effect of the AC force frequency depends on the properties of the tested piezoelectric material. In [37], the measurement results for hard (PC4D) and soft (PC5H) materials were different. The piezoelectric  $d_{33}$  coefficient of the hard material was boosted with the increment of AC force's frequency; while the  $d_{33}$  of the soft material was stable under 150 Hz, and then followed the same trend as the hard material. This can be explained by the suppression of domain movement at increasing frequencies for soft materials, and the de-aging effect for hard materials.

#### *Effect of Static Pre-load*

Static pre-load is used to clamp the samples at a desired position. Static pre-load has opposite effects on hard and soft piezoelectric materials. In hard materials, the piezoelectric  $d_{33}$  coefficient rises with increasing pre-load. Soft piezoelectric materials show the opposite trend. However, the measurement is more reliable under greater pre-load [38].

#### *Time Dependent Effect*

The measurement result is time dependent when the sample is under pre-load. For all the measurements in [39], the piezoelectric  $d_{33}$  coefficient reduces over time, and eventually becomes stable. The specific decay rate is related to the property of the tested piezoelectric material. However, in general, the time to reach stable status for soft materials is longer than that of hard materials [39].

#### *Second Order Effect*

In practical measurements the time dependent effect can be combined with the frequency dependent effect. If the frequency sweeps from low frequency to high frequency then back to low frequency when measuring the piezoelectric  $d_{33}$  coefficient,

the measured results for a given frequency are different, showing hysteretic behaviour [40]. To eliminate the second order effect, the measurement can be made after the pre-load has been applied for several hours, to ensure that the piezoelectric  $d_{33}$  coefficient has reached a stable region.

#### *Sample and Loading Geometry*

When measuring the piezoelectric  $d_{33}$  coefficient using the Berlincourt method, the sample under test should be under compression. However, this is not always true in practice. The effect of the sample and loading geometry refers to the shear stress generated when the load contacts the sample and the mechanical interactions between them. To reduce the shear stress, contact electrodes need to be carefully designed. For example, flat electrodes can be used for thin films.

#### *System Calibration*

Two calibration points are the zero calibration and gain setting. Normally a non-piezoelectric material is used for zero calibration, and an already tested hard PZT is used for gain setting. Due to the frequency dependent effect, system calibration must be carried out again once the AC force frequency changes.

#### *Environment Effect*

In addition to the effects arising from the sample and measurement system, the testing environment also significantly affects the value of the measured piezoelectric  $d_{33}$  coefficient. For example, EMI from surrounding electronic instruments disturbs the electric field, so that the measurement is not made under a constant electric field. Also sudden changes to temperature and humidity can create pyroelectric charges and additional paths for charge leakage. All of these can produce inaccuracy in the measurement.

For ideal solid state materials, the most simple model for describing deformation behavior is Hookean linear elasticity. The end point of elastic deformation is fracture.

However, the behavior of many materials in real world is time dependent and nonlinear as discussed above which is related to some combinations of elastic and viscous responses. As to the PVDF, we mainly consider its time and temperature dependent responses (especially the temperature as which may decrease  $d_{33}$  [45]), which are related to force touch's detection accuracy.

### 2.2.3 Challenges of Piezoelectric Material Based Force Touch

#### Detection in Interactive Displays

As mentioned above, the force detection process is similar to the inverse process of measuring the piezoelectric  $d_{33}$  coefficient using the Berlincourt method. Here,  $d_{33}$  is determined by measuring the force induced charges. Equations for this can be summarized as:

$$\sigma = F / A ; \quad (2.7)$$

$$P_3 = d_{33}\sigma ; \quad (2.8)$$

$$Q = AP_3 = d_{33}F; \quad (2.9)$$

where  $P_3$  is the force induced polarization in the poled direction,  $\sigma$  indicates stress. As the sample is under compression, scalar expression of Hook's law is used. As stated in a previous section, the piezoelectric  $d_{33}$  coefficient is not constant, and the actual value depends on many factors. Thus, it is necessary to address how these factors affect the accuracy of force touch detection, when the piezoelectric material is integrated into a touch panel system. Two assumptions are made. First, that the touch panel is designed for interactive displays in a current commercial consumer product (e.g. a mobile phone). Second, that the force touches are performed by human fingers. The following discussion is based on these two assumptions.

The frequency of the force touch is limited to a certain frequency band, and is highly dependent on the individual's behaviour and the type of software application. For

example, drawing applications normally don't require fast touch actions, while game applications may demand quick touches. Thus, when the piezoelectric material is used for force detection, the same force can generate different charges when the touch speed differs, decreasing the force touch detection accuracy.

The effects of force amplitude and time of the pre-load can be neglected, since after the product is assembled, the amplitude of the pre-load is almost fixed, and will not dramatically change during a short time. The time of the pre-load is normally at the scale of days and months, indicating that the piezoelectric  $d_{33}$  coefficient is in the stable region. The geometry of the sample and loading are strongly related to the product design, thus the effect of geometry is not discussed here.

The main environmental factors are the temperature and EMI interference. In practice, the main contributor to these two factors usually is the interactive display itself. The electric power source, touch function and display function can be the main EMI contributors, affecting both the piezoelectric  $d_{33}$  coefficient and the accuracy of the readout circuit. As shown in [23], the noise from the charger and LCD can exceed 1 V, strongly weakening the force touch accuracy. However, these two types of noise can be canceled using correlated double sampling (CDS), as described in [7]. Another type of noise from the interactive display can originate from other touch sensing functions. Here, only the project capacitive touch sensing is discussed. DC signals are widely used for resistive and optical touch sensing functions, the effects of which can be treated and removed as offset [41][42]. The capacitive touch function employs a sensing signal of around 100 kHz [21] to detect capacitive touch events, as shown in [23]. Thus, by using low-pass and high-pass filters, the capacitive and force touch signals can be separated.

Two main sources contributing to changes in temperature are the external AC electric field and electrical components of the interactive display. The AC electric field can result in small vibrations of the piezoelectric film, giving rise to a boost in temperature [34]. However, as the EMI induced heat is normally much smaller than that from the

processor of the interactive display, it can be neglected. Temperature changes made by the processor or other components can give rise to charge generation, due to the pyroelectric behavior of ferroelectric materials. The incremental rate is very slow, indicating that the frequency is much lower than the force touch signal. Hence, the pyroelectric signal can be filtered out, or cancelled using CDS related techniques [7], since it is a time correlated signal.

Besides the instability issue of the piezoelectric  $d_{33}$  coefficient previously discussed, there are two challenges facing force touch detection using piezoelectric materials in interactive displays: static force detection and elimination of force interferences. Two factors affect the static force detection. First, piezoelectric materials normally offer high relative permittivity [40], which results in charge dissipation. Second, thermal drift gives rise to charge generation due to the pyroelectric phenomenon [34]. Elimination of force interferences is complicated by charges induced by adjacent force touches, which can be interpreted by the system as a light force touch, giving rise to force touch mis-registration.

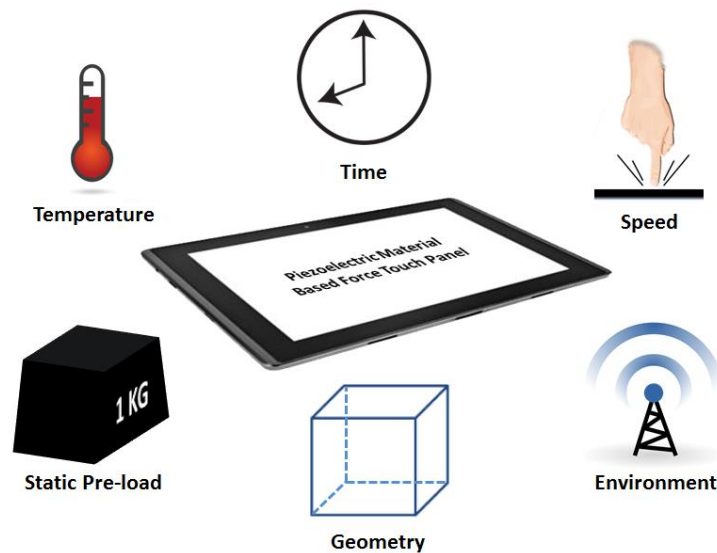


Figure 2. 9 Main factors affecting force touch sensing in a piezoelectric material based interactive display.

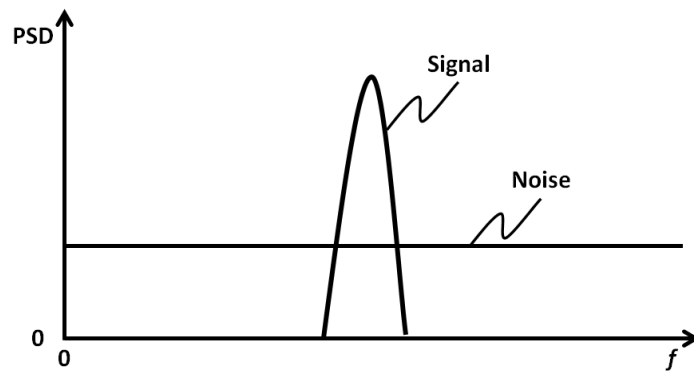
The above discussion shows that there are many factors that can influence the accuracy of force touch detection in a piezoelectric material based interactive display, as shown in Fig. 2.9. Some factors among these can be neglected, such as time, static pre-load and temperature, since they do not change dramatically over a short period of time. Nevertheless, the touch speed and geometry of the touch object may strongly disturb interpretation of the force signal. For example, the extreme touch speed case is a DC force touch vs. a high speed touch, since although the same force is used, the output signals are different. As to the case of various touch object geometries, different amounts of stress can be induced by the same force when the contact areas are different. As the touch detection accuracy can be undermined by the factors explained above, the readout circuit design is vital for achieving high detection accuracy. The following section discusses readout circuit designs for piezoelectric material based human force touch sensing.

## **2.2.4 Readout Circuit for Piezoelectric Material Based Force Touch**

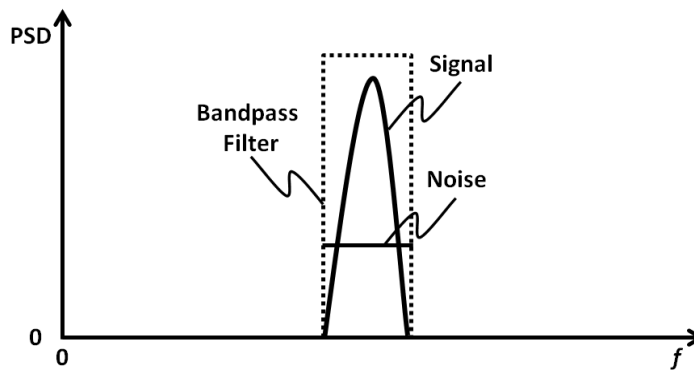
### **Signal**

Previous sections discussed the Berlincourt method for measurement of the piezoelectric  $d_{33}$  coefficient, and the reverse Berlincourt method for force signal detection in interactive displays. This section discusses the practical considerations in designing readout circuits for force touch induced electric signals.

The main purpose in carefully designing the readout circuit is to improve the sensitivity of the electrical system. Sensitivity here indicates the minimum detectable force for the system, which is equivalent to the condition at which the applied force is strong enough that the SNR of the system is equal to 0 dB. To increase the system sensitivity, either the signal power can be boosted, or the noise power decreased. Boosting the signal power can be done at different stages, for example, an RF signal can be amplified before sensing and after receiving through an antenna. The most important stage is at



(a)



(b)

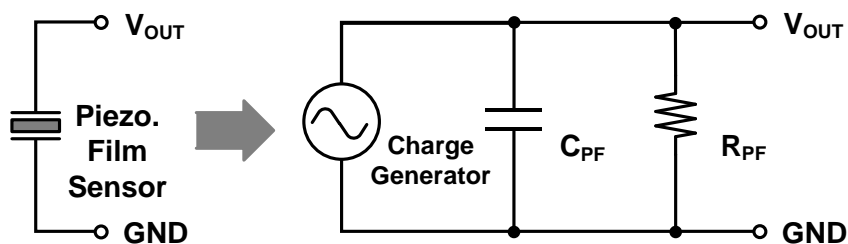
Figure 2. 10 Main factors affecting force touch sensing in a piezoelectric material based interactive display.

the signal source, because at other stages, the noise is also amplified, due to it sharing the same bandwidth as the signal, as shown in Fig. 2.10.

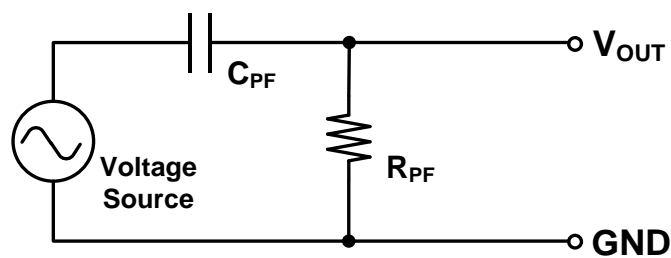
The issue at the signal source side of the piezoelectric material touch sensor is that, due to its high impedance, not all the electric signal generated by force touch can be acquired by the circuit. The equivalent circuit for a piezoelectric material based touch pad can be modeled as Fig. 2.11, consisting of a charge generator, a capacitor, and a resistor. The charge generator is based on the piezoelectric phenomenon. The magnitude of the generated charge depends on the piezoelectric coefficient of the piezoelectric material and the applied force. The capacitance of the touch pad capacitor can be calculated by the following equation:

$$C = \frac{A}{d} \epsilon_0 \epsilon_r ; \tag{2.10}$$

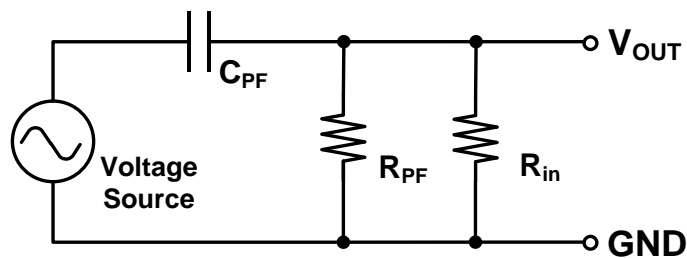
where  $A$  is the overlapped area of the electrode,  $d$  is the piezoelectric film's thickness, and  $\epsilon_0$  and  $\epsilon_r$  are the vacuum permittivity and relative permittivity, respectively. The resistance of the piezoelectric film touch pad is expressed as:



(a)



(b)



(c)

Figure 2. 11 Equivalent circuit of piezoelectric film based force sensor. (a) current source, (b) voltage source and (c) with input resistance.

$$R = \rho \frac{l}{A} ; \quad (2.11)$$

where  $\rho$  is the resistivity of the piezoelectric material. The resistivity of the piezoelectric material is normally huge. For example, the electrical resistivity of PVDF [44] is around  $2 \times 10^{14} \Omega/\text{cm}$ . As in the calculation of the capacitance,  $A$  indicates the contact area between the electrodes and the piezoelectric film, and  $l$  represents the thickness of the piezoelectric film. For a piezoelectric material based touch pad,  $l$  is equal to  $d$ . If  $d$  ( $l$ ) is assumed to be  $100 \mu\text{m}$ , and  $A$  is  $1 \text{ mm}^2$ , the corresponding values for the capacitance ( $C_{PF}$ ) and resistance ( $R_{PF}$ ) are  $1 \text{ M}\Omega$  and  $1 \text{ pF}$ , respectively.

In order to acquire the force induced electric signal, the impedance of the readout circuit needs to be large enough to take sufficient signal. This can be explained in Fig. 2.11 (c). The input resistance of the readout circuit is  $R_{in}$ , and the internal resistance and capacitance of the piezoelectric film based touch sensor are  $C_{PF}$  and  $R_{PF}$ , respectively. These three components consist of a voltage divider, requiring  $R_{in}$  to be large enough to take sufficient voltage. Below a simple experiment is demonstrated.

First an oscilloscope is directly connected to the sample to read the force induced piezoelectric signal. The experimental results are shown in Fig. 2.12 (a). The touch induced signal is around  $3.5 \text{ V}$ , large enough to light a light emitting diode (LED). However, when an LED is connected to the sample, the LED is not lit. This is because the internal impedance of the oscilloscope is very large, thus a part of the signal can be taken from the signal source. When an LED is used as the load, its impedance is not comparable to the signal source, thus the LED cannot be lit. A buffer circuit can be used to transfer the signal energy to the load. The buffer circuit should be designed to have high input impedance and low output impedance. In the experiment, a charge amplifier is used as the buffer circuit, as shown in Fig. 2.12 (b). With the charge amplifier, the generated charges can be conveyed to the load (LED), and then the LED is lit as shown in Fig. 2.12 (c).

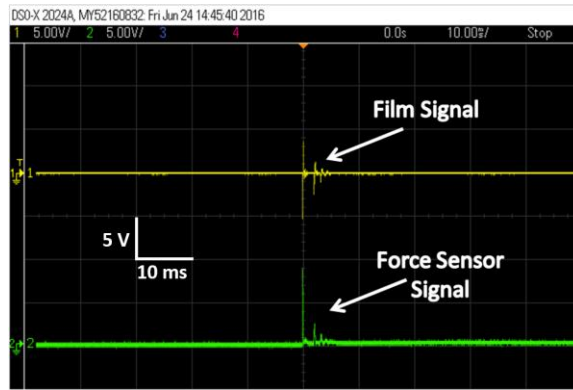
Besides acquiring enough signal power from the piezoelectric material based touch sensor, the signal frequency band must also be taken into consideration. The signal frequency depends on the speed of the touch action. The signal frequency is correlated to how fast (absolute speed value) a user performs the force touch. For example, the frequency of human touch action may be limited to within 10 Hz, which means that a user can tap the touch panel ten times during one second. However, the force touch signals from an oscilloscope, as shown in Fig. 2.13, show that the property of the force touch signal in the frequency domain is within 10 kHz. Thus, the cut-off frequency of the filter should be around 10 kHz to maintain enough signal power when fast touch events are performed.

### **2.3 Proposed Multi-functional Touch Panel**

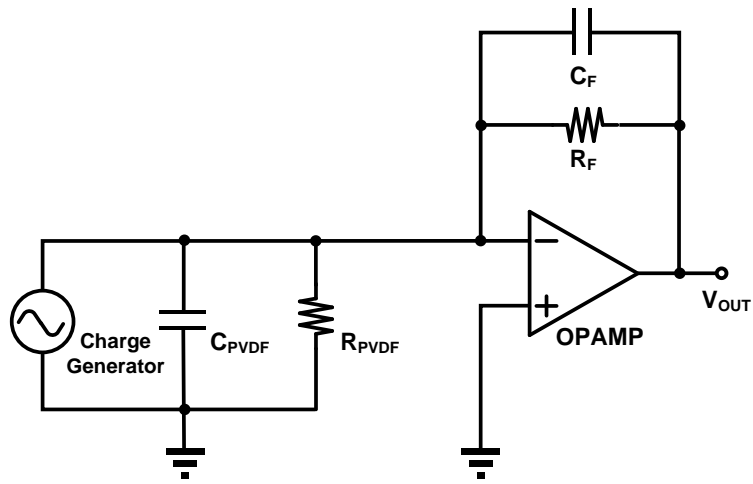
Based on the above literature reviews on capacitive touch panels and piezoelectric materials, the simple-structured multi-layered multi-functional stack-up shown in Fig. 2.14 is proposed for multi-dimensional sensing and energy harvesting in an interactive display. The piezoelectric material functions as an insulating, force touch sensing, and energy harvesting layer. A theoretical analysis of both electrical and mechanical aspects of the proposed technique is provided in the following chapter.

### **2.4 Conclusion**

This chapter provides a brief literature review on capacitive touch panels and piezoelectric materials. With an understanding of these two techniques, a multi-layered stack-up is proposed, which is expected to be able to detect capacitive touch and convert mechanical stress to electrical energy.



(a)

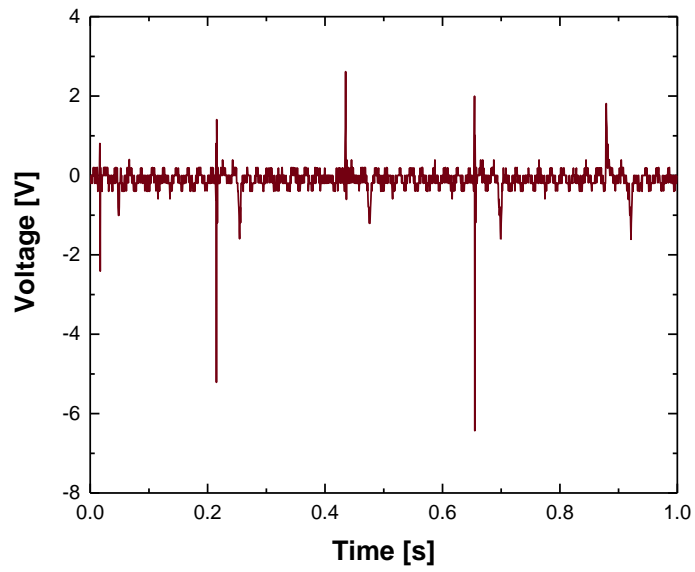


(b)

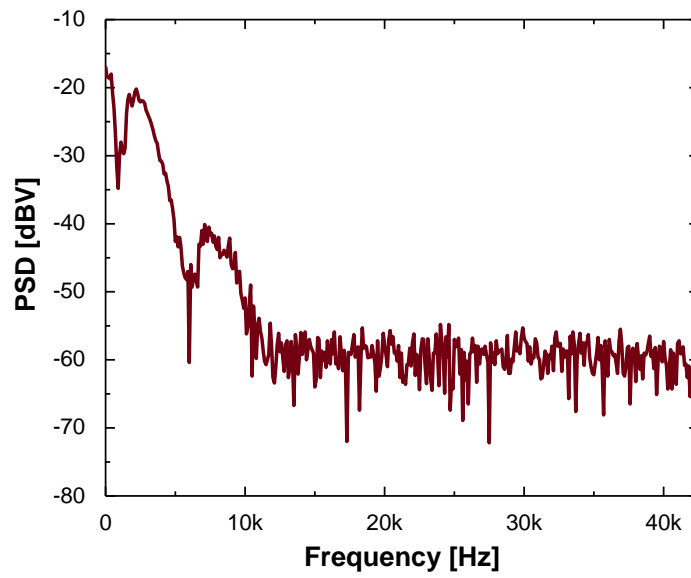


(c)

Figure 2. 12 (a) Signals from piezoelectric film and commercial force sensor. (b) Readout circuit. (c) An LED is lit by force touch induced electric power.



(a)



(b)

Figure 2. 13 Force touch signals in (a) time domain and (b) frequency domain.

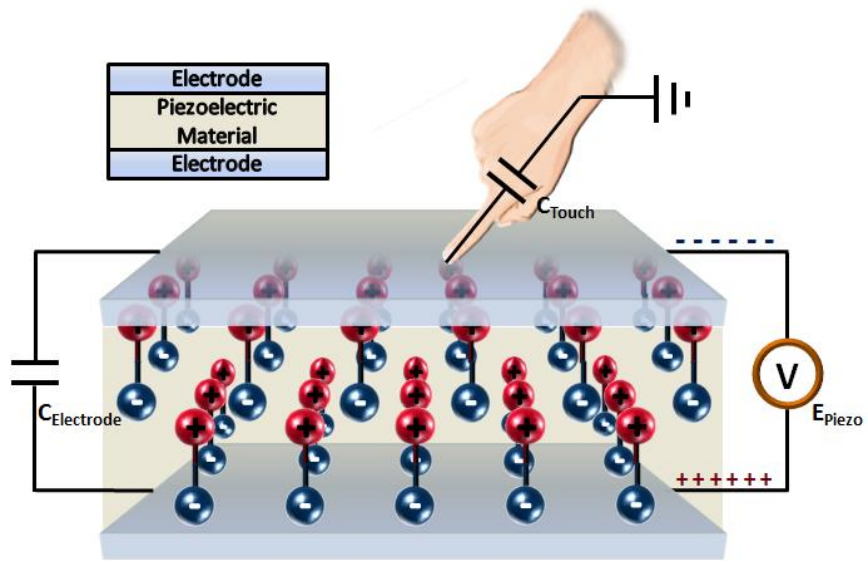


Figure 2. 14 Proposed multi-functional stack-up.

## Bibliography

- [1] Colwell Jr William, C., Elographics Inc, 1975. *Discriminating contact sensor*. U.S. Patent 3,911,215.
- [2] Barrett, G. and Omote, R., 2010. Projected-capacitive touch technology. *Information Display*, 26(3), pp.16-21.
- [3] 3M company, "Touch technology brief: Projected capacitive technology", 2011.
- [4] Walker, G., 2007. Touch and the Apple iPhone. *Veritas et Visus*, [online][retrieved on May 12, 2013] URL: <http://www.veritasetvisus.com/VVTP-12,%20Walker.pdf>, pp.50-54.
- [5] Walker, G., 2012. A review of technologies for sensing contact location on the surface of a display. *Journal of the Society for Information Display*, 20(8), pp.413-440.
- [6] Walker, G., 2013. Fundamentals of touch technologies. In *Sunday Short Course (S-4), SID Display Week 2013*.
- [7] Gao, S., Lai, J., Micou, C. and Nathan, A., 2016. Reduction of common mode noise and global multivalued offset in touch screen systems by correlated double sampling. *Journal of Display Technology*, 12(6), pp.639-645.
- [8] Shin, H., Ko, S., Jang, H., Yun, I. and Lee, K., 2013, February. A 55dB SNR with 240Hz frame scan rate mutual capacitor 30×24 touch-screen panel read-out IC using code-division multiple sensing technique. In *Solid-State Circuits Conference Digest of Technical Papers (ISSCC), 2013 IEEE International* (pp. 388-389). IEEE.

- [9] Miura, N., Dosho, S., Takaya, S., Fujimoto, D., Kiriya, T., Tezuka, H., Miki, T., Yanagawa, H. and Nagata, M., 2014, February. 12.4 A 1mm-pitch 80× 80-channel 322Hz-frame-rate touch sensor with two-step dual-mode capacitance scan. In *Solid-State Circuits Conference Digest of Technical Papers (ISSCC), 2014 IEEE International* (pp. 216-217). IEEE.
- [10] Yang, J.H., Park, S.H., Choi, J.M., Kim, H.S., Park, C.B., Ryu, S.T. and Cho, G.H., 2013, February. A highly noise-immune touch controller using filtered-delta-integration and a charge-interpolation technique for 10.1-inch capacitive touch-screen panels. In *Solid-State Circuits Conference Digest of Technical Papers (ISSCC), 2013 IEEE International* (pp. 390-391). IEEE.
- [11] Jang, H., Shin, H., Ko, S., Yun, I. and Lee, K., 2014, February. 12.5 2D Coded-aperture-based ultra-compact capacitive touch-screen controller with 40 reconfigurable channels. In *Solid-State Circuits Conference Digest of Technical Papers (ISSCC), 2014 IEEE International* (pp. 218-219). IEEE.
- [12] Ko, S., Shin, H., Lee, J., Jang, H., So, B.C., Yun, I. and Lee, K., 2010, November. Low noise capacitive sensor for multi-touch mobile handset's applications. In *Solid State Circuits Conference (A-SSCC), 2010 IEEE Asian* (pp. 1-4). IEEE.
- [13] Ko, S., Shin, H., Jang, H., Yun, I. and Lee, K., 2013, June. A 70dB SNR capacitive touch screen panel readout IC using capacitor-less trans-impedance amplifier and coded Orthogonal Frequency-Division Multiple Sensing scheme. In *VLSI Circuits (VLSIC), 2013 Symposium on* (pp. C216-C217). IEEE.

- [14] Park, J.E., Lim, D.H. and Jeong, D.K., 2014. A reconfigurable 40-to-67 dB SNR, 50-to-6400 Hz frame-rate, column-parallel readout IC for capacitive touch-screen panels. *IEEE Journal of Solid-State Circuits*, 49(10), pp.2305-2318.
- [15] Kim, K.D., Byun, S.H., Choi, Y.K., Baek, J.H., Cho, H.H., Park, J.K., Ahn, H.Y., Lee, C.J., Cho, M.S., Lee, J.H. and Kim, S.W., 2012, February. A capacitive touch controller robust to display noise for ultrathin touch screen displays. In *Solid-State Circuits Conference Digest of Technical Papers (ISSCC), 2012 IEEE International* (pp. 116-117). IEEE.
- [16] Jeong, H.E., Lee, J.K., Kim, H.N., Moon, S.H. and Suh, K.Y., 2009. A nontransferring dry adhesive with hierarchical polymer nanohairs. *Proceedings of the National Academy of Sciences*, 106(14), pp.5639-5644.
- [17] Hecht, D.S., Thomas, D., Hu, L., Ladous, C., Lam, T., Park, Y., Irvin, G. and Drzaic, P., 2009. Carbon - nanotube film on plastic as transparent electrode for resistive touch screens. *Journal of the Society for Information Display*, 17(11), pp.941-946.
- [18] Du, K.L. and Swamy, M.N., 2010. *Wireless communication systems: from RF subsystems to 4G enabling technologies*. Cambridge University Press.
- [19] Course Note of Hyper Physics, Department of Physics and Astronomy, Georgia State University, online: <http://hyperphysics.phy-astr.gsu.edu/hbase/electric/capchg.html>.
- [20] Xu, M., Sun, J. and Lee, F.C., 2006, March. Voltage divider and its application in the two-stage power architecture. In *Applied Power Electronics Conference and Exposition, 2006. APEC'06. Twenty-First Annual IEEE* (pp. 7-pp). IEEE.

- [21] Philipp, H., 2002. *Charge transfer capacitance measurement circuit*. U.S. Patent 6,466,036.
- [22] Peng, S.Y., Qureshi, M.S., Hasler, P.E., Basu, A. and Degertekin, F.L., 2008. A charge-based low-power high-SNR capacitive sensing interface circuit. *IEEE Transactions on Circuits and Systems I: Regular Papers*, 55(7), pp.1863-1872.
- [23] Gao, S., McLean, D., Lai, J., Micou, C. and Nathan, A., 2016. Reduction of noise spikes in touch screen systems by low pass spatial filtering. *Journal of Display Technology*, 12(9), pp.957-963.
- [24] Gao, S., Lai, J. and Nathan, A., 2016. Fast Readout and Low Power Consumption in Capacitive Touch Screen Panel by Downsampling. *Journal of Display Technology*, 12(11), pp.1417-1422.
- [25] Sevastopoulos, N.G. and LaPorte, D.A., Linear Technology Corporation, 2002. *Flexible monolithic continuous-time analog low-pass filter with minimal circuitry*. U.S. Patent 6,344,773.
- [26] Akhtar, H. and Kakarala, R., 2014. A methodology for evaluating accuracy of capacitive touch sensing grid patterns. *Journal of Display Technology*, 10(8), pp.672-682.
- [27] Gao, S. and Nathan, A., 2016, May. P - 180: Force Sensing Technique for Capacitive Touch Panel. In *SID Symposium Digest of Technical Papers* (Vol. 47, No. 1, pp. 1814-1817).

- [28] Akhtar, H. and Kakarala, R., 2014, October. A comparative analysis of capacitive touch panel grid designs and interpolation methods. In *Image Processing (ICIP), 2014 IEEE International Conference on* (pp. 5796-5800). IEEE.
- [29] Luo, C., Borkar, M.A., Redfern, A.J. and McClellan, J.H., 2012. Compressive sensing for sparse touch detection on capacitive touch screens. *IEEE Journal on Emerging and Selected Topics in Circuits and Systems*, 2(3), pp.639-648.
- [30] Kawai, H., 1969. The piezoelectricity of poly (vinylidene fluoride). *Japanese Journal of Applied Physics*, 8(7), p.975.
- [31] Liu, F., Hashim, N.A., Liu, Y., Abed, M.M. and Li, K., 2011. Progress in the production and modification of PVDF membranes. *Journal of membrane science*, 375(1), pp.1-27.
- [32] Goldacker, T., Abetz, V., Stadler, R., Erukhimovich, I. and Leibler, L., 1999. Non-centrosymmetric superlattices in block copolymer blends. *Nature*, 398(6723), pp.137-139.
- [33] Briscoe, J., Jalali, N., Woolliams, P., Stewart, M., Weaver, P.M., Cain, M. and Dunn, S., 2013. Measurement techniques for piezoelectric nanogenerators. *Energy & Environmental Science*, 6(10), pp.3035-3045.
- [34] Cain, M.G. ed., 2014. *Characterisation of ferroelectric bulk materials and thin films* (Vol. 2). Netherlands: Springer.
- [35] Arokia, N. and Baltes, H., 1999. Microtransducer CAD, Physical and Computational Aspects.

- [36] Berlincourt, D., Jaffe, H. and Shiozawa, L.R., 1963. Electroelastic properties of the sulfides, selenides, and tellurides of zinc and cadmium. *Physical Review*, 129(3), p.1009.
- [37] Hall, D.A., 2001. Review nonlinearity in piezoelectric ceramics. *Journal of materials science*, 36(19), pp.4575-4601.
- [38] Wooldridge, J., Muniz-Piniella, A., Stewart, M., Shean, T.A.V., Weaver, P.M. and Cain, M.G., 2013. Vertical comb drive actuator for the measurement of piezoelectric coefficients in small-scale systems. *Journal of Micromechanics and Microengineering*, 23(3), p.035028.
- [39] Cain, Markys G., Mark Stewart and Gee, M. G. 1999. Degradation of piezoelectric materials. *Teddington: National Physical Laboratory*.
- [40] Blackburn, J.F. and Cain, M.G., 2006. Nonlinear piezoelectric resonance: A theoretically rigorous approach to constant I– V measurements. *Journal of applied physics*, 100(11), p.114101.
- [41] Colwell Jr William, C., Elographics Inc, 1975. *Discriminating contact sensor*. U.S. Patent 3,911,215.
- [42] Lee, S., Jeon, S., Chaji, R. and Nathan, A., 2015. Transparent semiconducting oxide technology for touch free interactive flexible displays. *Proceedings of the IEEE*, 103(4), pp.644-664.
- [43] Krein, P.T. and Meadows, R.D., 1990. The electroquasistatics of the capacitive touch panel. *IEEE Transactions on Industry Applications*, 26(3), pp.529-534.

[44] 740 PVDF Material Data Sheet, Kynar Corp., available online:, <https://www.professionalplastics.com/professionalplastics/Kynar740DataSheet.pdf>, last retrieved on 25th Oct 2016.

[45] Jones, G.D., Assink, R.A., Dargaville, T.R., Chaplya, P.M., Clough, R.L., Elliott, J.M., Martin, J.W., Mowery, D.M. and Celina, M.C., 2005. Characterization, performance and optimization of PVDF as a piezoelectric film for advanced space mirror concepts (No. SAND2005-6846). Sandia National Laboratories.

# Chapter 3 Mechanical and Electrical

## Analysis of Interactive Stack-ups

---

The previous chapter proposed and briefly discussed an approach to implement multi-functionality in capacitance TSPs by employing piezoelectric materials [1][2]. With the piezoelectric material related technique, charges are generated on the surface when a force load is applied. The amount of charge produced is proportional to the strength of the force. Thus when the piezoelectric material is used as the substrate for the touch sensors, the induced charge can be read by the touch sensors for force sensing and energy harvesting.

However, as explained in chapter 1, the proposed technique should provide customers with similar or advanced user experience. Thus, we need to evaluate our technique with state-of-the-art commercial products. Since conventional capacitive touch detection technology is employed in our proposed technique, and there is no energy-harvesting function in commercial touch panels to the date of this research, force touch sensing function is compared to the iPhone 6S [3], in which capacitive sensors are integrated into the backlight of the display for measuring the distance change between the cover glass and the backlight. However, when a force touch happens near the edge of the touch panel, the small displacement challenges the detection accuracy. In [3] only two force sensing levels and a single force touch are supported, which cannot provide good user experience especially for drawing applications and multi-user games. Thus, in this chapter, we theoretically examine if the proposed technique based touch panel can potentially provide advanced force touch detection experience or not.

Four stack ups widely used in industry are investigated and depicted in Fig. 3.1. A thin layer of the piezoelectric film ( $\sim 20\mu\text{m}$ ) is underneath the touchscreen glass ( $\sim 0.5\text{mm}$ ). The electrodes are much thinner compared to the piezoelectric film, PET film and cover glass so they are not shown in the figure. As shown in Fig. 3.1.e, when a force is applied to the glass surface, the stress transmitted to the piezoelectric film layer will result in the induction of charges, which will be measured to interpret the force level. The mechanical and electrical properties of the touch panel strongly affect the force touch sensitivity. Below, studies on these two properties are provided, based on theoretical analysis and simulation results.

After acquiring the force induced electric signal, a challenge is to successfully interpret the capacitive touch signal and force touch signal. At the end of the chapter, the separation method for capacitive touch and force touch signals is provided, with experimental demonstration.

### **3.1 Mechanical Analysis of Proposed Touch Panels**

In this section, we analyze the mechanical response of the touch panel to force touches. Here, the relationship between force, stress, strain, panel thickness and displacement is investigated. The mechanical properties for different piezoelectric film thicknesses are investigated. The parameters of the materials are illustrated in Table 3.1. Electrode layers are not given as they are very thin compared to the other layers. Electrodes will not affect the mechanical investigation. The touch panels can be assumed as thin plates as their thicknesses are far smaller than the widths and lengths. To investigate the mechanical response of the proposed stack-ups, 13 touch locations evenly distributed throughout the touch panel are investigated. Due to the symmetric property of the touch locations, only 5 of them are analyzed, as depicted in Fig. 3.1 (f).

The force is assumed to be uniformly distributed over the contact area. The boundary conditions of the touch panel lie between a simple supported case and a fully clamped

	<b>Thickness (m)</b>	<b>Length (mm)</b>	<b>Width (mm)</b>
<b>Panel Glass</b>	$0.5 \times 10^{-3}$	122	70
<b>Piezo. Film</b>	$(10, 25, 50, 100) \times 10^{-6}$	122	70
<b>PET</b>	$50 \times 10^{-6}$	122	70
<b>Colour Filter Glass</b>	$0.4 \times 10^{-3}$	122	70

Table 3. 1 Dimension parameters of the proposed stack-ups.

	<b>Young's Modulus (Pa)</b>	<b>Poisson Ratio</b>	<b>Density (kg/m<sup>3</sup>)</b>	<b>Piezo. Coeff. (nC/N)</b>
<b>Panel Glass</b>	$7.4 \times 10^{10}$	0.3	2200	————
<b>Piezo. Film</b>	$8.3 \times 10^9$	0.18	1780	38
<b>PET</b>	$3.1 \times 10^9$	0.37	1380	————
<b>Colour Filter Glass</b>	$7.5 \times 10^9$	0.25	2500	————

Table 3. 2 Mechanical and piezoelectrical properties of the proposed stack-ups. [4]-[7]

case. For the latter, there is little literature available due to its high complexity. Thus, numerical results from finite element simulation software (COMSOL) are used for analysis. In this section, only the simply supported case is investigated. Furthermore, as the thickness and Young's modulus of the glass panel are much bigger than those of other layers, the glass panel dominates in the mechanical analysis. As a result the other layers are neglected.

Navier-Stokes double Fourier series solution [8] is used to obtain the displacement (Eq. 3.1) at a particular position  $(x, y)$  from a point force applied at a particular location  $(\zeta, \eta)$ .

Some of the assumptions of Kirchhoff-Love plate theory are as follows:

1. The thickness of the plate is much smaller than all the other physical dimensions
2. The displacements of the plate are small compared to the plate thickness
3. The material is linear elastic
4. Plane strains are small compared to unity

Our model meets all of these criteria. The closed-form solution is expressed as:

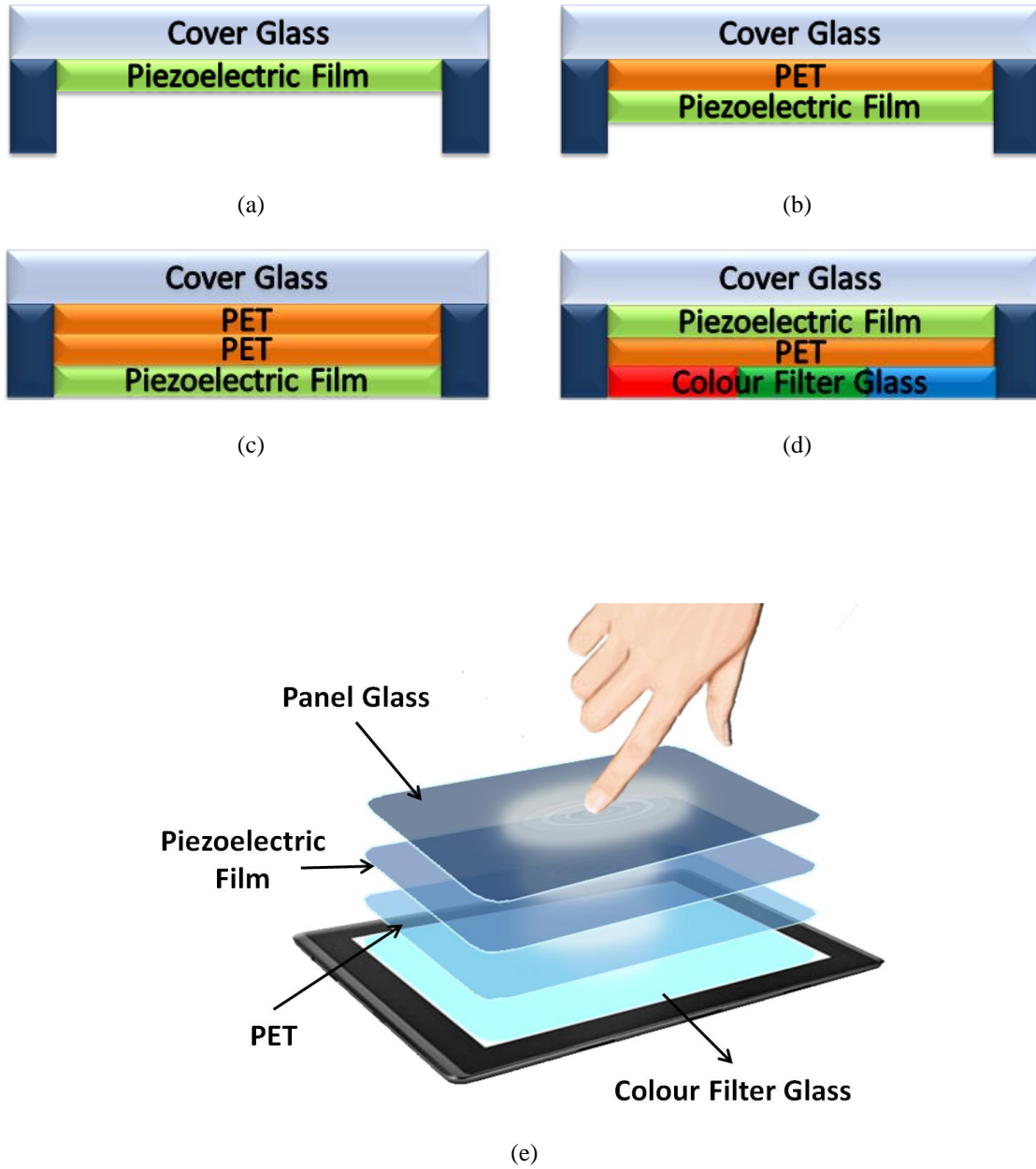
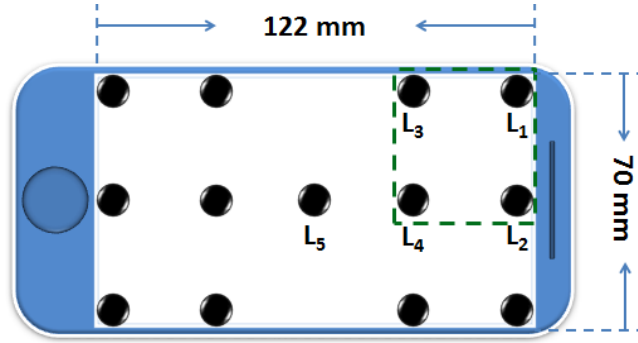


Figure 3. 1 Four proposed stack-ups of touch panels (a) – (d), the electrodes are on and underneath the piezoelectric film layer. (e) Conceptual force touch event applied on one of the stack-ups.



(f)

Fig. 3.1. (f) Top view of the investigated touch locations.

$$w(x, y, \xi, \eta) = \frac{\sum_{n=1}^{\infty} \sum_{m=1}^{\infty} \frac{4}{\pi^4 abD} \sin\left(\frac{n\pi x}{a}\right) \sin\left(\frac{m\pi y}{b}\right) \sin\left(\frac{n\pi \xi}{a}\right) \sin\left(\frac{m\pi \eta}{b}\right)}{\left(\frac{n^2}{a^2} + \frac{m^2}{b^2}\right)^2}$$

$$\text{where } D = \frac{Et^3}{12(1-\nu^2)} ; \quad (3.1)$$

The stress in the z direction is assumed to be 0 since the material is very small in the z direction compared to the other dimensions. Therefore, only plane stresses are considered. Note that this step is only to validate the suitability of the simulation environment. With other boundary conditions, the stress in z direction won't be 0, hence force induced charges can be calculated. The stresses and in the x and y directions and the shear stress ( $\tau_{xy}$ ) in the x-y plane can be found from the following expression:

$$\begin{pmatrix} \sigma_{xx} \\ \sigma_{yy} \\ \tau_{xy} \end{pmatrix} = \frac{-Ez}{1-\nu^2} \begin{bmatrix} 1 & \nu & 0 \\ \nu & 1 & 0 \\ 0 & 0 & \frac{1+\nu}{2} \end{bmatrix} \begin{bmatrix} \frac{\partial^2 \omega}{\partial x^2} \\ \frac{\partial^2 \omega}{\partial y^2} \\ 2 \frac{\partial^2 \omega}{\partial x \partial y} \end{bmatrix} ; \quad (3.2)$$

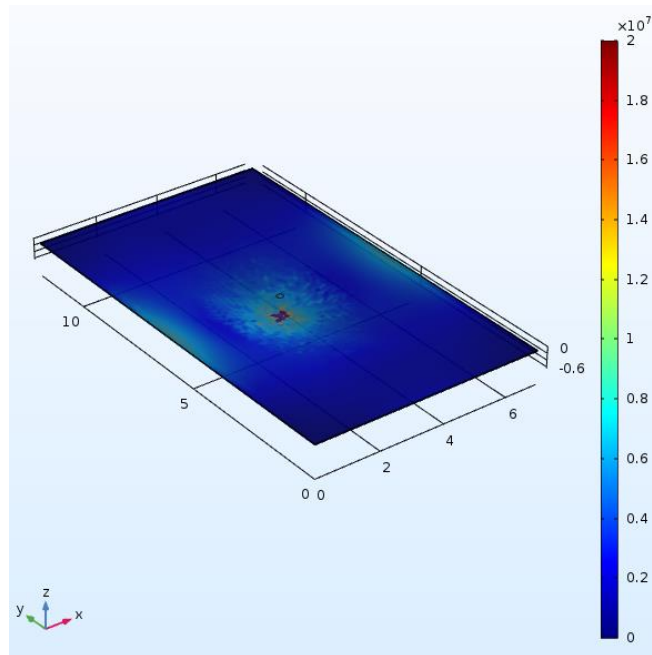
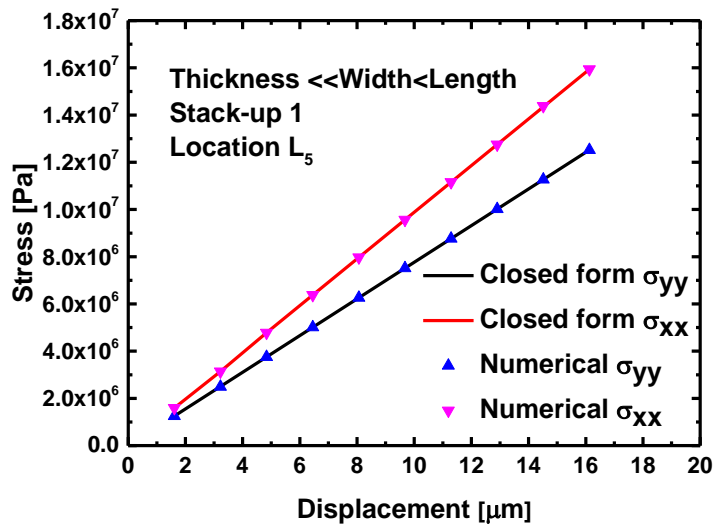


Figure 3. 2 (a) Stress vs. Displacement when thickness is 0.5mm at location  $L_5$ . (b) Stress [Pa] distribution of the touch panel. In the simulation, only one layer of PVDF is used, hence the displacement contributed by normal strain is much smaller than the curvature.

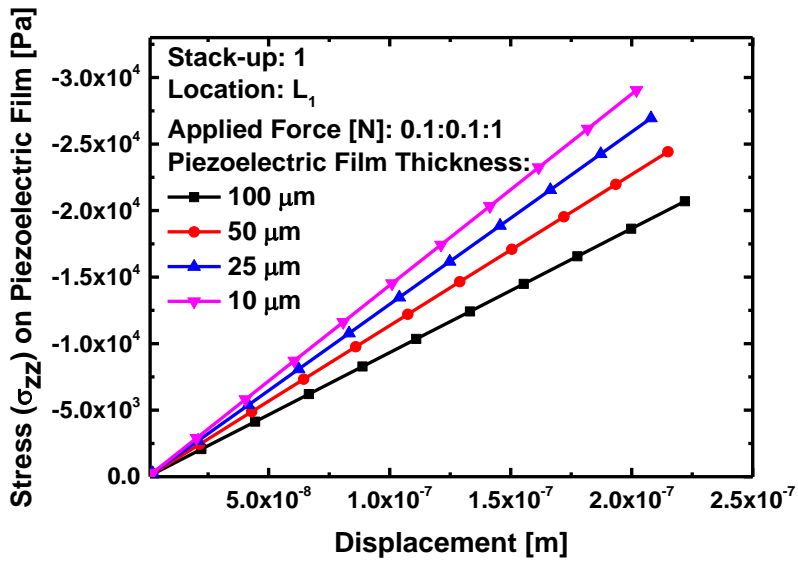
Based on the above equations, the closed-form relationship between stress and displacement is depicted in Fig. 3.2. Numerical results from COMSOL are shown

together with closed-form solution in Fig. 3.2. The good alignment validates the accuracy of COMSOL as a simulator.

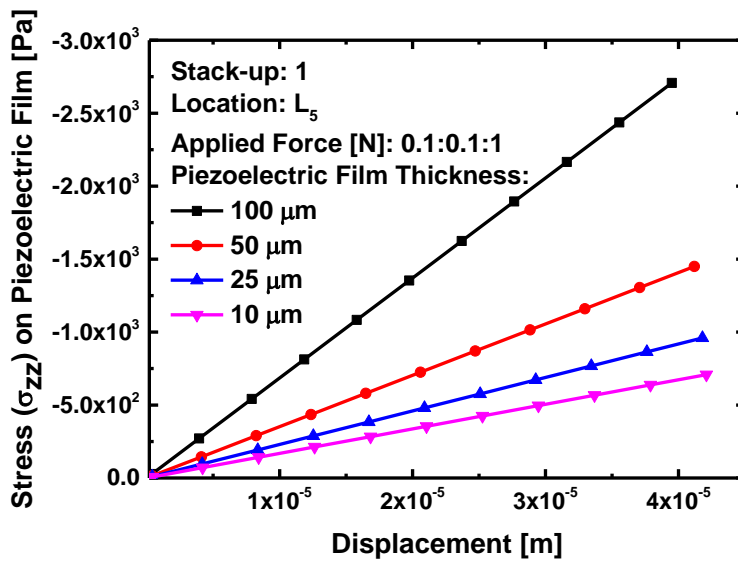
In the above paragraphs, the theoretical analysis of a simply supported plate was investigated. Due to the lack of literature on the fully clamped case, simulation results from COMSOL are utilized to analyze the resolution and sensitivity for displacements of the touch panel and stresses on the piezoelectric film. The results for location 1 and 5 of stack-up 1 are illustrated, as stack-up 1 has the lowest panel thickness and consequently the largest displacement among the four stack-ups. Locations 1 and 5 represent two extreme cases. Uniform forces over small concentric circles of radius 1mm are applied at locations 1 to 5, with different strength levels (0.1N to 1N).

The simulation results are depicted in Fig. 3.3. As described previously, five touch locations were investigated, which can be divided into two scenarios. Locations 4 and 5 are at and near the center region of the panel, thus can be explained by fully clamped plate theory. In contrast, locations  $L_1$  to  $L_3$  are close to the edges of the plate, hence they are approximated in a better way by axial compression in the  $z$  plane [9].

From Fig. 3.3, it can be observed that with the increment of piezoelectric film thickness, the displacements and stresses at locations  $L_4$  and  $L_5$  drop, which aligns with our expectation. This can be generally explained by bending stiffness ( $K$ ) which is the function of Young's modulus ( $E$ ) and thickness ( $t$ ). With the increase of  $E$  and  $t$ ,  $K$  boosts. However, at locations  $L_1$  to  $L_3$ , the displacements increase, together with the piezoelectric film thickness. This is because when the edges of the plate are fixed, the displacement is purely due to the compressive strain in the  $z$  direction. As the thickness goes up the strain will therefore increase, since the piezoelectric film has a lower Young's modulus than the glass. This also explains the stress resolution results. As the frames support the whole panel, most of the stress is concentrated at the frame regions. That is the reason why the stress values of location  $L_4$  and  $L_5$  are much smaller than those at locations  $L_1$  to  $L_3$ , while location 1 has the highest stress value.



(a)



(b)

Figure 3. 3 Resolution results for stackup 1: displacement and stress of stack-up 1, location  $L_1$  (a) and stack-up 1, location  $L_5$  (b). 0.1:0.1:1 indicates from 0.1 N to 1 N, with a step of 0.1 N.



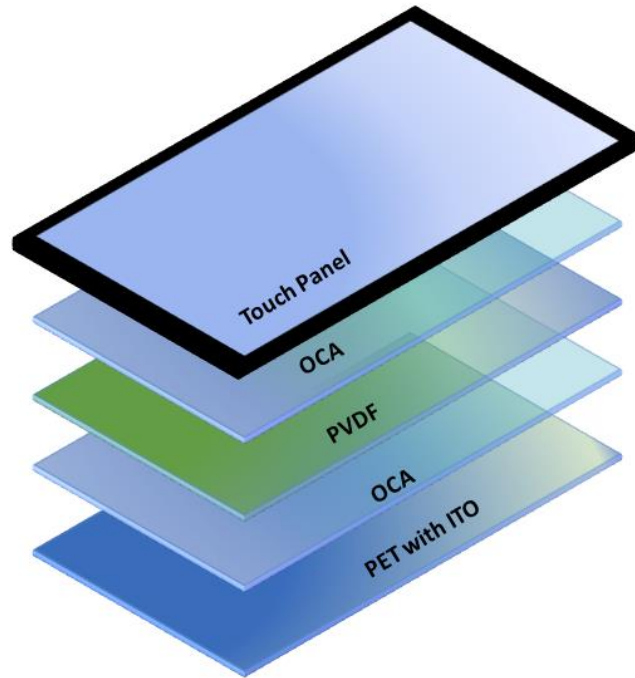
(a)



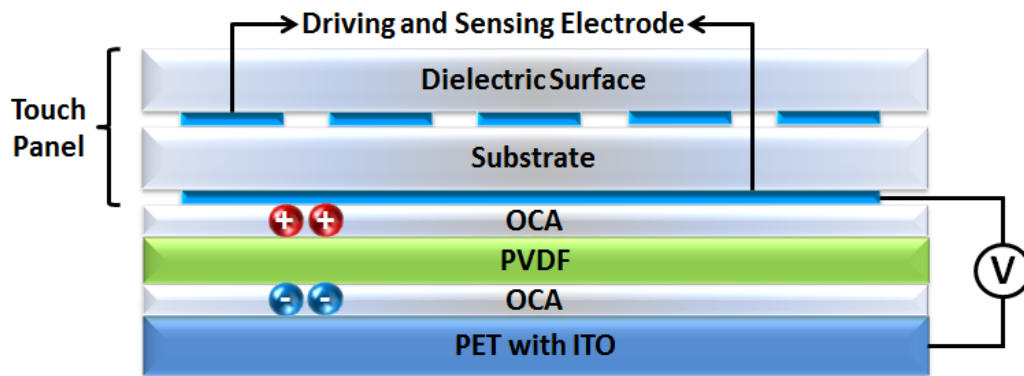
(b)

Figure 3. 4 (a) Original touch panel. (b) Touch panel laminated with PVDF and ITO coated PET.

To further examine the proposed technique, we laminate a layer of piezoelectric film ( $d_{33} = 20\text{pC/N}$ ) with a commercial touch panel (Microchip Inc). Optical Clearance Adhesive (OCA) glue is used for the lamination. The pictures of the original touch panel and laminated touch panel are shown in Fig. 3.4 (a) and (b). The structure and working principle of the laminated touch panel are shown in Fig. 3.4 (c) and (d). The touch panel's electrodes and the ITO coated PET consist of many capacitors. By



(c)



(d)

Fig. 3.4. (c) Structure of the laminated touch panel. (d) Working principle of collecting force induced charges.

selecting the correct electrode pin, the force induced voltage can be measured by an

oscilloscope. When a 1N perpendicular touch happens at the center of the panel edge, the output signal peaks at 0.2V (as shown in Fig. 3.5), indicating a high force sensitivity.

From the simulation and experimental results, a good responsivity can be achieved at 0.42 V/N. However, noise could affect signal detection, especially the system's sensitivity. Therefore an electrical analysis in terms of SNR has been carried out.

### 3.2 Electrical Analysis of Proposed Touch Panels

The force applied to the touch panel needs to be converted into an electric signal for the processor to manipulate. Henceforth, a transimpedance amplifier (TIA) is employed as the readout circuit. The SNR is an important parameter for a sensing system. In this section we theoretically analyze the SNR value for the presented piezoelectric film based force sensing system.

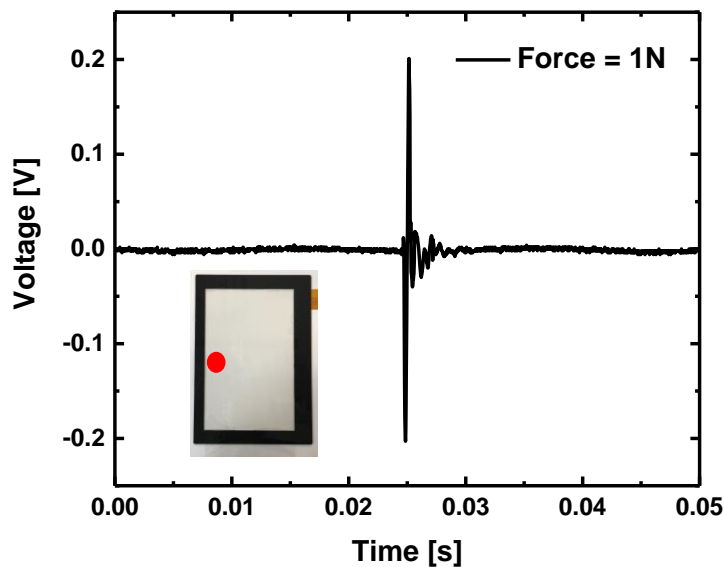


Figure 3. 5 Voltage response of a 1N perpendicular force at the center edge of the piezo film laminated touch panel. The red point indicates the touch location. The actual contact area is 1mm<sup>2</sup>.

Piezoelectric films can be modelled as a charge generator in parallel with a capacitor ( $C_{PF}$ ) and an internal film resistor ( $R_{PF}$ ) [10] as depicted in Fig. 3.6 (a). Due to the fact that different circuit designs contribute to various noise components, a typical charge amplifier is analyzed as an example. This is shown in Fig. 3.6 (b).

As the piezoelectric force sensor and readout circuit are uncorrelated noise sources, the input-referred noise power  $\overline{i_{IN}^2}$  of the force sensing system is expressed as

$$\overline{i_{IN}^2} = \overline{i_{PF}^2} + \overline{i_{RC}^2} ; \quad (3.3)$$

$\overline{i_{PF}^2}$  and  $\overline{i_{RC}^2}$  are the noise power spectrum densities (PSDs) of the piezoelectric touch sensor and the readout circuit, respectively. From Fig. 3.6 (c),  $\overline{i_{RC}^2}$  includes feedback resistor noise  $\overline{i_R^2}$  and the input current and voltage noise of the opamp ( $\overline{i_{n-op}^2}$  and  $\overline{e_{n-op}^2}$ , values can be retrieved from operational amplifier product datasheet) [11].  $\overline{i_R^2}$  is expressed as:

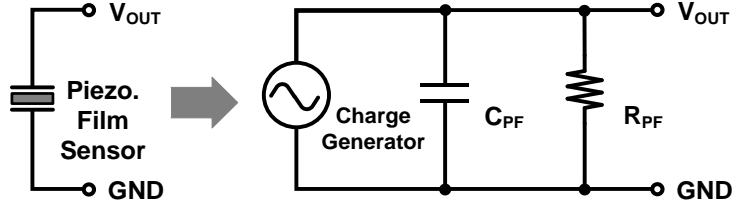
$$\overline{i_R^2} = \frac{4kT}{R_F} ; \quad (3.4)$$

where  $k$  is the Boltzmann constant and  $T$  is the temperature in Kelvin degrees. Note that  $\overline{i_{n-op}^2}$  is the shot noise of the input devices. The PSD of the output noise generated by  $\overline{e_{n-op}^2}$  is:

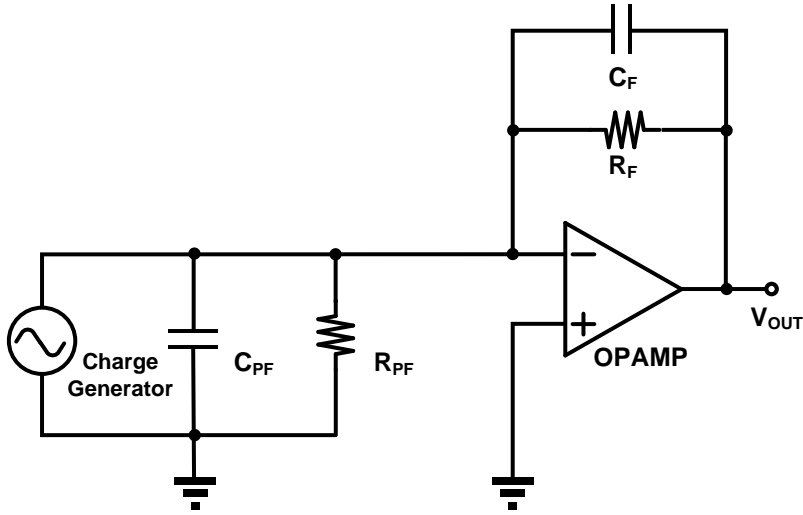
$$\begin{aligned} \overline{v_{on}^2} &= \overline{e_{n-op}^2} \left| 1 + \frac{Z_F}{Z_{PF}} \right|^2 \\ &= \overline{e_{n-op}^2} \frac{(R_{PF} + R_F)^2 + 4\pi^2 f^2 R_F^2 R_{PF}^2 (C_F + C_{PF})^2}{R_{PF}^2 (1 + 4\pi^2 f^2 R_F^2 R_{PF}^2)} ; \end{aligned} \quad (3.5)$$

Here  $Z_F$  and  $Z_{PF}$  are the feedback and piezoelectric sensor impedance values. As  $R_{PF}$  is much higher than  $R_F$ , Eq. 9 is simplified as

$$\overline{v_{on}^2} = \overline{e_{n-op}^2} \frac{1 + 4\pi^2 f^2 R_F^2 (C_F + C_{PF})^2}{(1 + 4\pi^2 f^2 R_F^2 R_{PF}^2)} ; \quad (3.6)$$



(a)



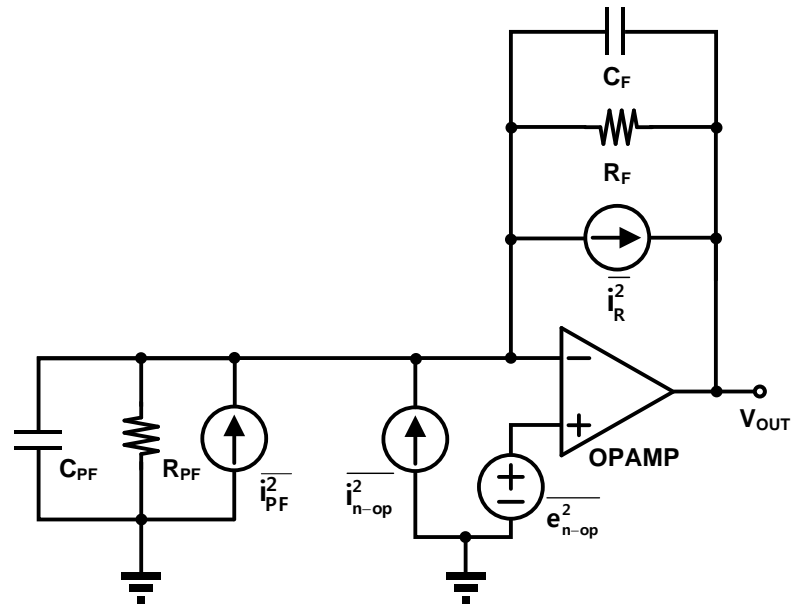
(b)

If a CMOS based operational amplifier is utilized, the shot noise can be neglected. Hence, the total input-referred noise PSD is expressed as (Fig. 3.6 (d))

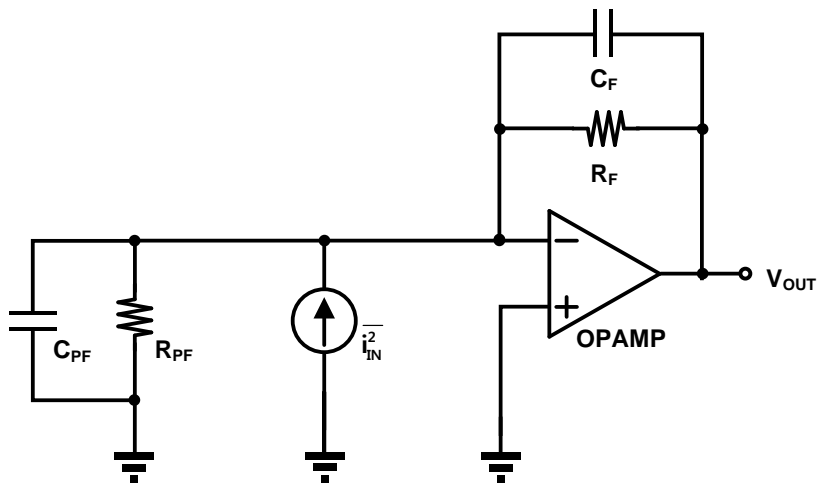
$$\overline{i_{IN}^2} = \frac{4kT}{R_{PF}} + \frac{4kT}{R_F} + \overline{e_{n-op}^2} \left[ \frac{1}{R_F^2} + (2\pi f)^2 (C_F + C_{PF})^2 \right]; \quad (3.7)$$

If we assume the force is linearly increased within a “press” period (assumed to be 0.1s) and that the sampling frequency ( $f_s$ ) is 100Hz (to ensure that we can accurately interpret the applied force). Then the signal energy ( $E_{Signal}$ ) is calculated as:

$$E_{Signal} = \frac{Q_T^2}{2C_{PF}f_s}; \quad (3.8)$$



(c)



(d)

Figure 3. 6 (a) Equivalent circuit of piezoelectric film based force sensor; (b) charge amplifier based readout circuit; (c) noise sources of the circuit and (d) input referred noise source includes all the noise sources.

here  $Q_T$  is the total generated charge during the “press” period. Furthermore, if a  $1\text{M}\Omega$  feedback resistor and a  $10\text{nf}$  feedback capacitor are used, the corresponding SNR at location 1 of stack-up 1 is around  $59.1\text{dB}$  at room temperature. This indicates that high detection sensitivity is achieved. The force could be accurately interpreted.

Besides the SNR, another thing that should not escape our attention is the electrostatics analysis. As the substrate of the touch sensors is changed from glass to piezoelectric film, the mutual capacitance ( $C_M$ ) between touch panel’s driving and sensing electrodes is decreased with the drop of dielectric coefficient. For force sensing, we need to consider if the applied force will change the distance between the electrodes to further affect the capacitance measurement, as the Young’s modulus of the piezoelectric film is much smaller than glass. In the simulation, a  $5\text{N}$  force is applied at location 5 of the dielectric surface (panel glass). The capacitance ( $7.76\text{pC}$ ) remains constant before and after the applied force, indicating that the capacitance change is negligible.

### **3.3 Separation of Force and Capacitive Combined Touch**

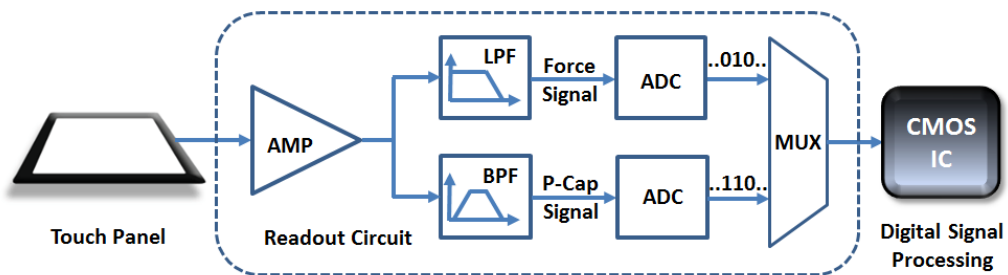
#### **Signals**

In previous sections we proposed four widely used stack-ups, and provided a detailed analysis for both mechanical and electrical aspects. Based on the theoretical analysis and simulation results, we learned that the piezoelectric material based force sensing technique can provide high force detection sensitivity. However, as the electrodes in the touch panel are shared by the force touch and capacitive touch signals, strong interference from each will decrease the accuracy of both capacitive and force touch detection. Thus interference elimination techniques must be applied to avoid the drop in detection accuracy.

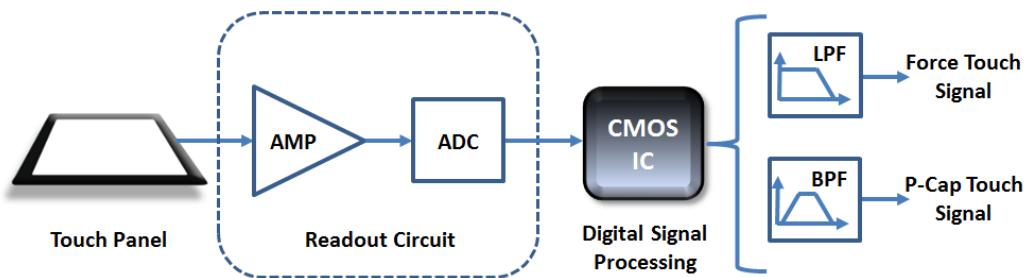
To separate these two external stimuli, the first thing to do is to analyze the frequency property of each. The frequency band of the capacitive touch signal is normally around  $100\text{ kHz}$  [12]. For example, in the nexus 7, the working frequency for the capacitive



(a)

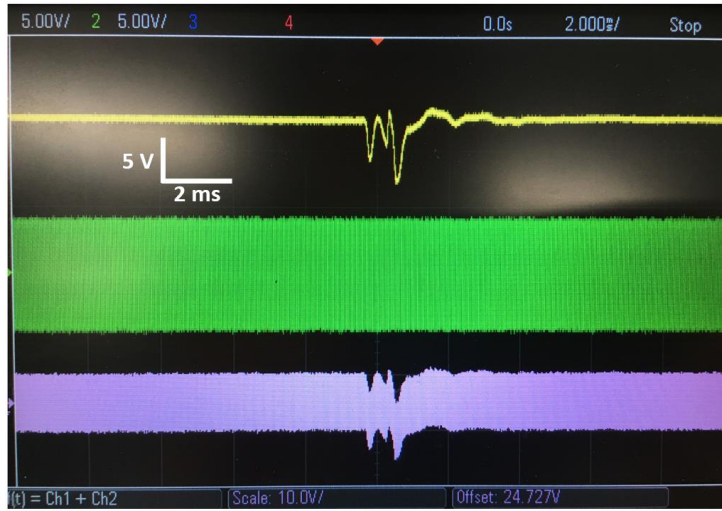


(b)

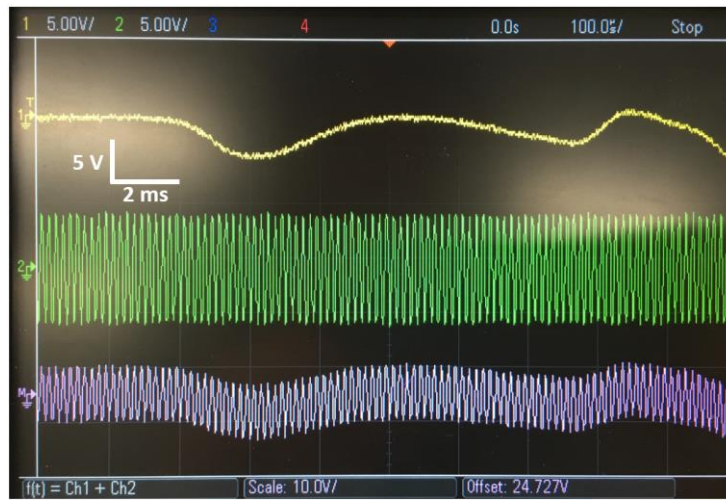


(c)

Figure 3. 7 Frequency bands of force touch signal and capacitive touch signal. Block diagram of low-pass and band-pass filtering based force touch and capacitive touch signal interpretation circuit.



(a)



(b)

Figure 3. 8 Capacitive touch signal and force touch signal and their combination in time domain.

touch signal is 90 kHz [13]. No literature is available as to the working frequency for a piezoelectric material based human force touch signal. Thus, in chapter 2, discussions and a simple experiment were carried out to find out the frequency band of the force touch signal. And we concluded that the force touch signal is a low frequency signal that occupies the frequency band from 0 to 10 kHz. The working frequency bands are conceptually shown in Fig. 3.7 (a). Thus, by using a low pass filter and a band pass filter, these two signals can be smoothly separated. As shown in Fig. 3.7 (b), the low-pass filter and the band-pass filter can be implemented on the circuit or digital signal processing (DSP) side by using algorithms. However, it is also noted that the force touch induced signals are impulses, indicating that the cut-off frequency of the low pass filter should be much higher than 10 Hz. This will be demonstrated below by experimental results.

Intuitively, these two signals (capacitive and force touch signal) should be added at the source, and then separated by the filters as discussed above. The combined signal can be assumed as a high frequency signal modulated by a low frequency signal. To demonstrate this, a function generator is used to generate a stable high frequency signal which represents the excitation signal for capacitive signal sensing. A commercial piezoelectric based touch sample (PEDOT/PVDF) is used for outputting the force signal. The fake capacitive signal and the real force signal are sent to the different channels of an oscilloscope (channel 1 and channel 2), and then these two signals are added together using the math function of the oscilloscope. The signals are shown in Fig. 3.8 (a) and (b). In Fig. 3.8, the yellow signal is the force signal, which is relatively low frequency, and the green signal represents the capacitive signal, whose frequency is 100 kHz. The blue signal is the combined signal, which is added up by the oscilloscope. The signals in Fig. 3.8 (a) and (b) are identical, with the only difference between these two figures being the time scale. The result aligns with the previous expectation.

The next step is to implement the above signal combination in a circuit. In chapter 2, different methods for capacitive signal sensing were introduced. An easily implemented

method is needed which can detect the force touch signal and capacitive touch signal at the same time. To satisfy the two requirements, it was decided to use a charge amplifier. The circuit for combining capacitive and force signals is shown in Fig. 3.9. From the circuit diagram it can be seen that the value of the capacitance  $C_{Sensor}$  is related to the piezoelectric based touch sensor. However, when a human finger taps on the touch panel, the value of the  $C_{Sensor}$  increases, because the finger-related capacitance is in parallel to the original touch sensor, boosting the capacitance value [12]. The relationship between charge, voltage and capacitance:

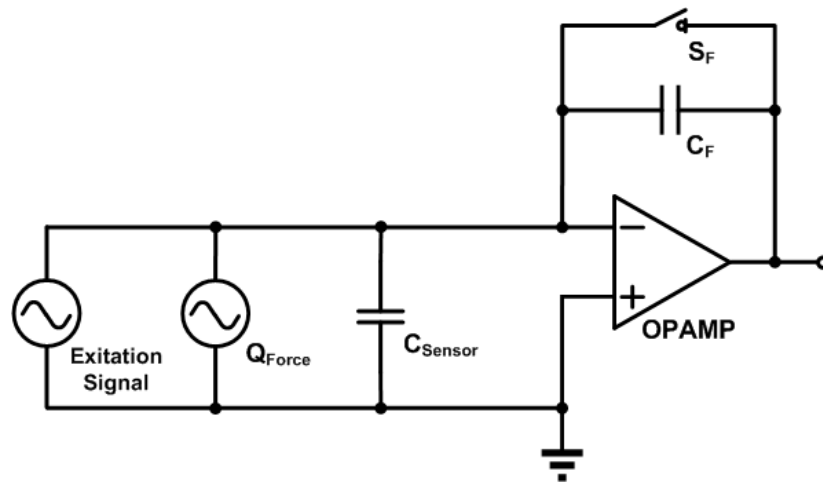
$$Q = CV; \tag{3.9}$$

shows that when the capacitance value increases for a given voltage level, the amount of stored charge decreases with linearly. Thus by periodically measuring the stored charges, we can know the capacitive change and hence interpret the presence of the capacitive touch events.

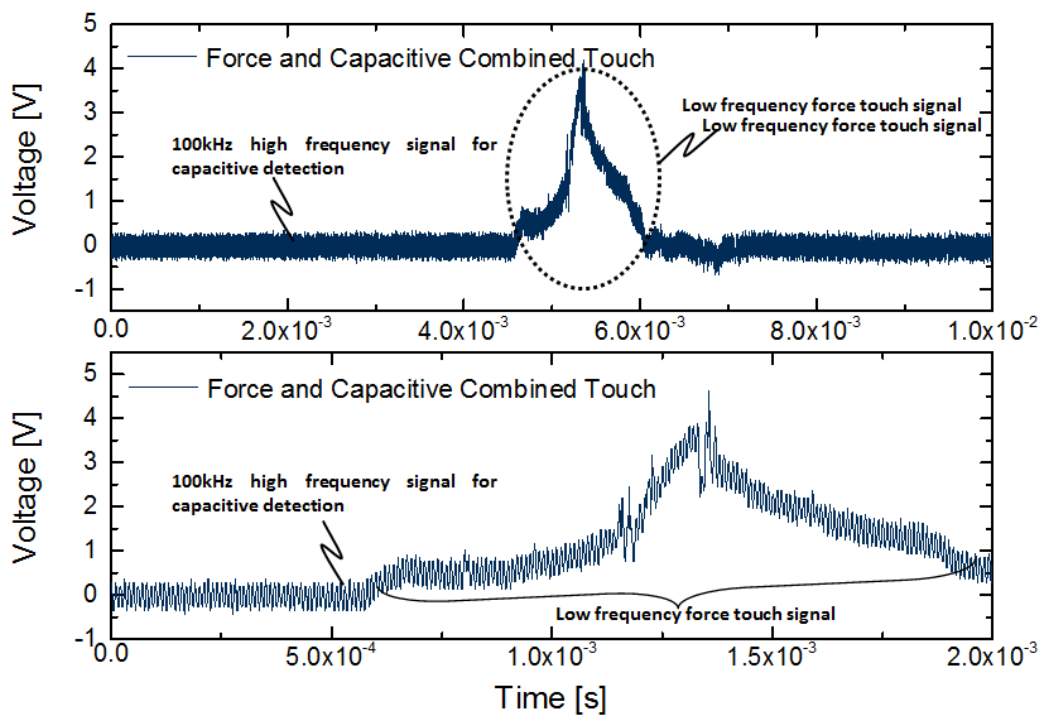
The same experiment was performed with the charge amplifier. The output was illustrated using the oscilloscope, and showed that the force signal modulates the capacitive signal, as expected. Fig. 3.9 (a) and (b) show the same signal with different time scales, to clearly demonstrate this phenomenon. To further investigate how to separate these two signals, the force and capacitive combined signal is shown in the time domain and frequency domain. Fig. 3.10 (a) shows that when no touch events occur, there is a signal in the frequency domain only at 100 kHz. In contrast, when touch events are performed, energy is boosted within the 0 to 10 kHz range, indicating that the force signal occupies the low frequency range. As the frequency bands of force and capacitive touch signals are close to each other (only one order), applying filters is not easy using hardware, thus it is suggested to apply digital filters.

### **3.4 Conclusion**

In chapter 2, a sandwiched multi-functional stack-up was proposed after reviewing capacitive touch panels and techniques related to piezoelectric materials. In this chapter, the mechanical and electrical characteristics of the multi-functional based capacitive touch panel are investigated. Based on the analysis, the proposed technique can provide better force touch accuracy and sensitivity. Furthermore, the force touch signal and capacitive touch signal can be separated in the frequency domain, validating the possibility of concurrently detecting multi-dimensional signals.

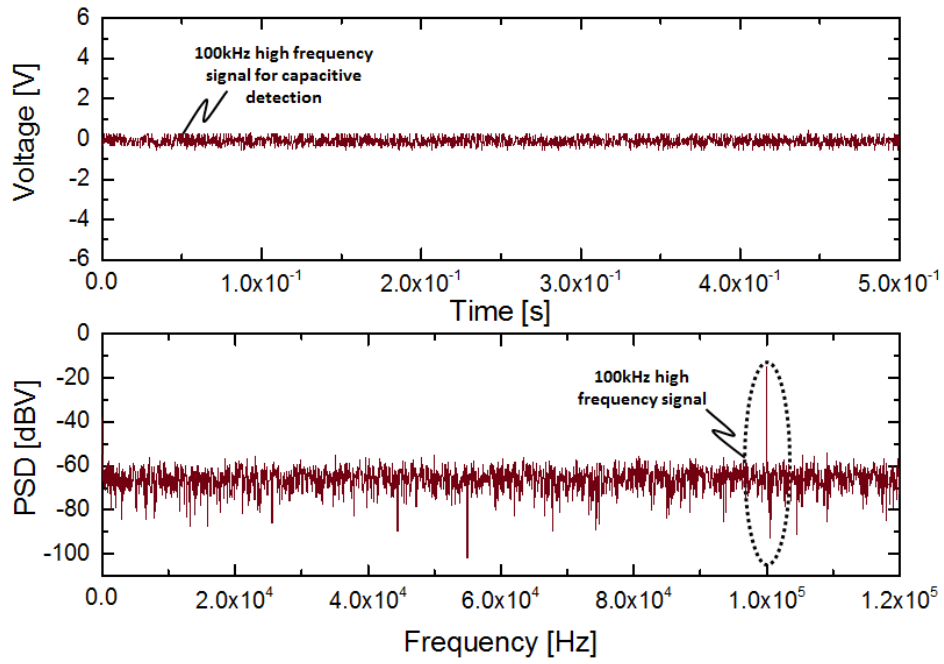


(a)

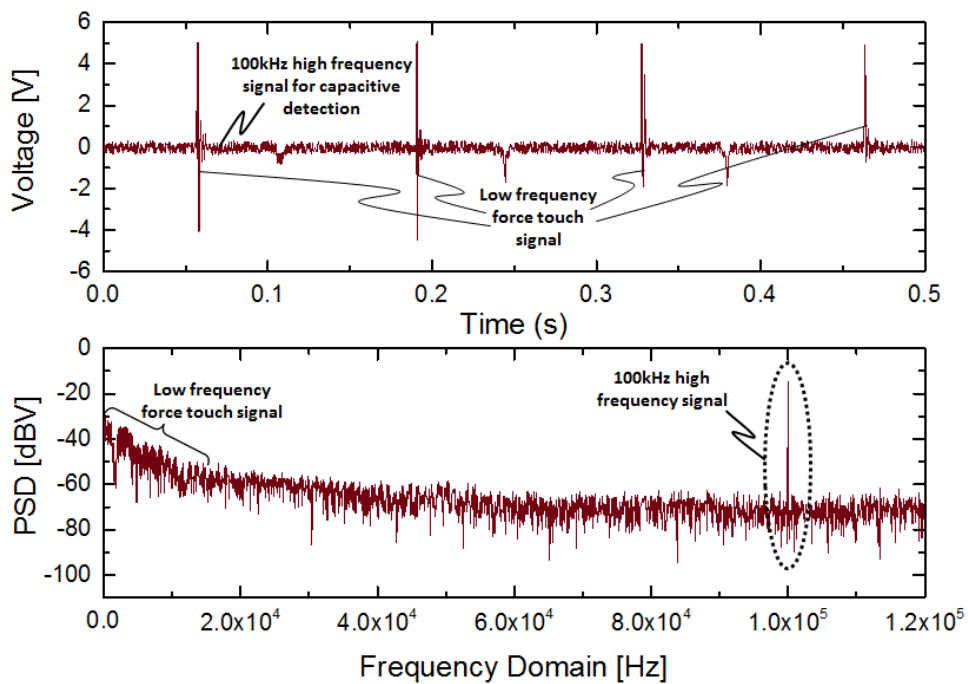


(b)

Figure 3. 9 (a) Readout circuit for force and capacitive touch signals. (b) Capacitive and force touch combined signal in time domain.



(a)



(b)

Figure 3. 10 Frequency bands of force touch signal and capacitive touch signal.

## Bibliography

- [1] Kawai, H., 1969. The piezoelectricity of poly (vinylidene fluoride). *Japanese Journal of Applied Physics*, 8(7), p.975.
- [2] Liu, F., Hashim, N.A., Liu, Y., Abed, M.M. and Li, K., 2011. Progress in the production and modification of PVDF membranes. *Journal of membrane science*, 375(1), pp.1-27.
- [3] Detwiler, B., 2015, Oct. iPhone 6S teardown reveals upgrades galore, similar hardware layout. *CNET Blog*. Available at: “<http://www.cnet.com/news/iphone-6s-teardown-reveals-upgrades-galore-similar-hardware-layout/>”
- [4] “Specialty glass products technical reference document”, Corning Inc. Aug. 2012.
- [5] Mohammadi, B., Yousefi, A.A. and Bellah, S.M., 2007. Effect of tensile strain rate and elongation on crystalline structure and piezoelectric properties of PVDF thin films. *Polymer testing*, 26(1), pp.42-50.
- [6] Speight, J. G., Norbert Adolph Lange (2005). McGraw-Hill, ed. Lange's handbook of chemistry (16 ed.).
- [7] “The future is flexible: Corning willow glass”, Technique Datasheet, Corning Inc., 2012.
- [8] Ren, B. and Lissenden, C.J., 2016. PvdF multielement lamb wave sensor for structural health monitoring. *IEEE transactions on ultrasonics, ferroelectrics, and frequency control*, 63(1), pp.178-185.

- [9] Gao, S., Arcos, V. and Nathan, A., 2016. Piezoelectric vs. Capacitive Based Force Sensing in Capacitive Touch Panels. *IEEE Access*, 4, pp.3769-3774.
- [10] “Interfacing piezo film to electronics”, Measurement Specialties, Inc. Mar. 2006.
- [11] Crescentini, M., Bennati, M., Carminati, M. and Tartagni, M., 2014. Noise limits of CMOS current interfaces for biosensors: A review. *IEEE transactions on biomedical circuits and systems*, 8(2), pp.278-292.
- [12] Walker, G., 2014. Fundamentals of Projected-Capacitive Touch Technology. *online*, *Society for Information Display Display Week*.
- [13] Gao, S., McLean, D., Lai, J., Micou, C. and Nathan, A., 2016. Reduction of noise spikes in touch screen systems by low pass spatial filtering. *Journal of Display Technology*, 12(9), pp.957-963.
- [14] <http://www.acoustics.co.uk/pal/wp-content/uploads/2015/11/Properties-of-poled-PVDF.pdf>

# Chapter 4 Fabrication and Measurement of Multi-Functional Touch Panel

---

In chapter 3, the proposed multi-functional touch panel was evaluated theoretically. The analysis shows that the proposed technique can provide higher force detection accuracy and sensitivity compared to current commercial 3D (x-y-z) touch panels [1][2]. The analysis was further proven by laminating a PVDF/ITO/PET sandwiched layer with a commercial capacitive touch panel. In this chapter, the proposed multi-functional touch panel will be fabricated and measured.

Here, mono-layered graphene [3]–[13] is used as a flexible and transparent electrode, due to its high optical transparency (97.7%), low sheet resistance ( $30 \Omega/\square$  for highly doped and  $300 \Omega/\square$  for undoped [13]) and high mechanical strength (Young's modulus of 1 TPa and intrinsic strength of 130 GPa [12]). In particular, the fracture strain of graphene can be one order higher than that of ITO [13] (ITO: 0.003-0.022 [14], Graphene: 0.14 [12]), indicating that graphene is a strong candidate for use as an electrode. In addition to the above reasons, we also want to prove that our proposed technique can cover a variety of materials, from conventional materials (e.g. ITO) to advanced materials (e.g. graphene).

## 4.1 Touch Panel Fabrication

Graphene is prepared using the previously reported chemical vapour deposition (CVD) recipe<sup>1</sup>, the process for which is shown in Fig. 4.1. First the graphene is grown on the  $5 \times 5 \text{ cm}^2$  copper substrate, which is then etched using acid (graphene is patterned by using oxygen plasma). The graphene is later transferred onto a piece of PET. The above

procedure is repeated to produce two graphene/PET structured devices. One of the devices is used as the bottom (ground) layer, and another device is patterned, working as the top electrode layer. The two devices are laminated with a piece of commercial  $\beta$ -phase PVDF from Solvay Corp., becoming a flexible, transparent and multifunctional touch panel. Lamination is processed in 90-degree environment; the pressure is not measured due to lack of technique support. The high temperature degrades the polling process of the PVDF film, the corresponding effect will be explained in the following chapter.

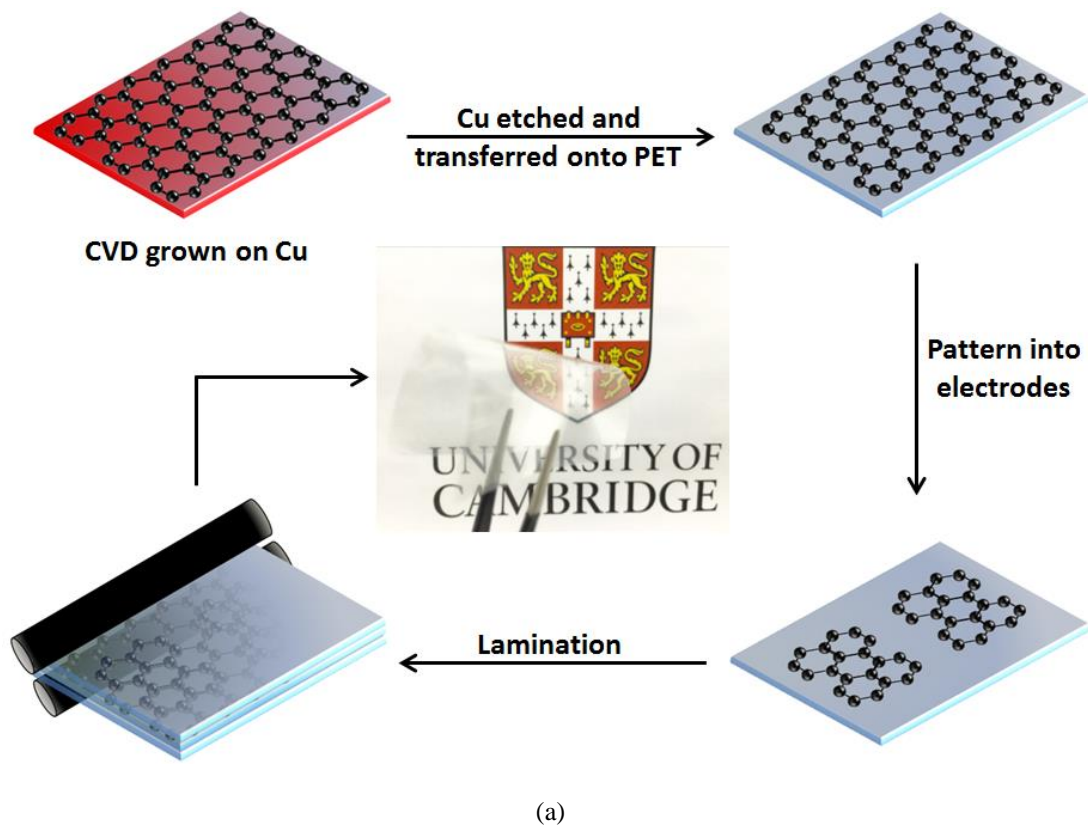
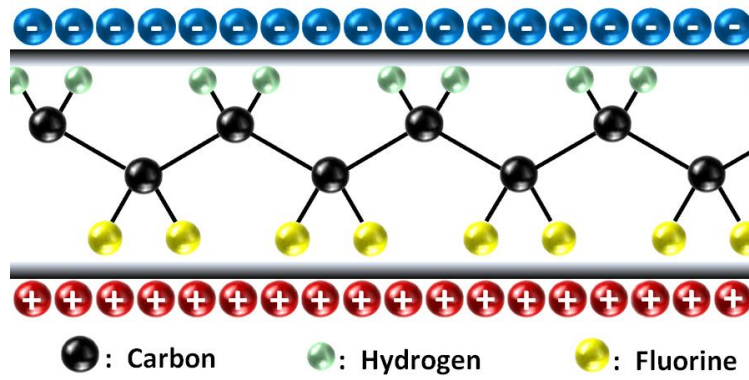
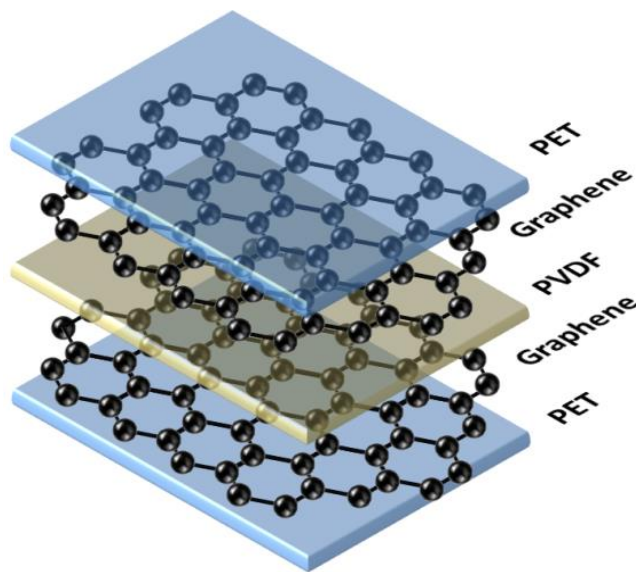


Figure 4. 1 (a) Fabrication process of the graphene/PVDF based multi-functional touch panel.



(b)



(c)

Figure 4.1 (b) structure of  $\beta$ -phase PVDF and (c) structure of the multi-functional touch panel.

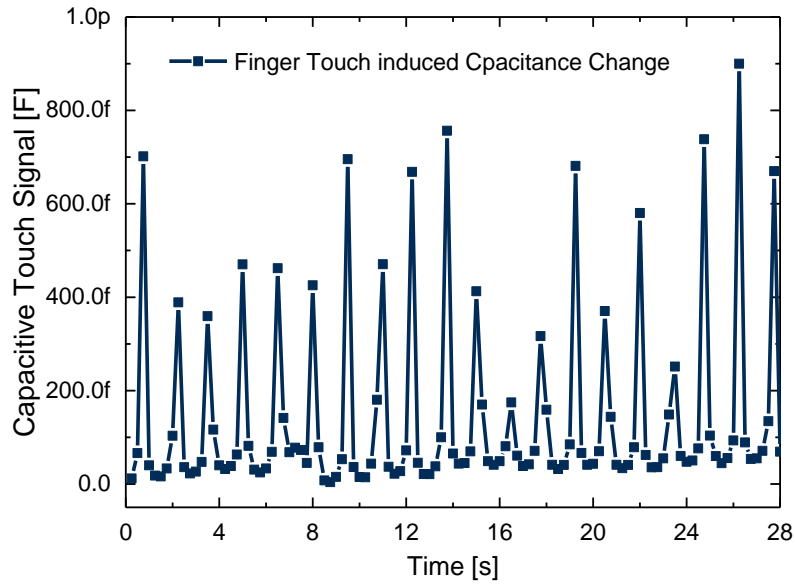
The fabricated touch panel is expected to be sensitive to changes in capacitance and force. To measure the change of capacitance, a parameter analyser (Keithley 4200 SCS) is used. Two scenarios of capacitive touch are performed and measured. In the first scenario conventional tapping touches are performed, indicating that the finger contacts the surface of the touch panel. In the second scenario, different layers of microscope slides (Thermo Fisher Scientific Inc.) are used to mimic a variety of distances for hover touch events. The thickness of each microscope slide is around 0.5 mm.

## **4.2 Touch Panel Measurement**

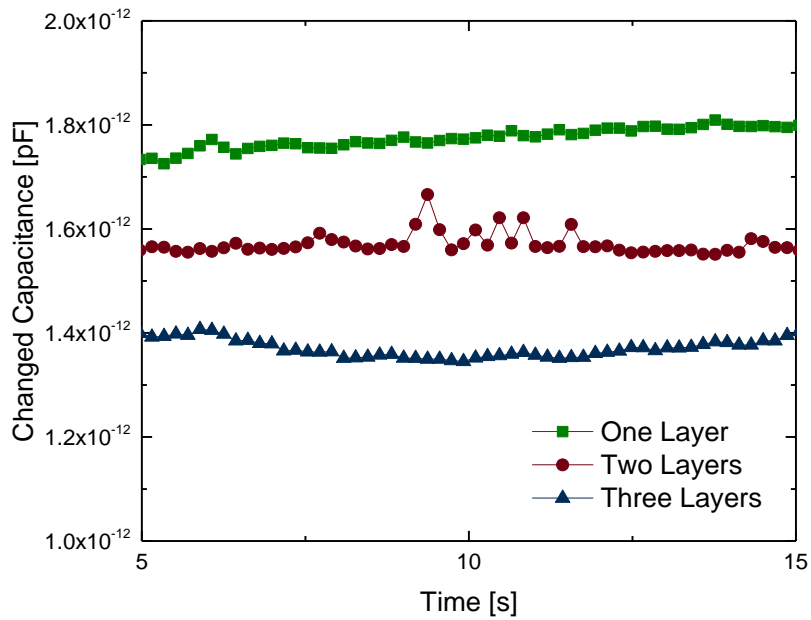
### **4.2.1 Capacitive Response to Human Finger Touch**

As mentioned above, two types of capacitive touch event are performed: the tapping (contact) touch and hover (non-contact) touch. For the tapping touch, the amplitude of minimum capacitive change is measured. This is because a touch panel system normally has a threshold set to determine whether or not a contact touch event happens. The minimum capacitance change can help in determining the threshold of registering the touch events. It should be noted here that the minimum capacitance change is not the minimum detectable capacitance change, which is related to many factors such as the AC measuring signal frequency and the noise floor.

A series of contact touches were performed; part of the experimental results is shown in Fig. 4.2 (a). As explained above, the intention of this experiment was to help estimate the touch detection threshold. Thus, the strength of the performed contact touches must be similar to conventional tapping touches with touch panels. The experimental results show that the minimum capacitance change caused by the finger contact touch was around 200 fF, which can be considered to be a threshold. Two factors related to the different capacitance values induced by the contact finger touches are the contact area ( $A$ ) and the distance. The contact area has a positive relationship with the applied force. In contrast, the distance between the finger to the sensing electrode ( $d_1$ ) and the distance between the sensing electrode and the driving electrode ( $d_2$ ) have a negative



(a)



(b)

Figure 4. 2 Experimental results of (a) tapping touch and (b) hover touch related events.

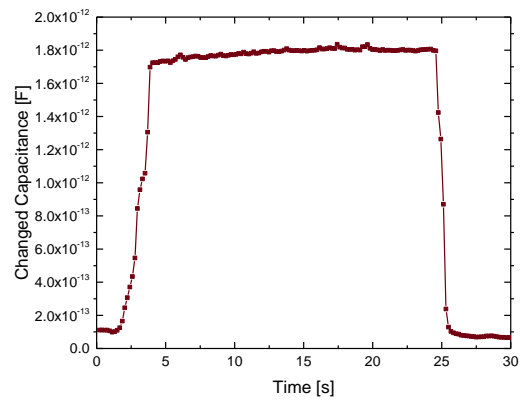
relationship with the strength of the applied force. The precise reduced distance value depends on the applied force, mechanical properties of the touch panel (such as Young's modulus and Poisson ratio of each layer) and boundary conditions (such as simply supported and fully clamped).

In terms of non-contact touches, different layers of plain microscope slides were used to control the distance between the finger and the touch panel. Each glass slide is around 0.5 mm thick. The experimental results are shown in Fig. 4.2 (b). It can be observed that the hover touch induced capacitance change decreases as the number of glass slides increases. The number of glass slides and the change in capacitance value are negatively correlated, which aligns with our expectation. The detailed experimental results of hover touch events are illustrated in Fig. 4.3. The experimental results demonstrated in Fig. 4.2 and Fig. 4.3 show that the fabricated touch panel can detect both contact and non-contact touch events, satisfying the needs of customers. The fluctuations in Fig. 4.2 (b) and Fig. 4.3 are caused by the unstable finger position. The differences in measured results from the four touch pads are within 5%.

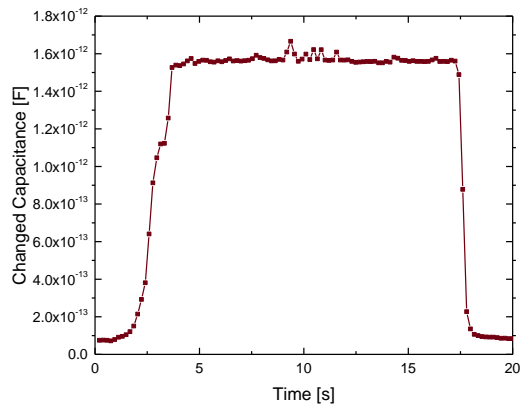
### **4.2.2 Force Response to Machine Stylus Touch**

To examine the performance of the fabricated touch panel in terms of its response to the force touch, a test-bed was built as shown in Fig. 4.4 (a). It consists of three main components: a 3-D position control system for the touch panel (Fig. 4.4 (b)), a stable force source, and an accurate force sensor (Fig. 4.4 (c)).

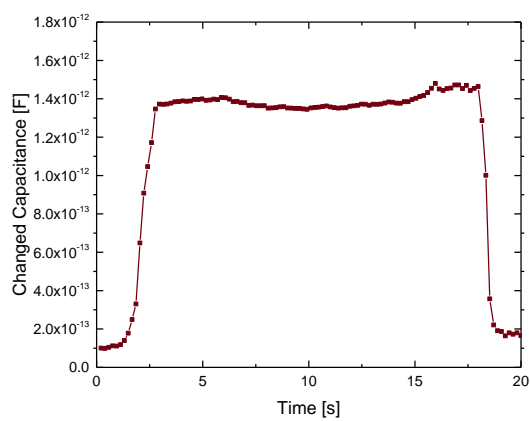
The 3-D position control system consists of three motors used to accurately control the position of the touch panel along the x-y-z axis. The resolution of the 3-D positioning system is 1 mm. A LabVIEW based graphic user interface (GUI) (Fig. 4.4 (d)) was designed to control the positioning system. After the touch panel was positioned properly, the shaker was started to provide a stable force touch signal. The stick of the shaker can be tuned from 0 to 90 degrees. In our measurement, the direction



(a)

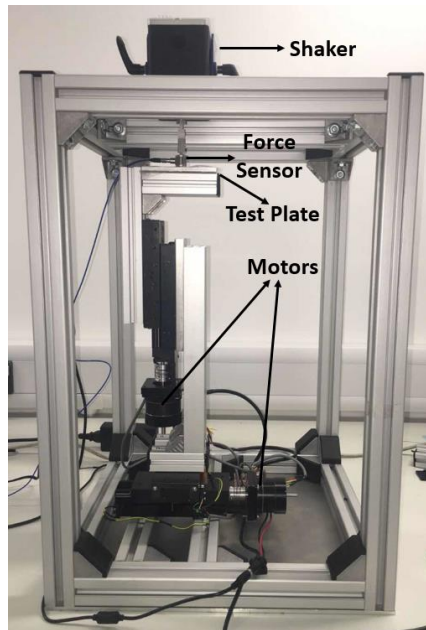


(b)

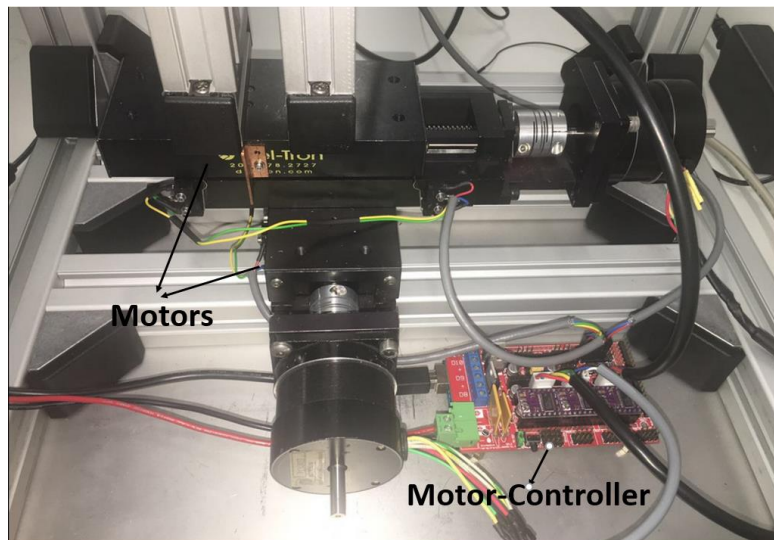


(c)

Figure 4. 3 Experimental results of hover touch events with (a) one, (b) two, and (c) three layers of plain microscope slides.

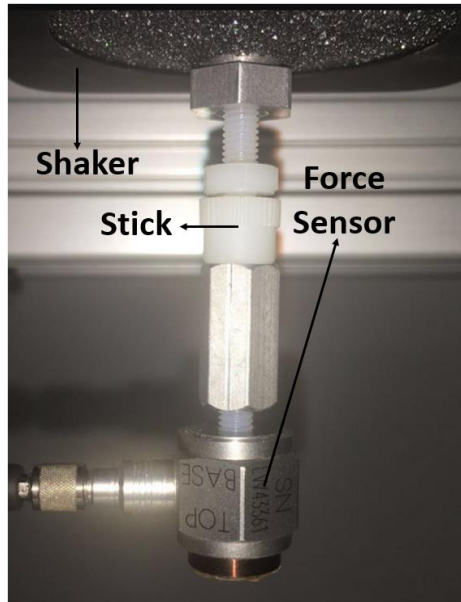


(a)

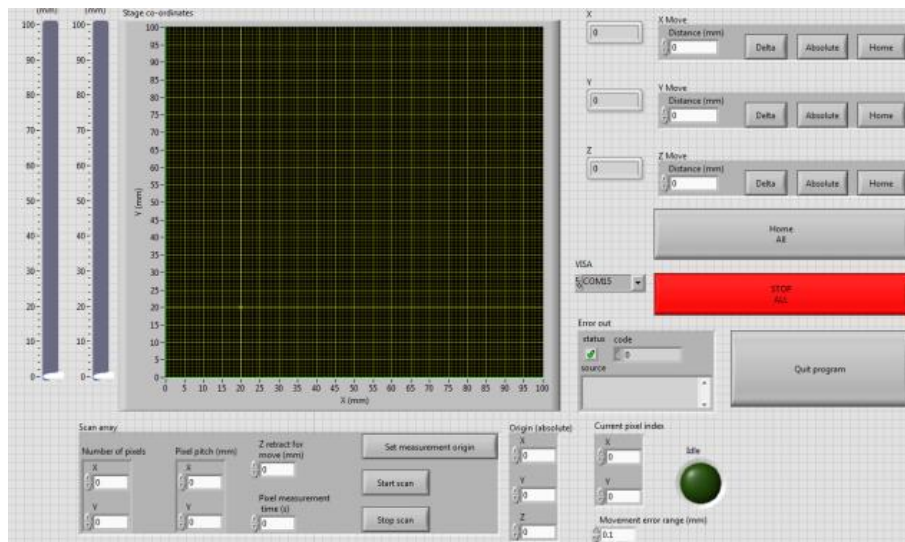


(b)

Figure 4. 4 (a) Test-bed for force touch experiment, and (b) three-motor controlled positioning system.

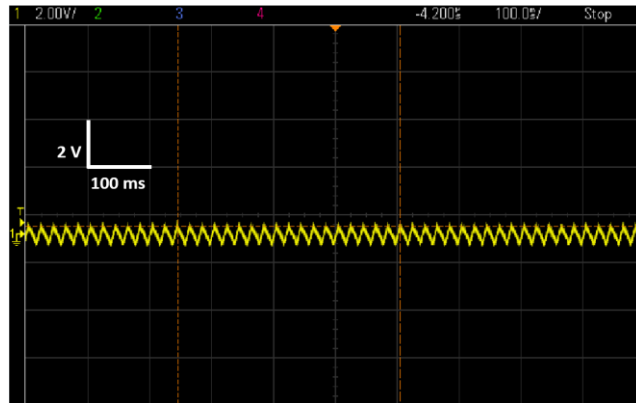


(c)

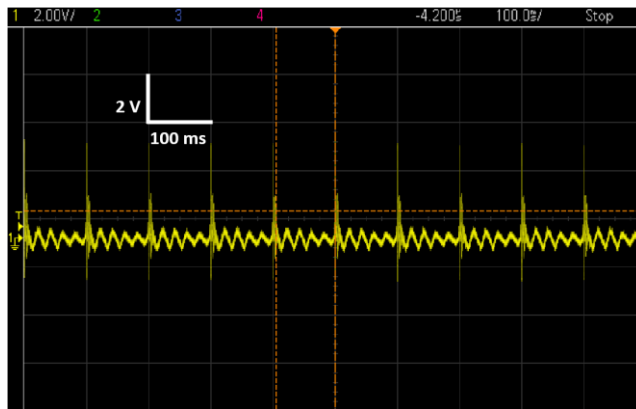


(d)

Figure 4.4. (c) Shaker stick mounted with a force sensor, LabVIEW based GUI for the 3-D positioning system.



(a)



(b)



(c)

Figure 4. 5 Experimental results of (a) charger noise; (b) force touch signal with charger noise; (c) force touch signal after charger noise cancellation.

of the stick was fixed at 90 degrees (perpendicular) to the fabricated touch panel. The strength of the force touch signal can be read by the force sensor mounted on the stick of the shaker, as shown in Fig 4.4 (c). By comparing output signals from the force sensor and the touch panel, the force/voltage coefficient of the fabricated touch panel could be calculated.

There are some limitations to the force touch measurement system. First, because the material of the plate holding the touch panel is conductive, strong environmental interference (e.g. charger noise) is coupled and hence disturbs the force touch measurement. As shown in Fig 4.5 (a), the peak to peak value of the charger noise can even exceed 1 V. When the force touch signal combined with the charger noise, it was difficult to read the accurate value (shown in Fig. 4.5 (b)). To solve this, the plate was connected to the ground of the oscilloscope. Fig. 4.5 (c) shows the result when the charger noise is cancelled out. Second, the plate is not fully fixed. When the stick of the shaker hits the touch panel, the plate moves together with the stick in a small distance. When the stick moves back, the plate rebounds as well, resulting in the loss of the negative part of the signal, as shown in Fig. 4.5 (c). This will be solved in a future design. For now, to keep the stage stable, the plate was manually held, and the frequency of the shaker was controlled to be 1 Hz (note, due to the functional limitations of the shaker, the shaker cannot provide a sinusoidal signal at low frequency range. Instead of a sinusoidal signal, the shaker produces an “impulse” signal). The results demonstrated in Fig. 4.6 show that both positive and negative components were obtained. The signal from channel 2 in Fig. 4.6 is the output from the commercial force sensor. By comparing the outputs from the commercial force sensor and the fabricated touch panel, the piezoelectric  $d_{33}$  coefficient of the fabricated touch panel can be obtained. In our measurement, 100 experiments were performed, and the averaged piezoelectric  $d_{33}$  coefficient was 0.092 V/N. This value is smaller than expected, we think a possible reason is because of the piezoelectric coefficient decreases during the lamination process. In lamination, high temperature (90 degree) is applied, hence the piezoelectric property is damaged a little bit.

As mentioned above, the direction of the stick was set to be perpendicular to the fabricated touch panel. However, in practical touch scenarios, the directions of touch

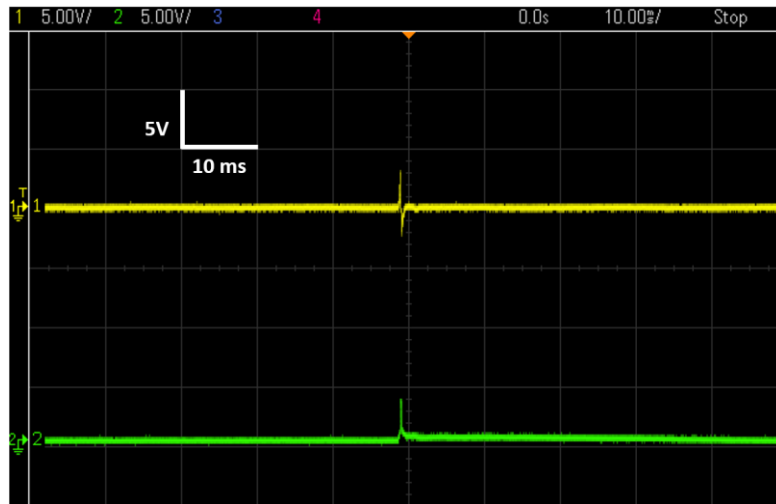


Figure 4. 6 Experimental results of force touch signal with “stabilized” plate.

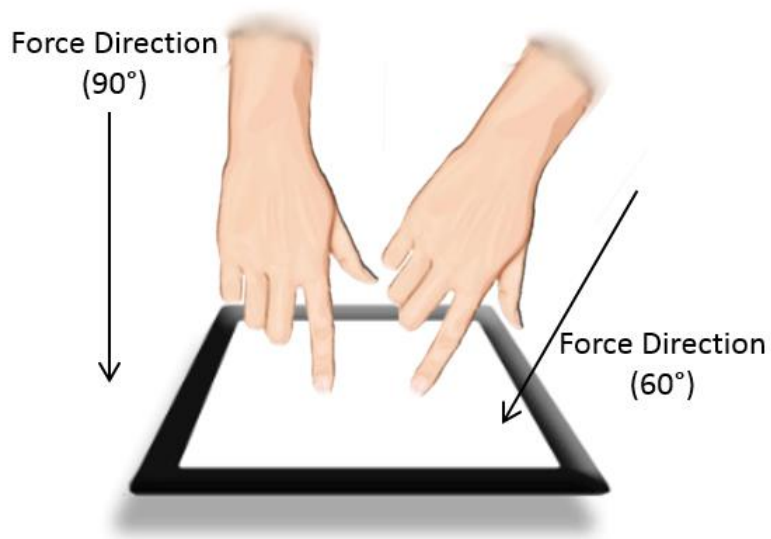


Figure 4. 7 Conceptual descriptions of touch events from different directions.

events are not always perpendicular to the touch panel, as conceptually shown in Fig. 4.7.

To investigate how the angle of a touch event affects the touch panel's output, two touch angles (80° and 70°) were performed. The experimental results are shown in Table 4.1. When touch angle is not normal, a portion of force will be divided into x-y plane, hence the force in z direction decreases, resulting in smaller force induced voltage.

<b>Touch Angle</b>	<b>V/N</b>
90°	0.092
80°	0.084
70°	0.069

Table 4. 1 Conceptual descriptions of touch events from different directions.

### **4.3 Conclusion**

In this chapter, the proposed multi-functional touch panel was fabricated and measured. CVD grown mono-layer graphene was used as the electrodes, which were then laminated with a commercial PVDF film to form the multi-functional touch panel. The capacitive touch response and force touch response of the fabricated touch panel were investigated. The experimental results showed that the fabricated touch panel can successfully detect capacitive and force touch events with high sensitivity (0.2 pF and 92 mV/N).

## Bibliography

- [1] Gao, S., Arcos, V. and Nathan, A., 2016. Piezoelectric vs. Capacitive Based Force Sensing in Capacitive Touch Panels. *IEEE Access*, 4, pp.3769-3774.
- [2] Gao, S. and Nathan, A., 2016, May. P - 180: Force Sensing Technique for Capacitive Touch Panel. In *SID Symposium Digest of Technical Papers* (Vol. 47, No. 1, pp. 1814-1817).
- [3] Wu, X., Zhong, G., D'Arsié, L., Sugime, H., Esconjauregui, S., Robertson, A.W. and Robertson, J., 2016. Growth of continuous monolayer graphene with millimeter-sized domains using industrially safe conditions. *Scientific reports*, 6.
- [4] Nair, R.R., Blake, P., Grigorenko, A.N., Novoselov, K.S., Booth, T.J., Stauber, T., Peres, N.M. and Geim, A.K., 2008. Fine structure constant defines visual transparency of graphene. *Science*, 320(5881), pp.1308-1308.
- [5] Lee, S.K., Kim, B.J., Jang, H., Yoon, S.C., Lee, C., Hong, B.H., Rogers, J.A., Cho, J.H. and Ahn, J.H., 2011. Stretchable graphene transistors with printed dielectrics and gate electrodes. *Nano letters*, 11(11), pp.4642-4646.
- [6] Liu, Z., Liu, Q., Huang, Y., Ma, Y., Yin, S., Zhang, X., Sun, W. and Chen, Y., 2008. Organic photovoltaic devices based on a novel acceptor material: graphene. *Advanced Materials*, 20(20), pp.3924-3930.
- [7] Han, T.H., Lee, Y., Choi, M.R., Woo, S.H., Bae, S.H., Hong, B.H., Ahn, J.H. and Lee, T.W., 2012. Extremely efficient flexible organic light-emitting diodes with modified graphene anode. *Nature Photonics*, 6(2), pp.105-110.

- [8] Kim, R.H., Bae, M.H., Kim, D.G., Cheng, H., Kim, B.H., Kim, D.H., Li, M., Wu, J., Du, F., Kim, H.S. and Kim, S., 2011. Stretchable, transparent graphene interconnects for arrays of microscale inorganic light emitting diodes on rubber substrates. *Nano letters*, 11(9), pp.3881-3886.
- [9] Rogers, J.A., 2008. Electronic materials: Making graphene for macroelectronics. *Nature nanotechnology*, 3(5), pp.254-255.
- [10] Bonaccorso, F., Sun, Z., Hasan, T. and Ferrari, A.C., 2010. Graphene photonics and optoelectronics. *Nature photonics*, 4(9), pp.611-622.
- [11] Bae, S.H., Lee, Y., Sharma, B.K., Lee, H.J., Kim, J.H. and Ahn, J.H., 2013. Graphene-based transparent strain sensor. *Carbon*, 51, pp.236-242.
- [12] Lee, C., Wei, X., Kysar, J.W. and Hone, J., 2008. Measurement of the elastic properties and intrinsic strength of monolayer graphene. *science*, 321(5887), pp.385-388.
- [13] Novoselov, K.S., Fal, V.I., Colombo, L., Gellert, P.R., Schwab, M.G. and Kim, K., 2012. A roadmap for graphene. *Nature*, 490(7419), pp.192-200.
- [14] <http://www.mit.edu/~6.777/matprops/ito.htm>, last retrieved on 30<sup>th</sup> Sept 2017.

# Chapter 5 Algorithms for Force Touch Signal

---

A theoretical analysis of the mechanical and electrical properties of the proposed technique was performed in chapter 3 in order to validate it, following which a graphene based touch panel was fabricated and tested in chapter 4. From the experimental results illustrated in chapter 4, it was learned that the fabricated touch panel can provide good force and capacitive touch detection sensitivity. Chapter 3 demonstrated that the capacitive touch signal and force touch signal can be separated by using their frequency properties. More specifically, the force touch signal takes the low frequency range (within 1 kHz), while the capacitive signal occupies a relatively high frequency range of 100 kHz. After separating these two signals, the next step is to interpret them. This chapter focuses on developing algorithms to interpret the force touch signal.

First, the strength of the applied force touch signal is addressed. Here the force touch signal can be divided into two scenarios: dynamic force touch events and static force touch events. As a piezoelectric material, PVDF can detect dynamic force touch signals [1]–[12]. However, it is unable to detect a static force signal, as explained in chapter 2. This chapter designs interpretation algorithms to realize both dynamic and static force touch sensing.

Second, stress propagation is a practical issue for the PVDF based touch panel in detecting force touch events. More specifically, the stress caused by a force touch in one location can propagate to adjacent locations. Although the propagated stress can be small, it is difficult for the system to distinguish whether the detected signal at a specific

location is generated from a real touch event at this location, or propagated from other force touch locations. The algorithm developed in this chapter overcomes this issue as well.

Third, power consumption is a critical issue in electronics. In the later part of this chapter, an algorithm is proposed and demonstrated that can concurrently detect force touch signals and harvest force touch generated electrical energy.

## **5.1 Algorithms for Force Touch Interpretation**

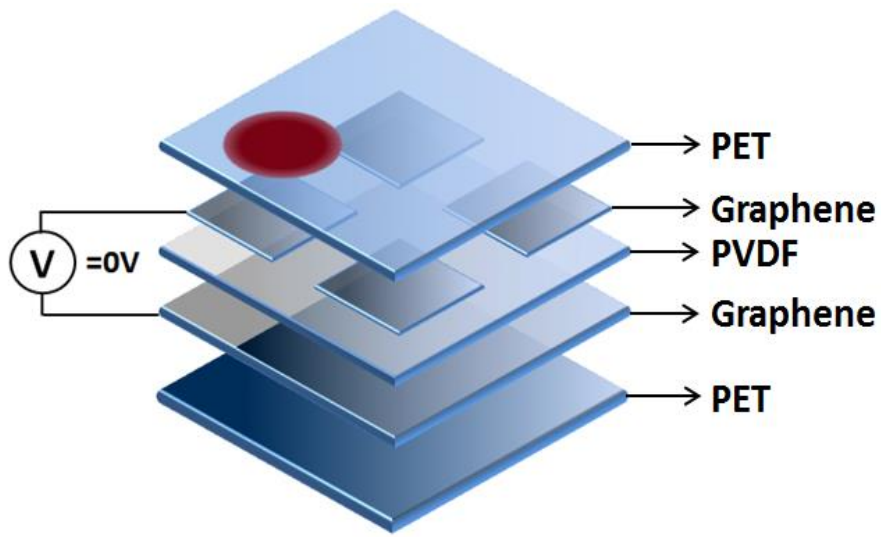
As mentioned before in chapter 4, one piece of graphene was patterned into four small square areas, which represent four touch pads. The other piece of graphene was maintained and works as a ground layer. PVDF film was settled in between the two graphene layers, functioning as an insulating layer for the graphene based capacitor and the force detection and energy harvesting layer by generating force induced charges. The main drawback of using PVDF, or any other piezoelectric material, for force sensing is its inability to detect static force due to thermal drift and current dissipation [6]. Furthermore, when a force touch occurs at one location, mechanical stress can propagate to adjacent areas. The amount of propagated stress depends on the mechanical properties of the touch panel and the character of the applied force touch. Although the transferred mechanical stress and induced charges are sometimes small, it is difficult to distinguish whether they have been induced by a light touch or by an adjacent heavy touch. Hence, the propagated stress may give rise to force touch misregistrations. These two issues are shown in Fig. 5.1.

To solve these two issues, capacitive signals are used. For the former, the existence of a capacitive signal can be used to indicate a static force signal, as these two signals are generated together by a force finger touch. Thus, although the force signal may fall to zero, or below a certain threshold, as long as the capacitive touch signal is detected, the force touch is assumed to be maintained at the same level as its peak value. This is

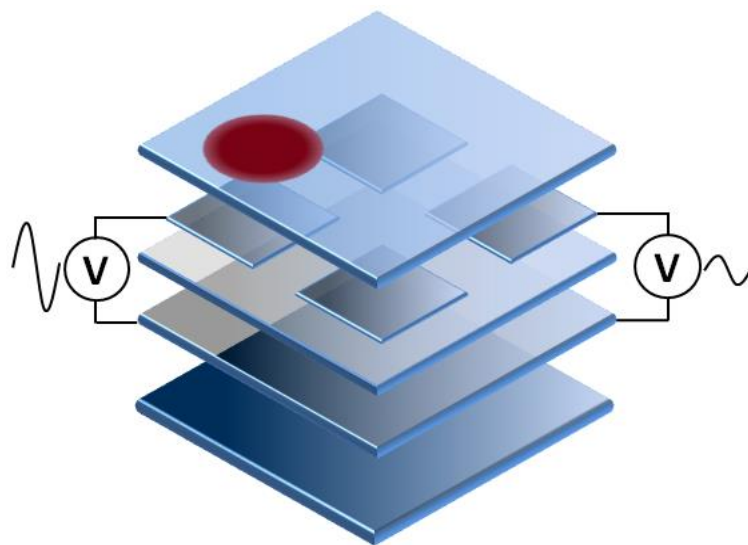
conceptually shown in Fig. 5.2. In Fig. 5.2 (a), the static force touch lasts within the time period  $t_1$  to  $t_1+\Delta t_2$ , however, the force touch signal is only detected during the time period  $t_1$  to  $t_1+\Delta t_1$ . After applying the algorithm, if a capacitive touch signal is detected, then the force is assumed to be maintained.

As to force touch mis-registration due to propagated stress from adjacent force touches, the capacitive touch signal is also employed to distinguish a real finger force touch signal from a fake one. This is achieved based on the fact that when a location experiences propagated stress from adjacent force touches, its capacitance does not change dramatically. Thus, if there is no capacitive touch signal at a specific location, we assume that there is no finger based force touch, even if the readout shows an observable force signal. This is conceptually described in Fig. 5.3. A truth table of force and capacitive touch signals is explained in Table 5.1, and the algorithm flow chart is described in Fig. 5.4.

To implement the designed algorithms, a touch panel system was assembled as shown in Fig. 5.5 (a) and (b). First the static force touch interpretation algorithm was applied. The force touch and capacitive touch signal output from a single channel is shown in Fig. 5.6 (a) and (b). Fig. 5.6 (a) and (b) show that static force touch is detected, and that the force is maintained during the static force touch period. A larger capacitance signal is obtained when a stronger force touch occurs. This is because when a stronger finger touch occurs, normally the contact area between the touch panel and human finger becomes larger, resulting in a bigger capacitive signal. In Fig.5.6 (c) and (d), outputs from two adjacent channels are plotted. The figure shows that, when a force touch occurs at sensor 1, the propagated stress can give rise to a light force signal at sensor 2, resulting in potential force touch mis-registration. In contrast, the capacitive signals at the adjacent sensors are very small, thus can be used as determination signals for force touch detection. After applying the propagated stress elimination algorithm, the issue is solved as shown in Fig. 5.6 (e).



(a)



(b)

Figure 5. 1 Two issues of piezoelectric-based force touch sensing in a touch panel. (a) Static force touch is not detected. (b) Propagated stress induced charge may result in force touch mis-registration. The red circles indicate the force touch positions. The forces are static force and dynamic force in (a) and (b), respectively.

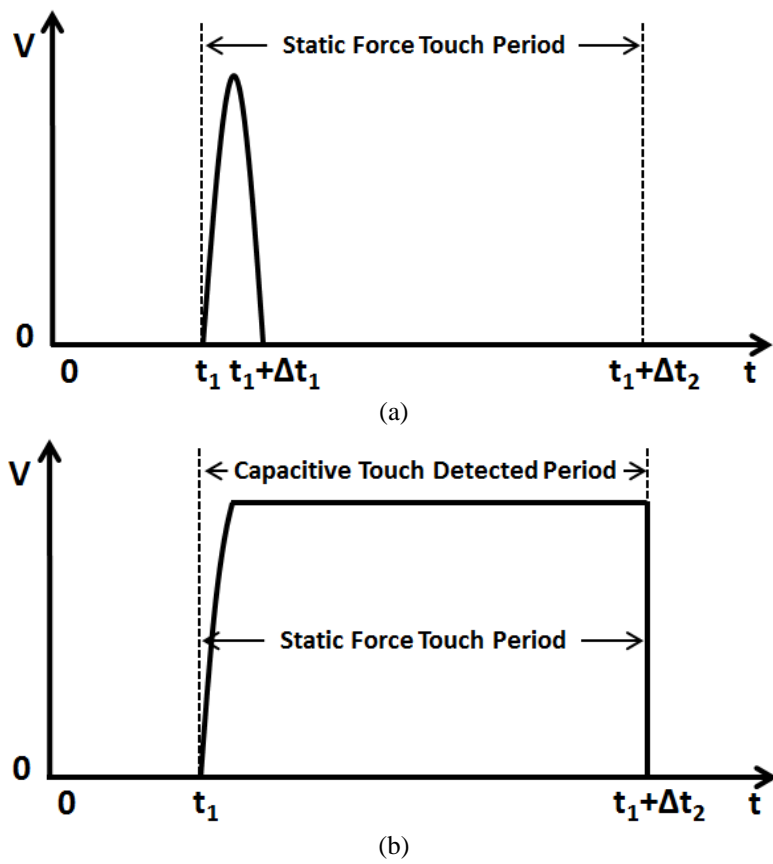


Figure 5. 2 Conceptual output of the static force detection algorithm.

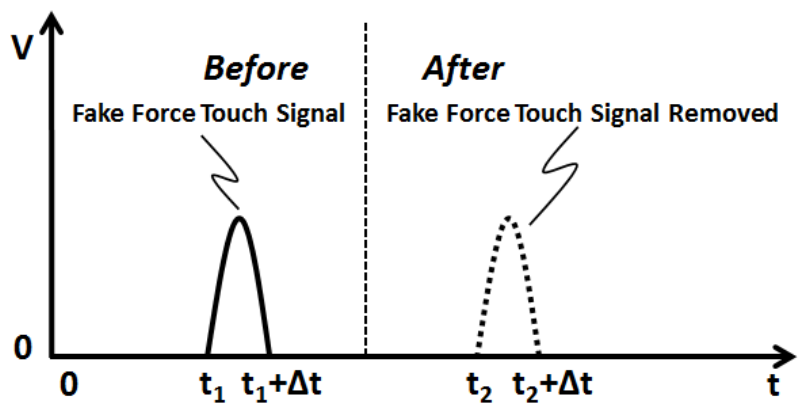


Figure 5. 3 Conceptual outputs of the fake force touch signal before and after the algorithm.

Input		Output	
$T_{\text{Capacitive}}$	$T_{\text{Force}}$	$T_{\text{Capacitive}'}$	$T_{\text{Force}'}$
0	0	0	0
0	1	0	0
1	0	1	0
1	1	1	1

Table 5. 1 Truth table of force and capacitive touch signals.

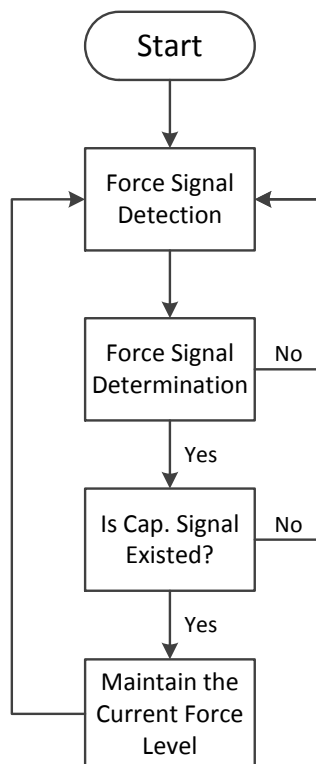
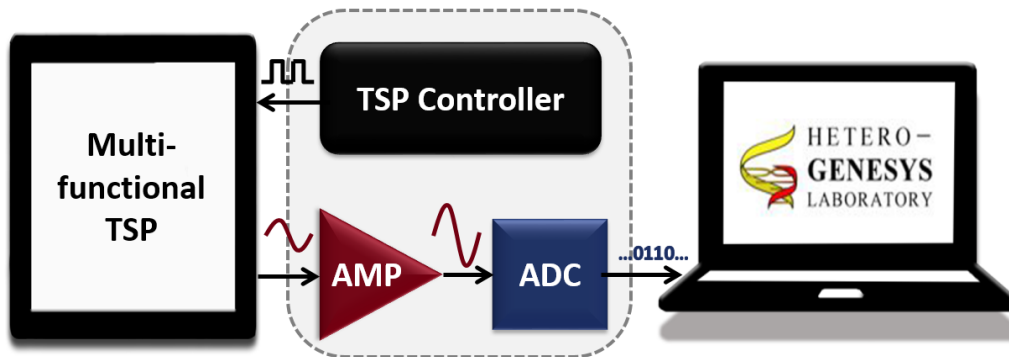
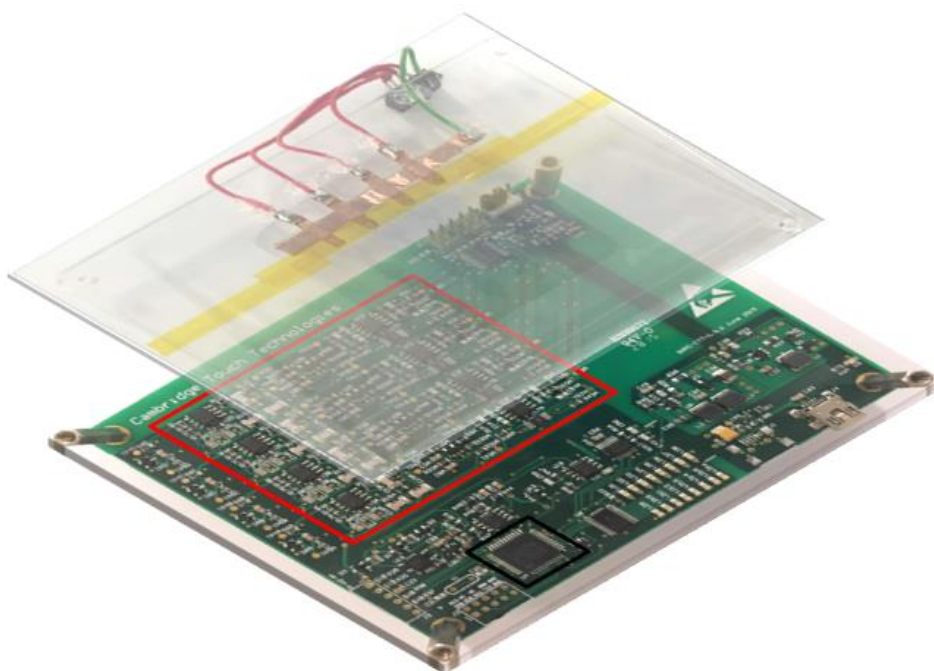


Figure 5. 4 Flow chart of the force detection algorithm.

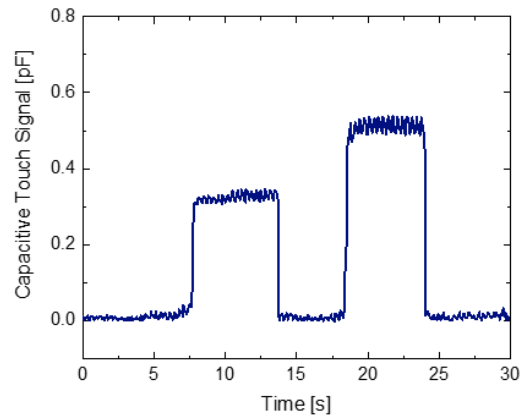
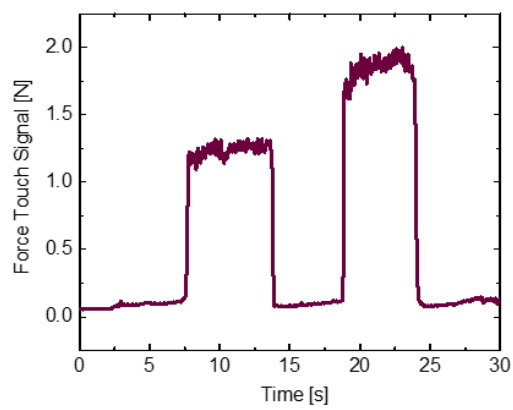


(a)



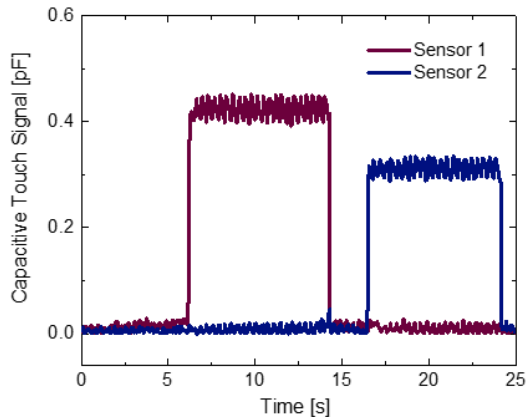
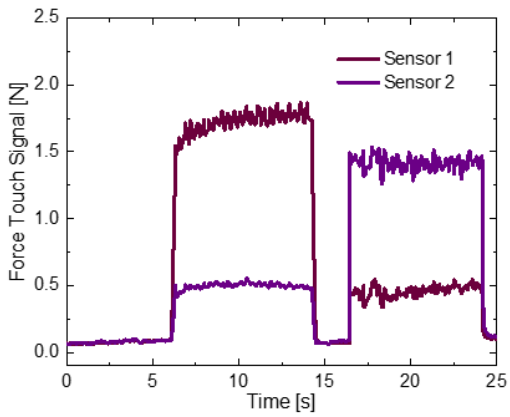
(b)

Figure 5. 5 (a)–(b) System diagram and interface circuit.



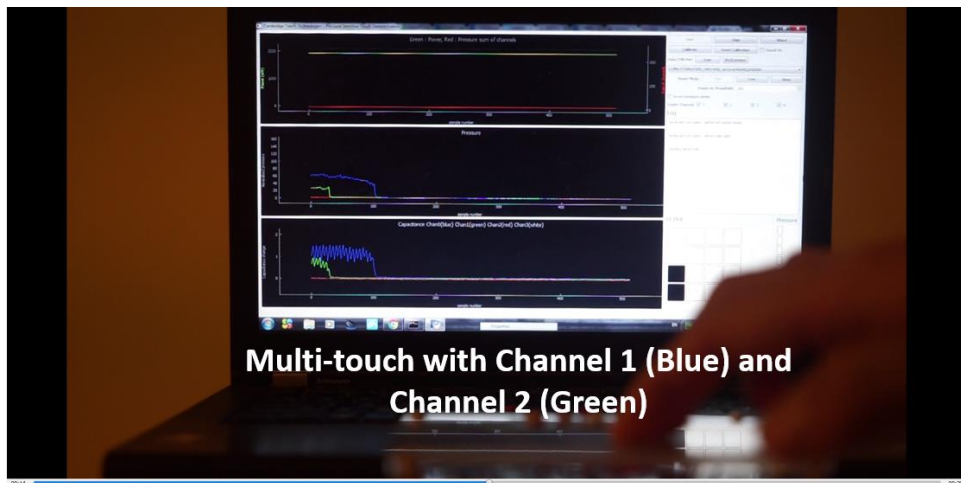
(a)

(b)



(c)

(d)



**Multi-touch with Channel 1 (Blue) and Channel 2 (Green)**

(e)

Figure 5. 6 (a)–(b) Force and capacitive signals output from a single channel of the system. (c)–(d) Force and capacitive signals output from two adjacent channels of the system before the propagated stress elimination algorithm is applied. (e) Screen capture of the software.

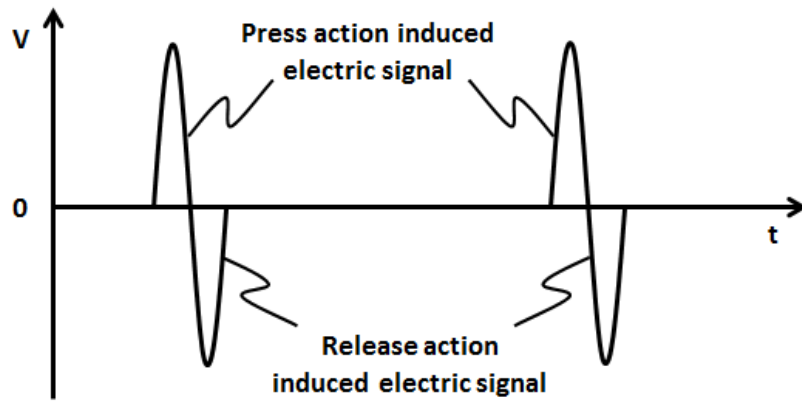
## 5.2 Energy Harvesting

Energy consumption is a practical and critical issue in today's electronic devices. In smart phones, high power consumption, mainly caused by 3G (~31%), display (~24%), and Wi-Fi (~24%) [13] components, shortens the lifetime of the battery, giving rise to the popularity of portable charging devices [14]. Many low power consumption techniques have been proposed and implemented [15]–[20]. In addition to these, energy harvesting techniques are attracting attention. Traditional energy-harvesting techniques in smart phones are based on collecting RF, solar and thermoelectric related energy. However, harvested RF energy is only approximately  $0.1 \mu\text{W}/\text{cm}^3$  [21], strong sunlight is needed for collecting solar energy, and thermoelectric energy requires stable heat sources, which are not convenient for customers [21]. Thus, a green and convenient energy harvesting technique is required for smart phones.

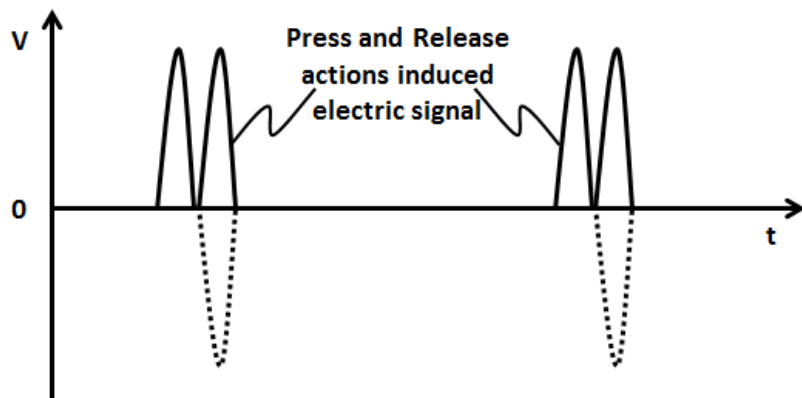
As mentioned previously in chapter 2, the force induced charge can be employed to interpret the force level, or be stored for future use. The previous section demonstrated how the force induced charge is used for distinguishing the force level. This section provides a simple energy harvesting system, and the harvested energy is then used to light a blue LED.

### 5.2.1 Piezoelectric Based Energy Harvesting System

As conceptually shown in Fig. 5.7, the piezoelectric material based force induced electric signal has positive and negative components because the polarization changes twice during a whole press and release finger touch procedure. This kind of signal cannot be directly stored in an energy storage component such as a capacitor, because the negative part will compensate for the positive part. A single Diode based rectifier circuit can be used to block the negative part, as shown in Fig. 5.8 (a). However, blocking the negative part wastes half of the mechanical (force) energy transformed to electrical energy. Thus, a bridge rectifier circuit as shown in Fig. 5.8 (b) is employed to fully collect the energy. The conceptual output after the bridge rectifier is described in



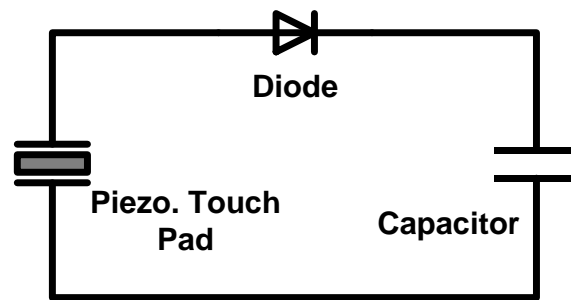
(a)



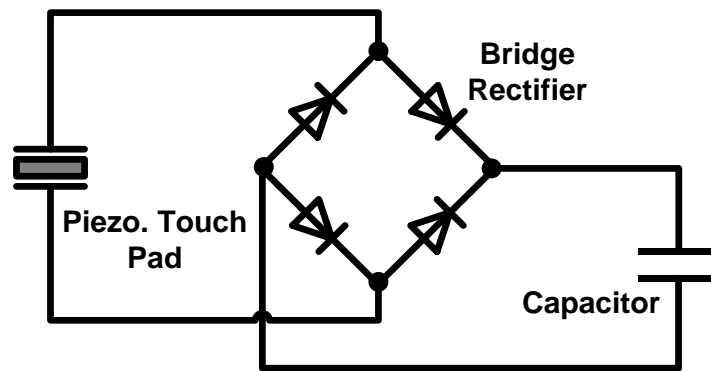
(b)

Figure 5. 7 Conceptual piezoelectric based finger touch signal.

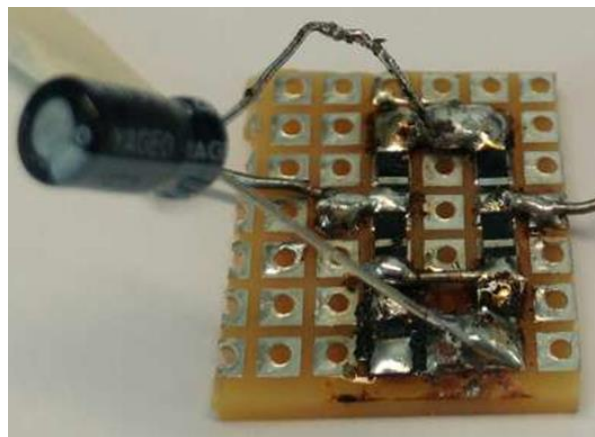
Fig. 5.7 (b), and the collected energy in the capacitor is shown in Fig. 5.9. In Fig. 5.9 (a), the charging and discharging periods are clearly shown. After each force touch the capacitor is charged by a little bit. Zooming-in on the charging period shows that there are two charging moments during a single force touch. Because the polarization alters twice, the energy in the negative part is also collected by the bridge rectifier, and used to charge the capacitor.



(a)

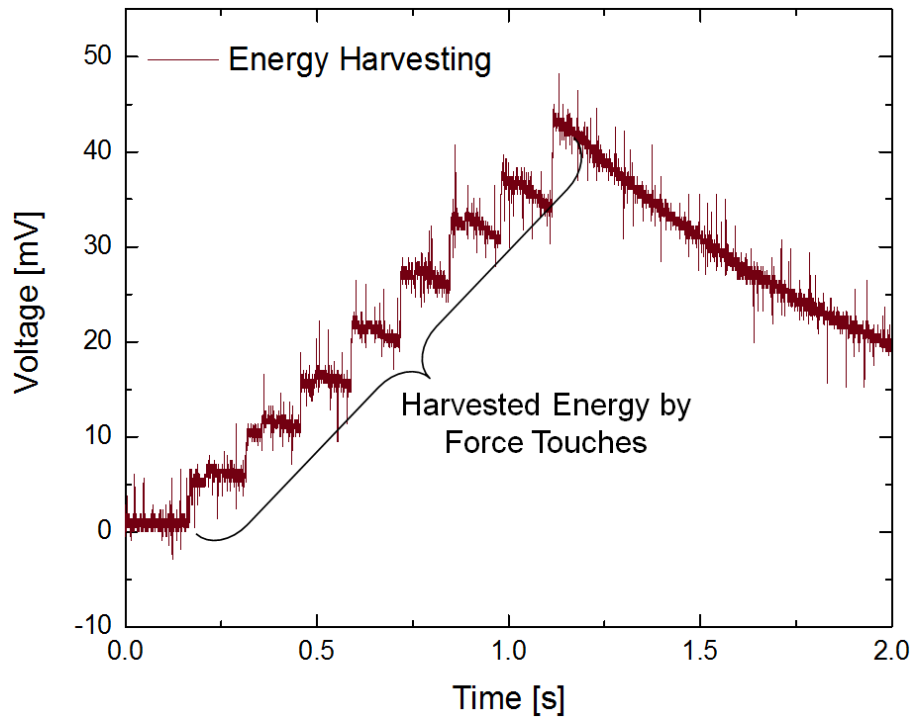


(b)

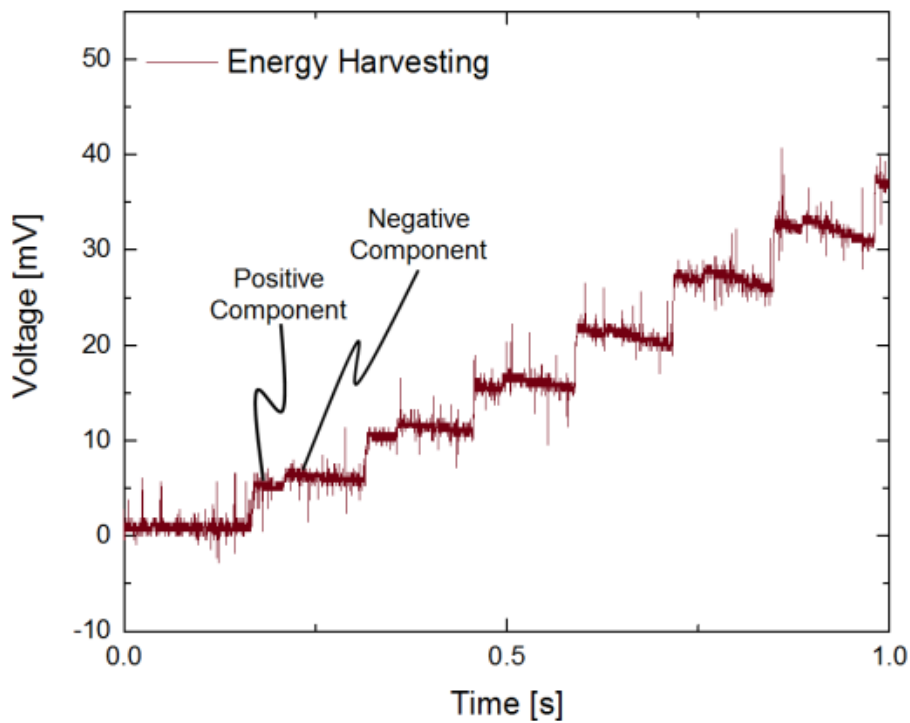


(c)

Figure 5. 8 (a) Single diode based rectifier circuit; (b) four diodes based bridge rectifier circuit; (c) Practical rectifier circuit.



(a)



(b)

Figure 5. 9 (a) Charging and discharging period; (b) Details of the charging period.

The above demonstrates that force induced charges can be used to charge a capacitor, thus, when the software application doesn't need to read force information, the force induced charge can be used for energy harvesting. It is also possible to read the force signal and do energy harvesting at the same time. For example, the positive part can be used for force signal detection, and the negative part used for energy harvesting, as shown in Fig. 5.10.

Fig. 5.10 (a) shows that the force detection circuit and energy harvesting circuit share the same ground. Both use half of the energy generated by force touches. To illustrate these two functions, the force detection circuit and the energy harvesting circuit were connected to an oscilloscope, as shown in Fig. 5.10 (b). The corresponding touch signal and energy harvesting signal are shown in Fig. 5.10 (c), respectively. Force detection and energy harvesting were achieved at the same time. In practical circuit design, a charge amplifier is widely used to read the force touch signal, due to the high impedance of the PVDF sample. Since the oscilloscope is already equipped with high impedance, no charge amplifier was used in this demonstration.

To calculate how much total energy is stored in the capacitor, the following equation can be used:

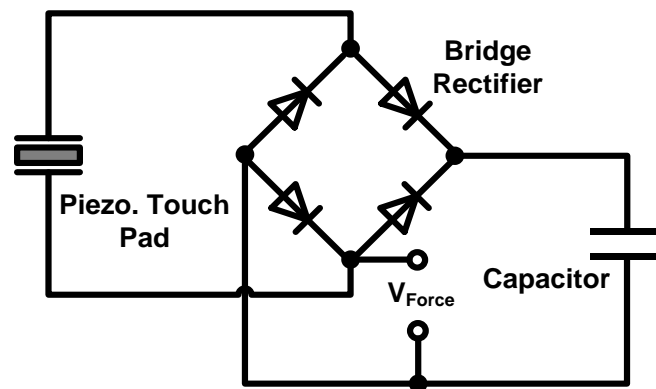
$$E_{E.H.} = \frac{1}{2} CV^2; \quad (5.1)$$

where  $E_{E.H.}$  is the energy stored in the capacitor,  $C$  denotes the capacitance of the capacitor, and  $V$  represents the voltage across the capacitor. To calculate the stored energy in Fig. 5.9 (a), the following values for the variables can be used in Eq. 5.1:  $C$  is equal to 1  $\mu\text{F}$  and  $V$  is around 45 mV. Thus,  $E_{E.H.}$  is 1.03 nJ based on the equation. To calculate the energy harvested by a single force touch, the following equation can be employed:

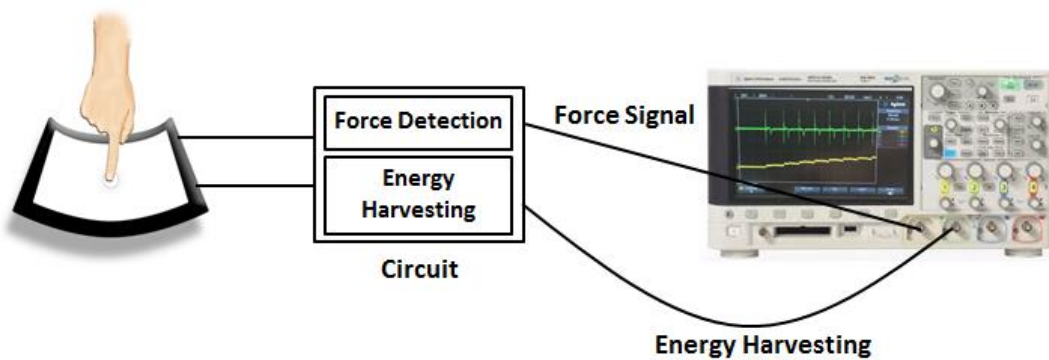
$$\Delta E_{E.H.} = \frac{1}{2} C(V' - V)^2; \quad (5.2)$$

where  $\Delta E_{E.H.}$  indicates the energy stored by a single force touch, and  $\Delta V$  represents the voltage change after a single force touch.

Because of the high impedance of the PVDF based touch panel, the energy generated by the force touch cannot be efficiently transferred and stored in the capacitor. To solve this issue, a Maximum Power Point Tracking (MPPT) circuit is normally used.

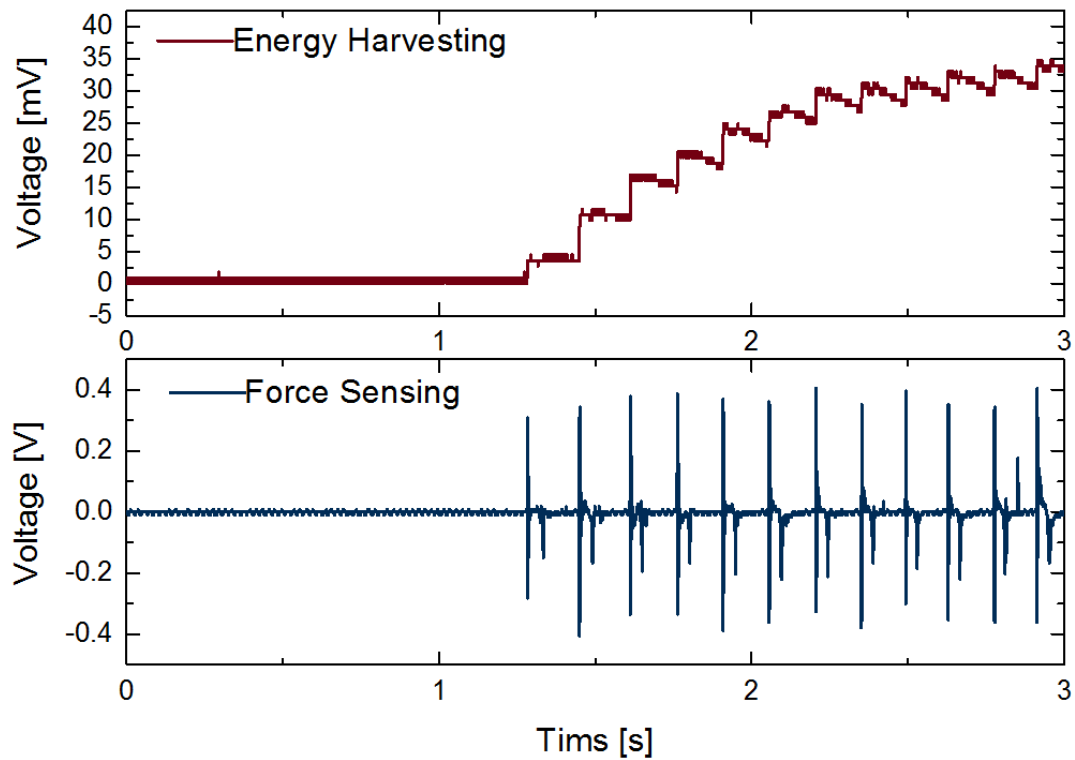


(a)



(b)

Figure 5. 10 (a) Circuit for force detection and energy harvesting. (b) Configuration of the touch panel, circuit, and oscilloscope.



(c)

Figure 5. 11 Simultaneous force touch signal and energy harvesting.

However, this thesis is mainly concerned with demonstrating this function in a touch panel, thus MPPT circuits are not employed.

Based on the work presented in this section, the functionalities in our touch panel expand from two (capacitive and force sensing) to three, including energy harvesting, as shown in Fig. 5.11.

### 5.3 Conclusion

This chapter has designed and implemented the interpretation algorithm and energy harvesting algorithms. The force touch interpretation algorithm addresses two issues facing the piezoelectric materials based force touch panel: static force sensing,

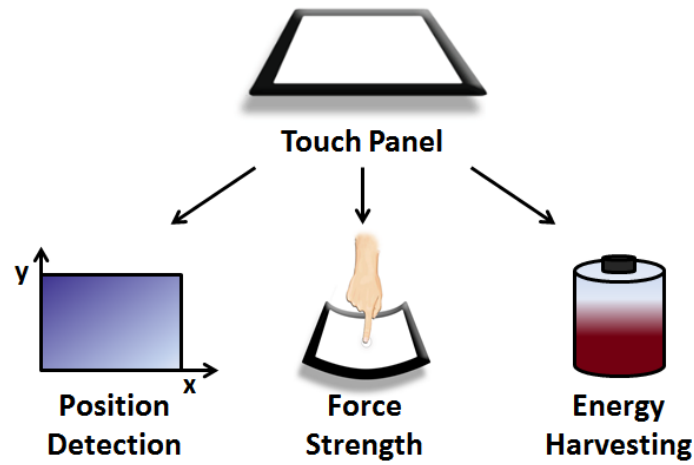


Figure 5. 12 Three functions in the touch panel are position detection (by capacitive sensing), force detection and energy harvesting.

and stress propagation. The energy harvesting algorithm achieved both energy harvesting and force touch detection by using the altered polarizations of piezoelectric materials during force touch events. Furthermore, the accuracy and resolution for force touch detection are maintained.

Detection of the capacitive signal in terms of accuracy and readout speed are vital to the force touch interpretation algorithm. Thus, the following chapter develops performance optimization algorithms for capacitive touch detection.

## Bibliography

- [1] Cha, S., Kim, S.M., Kim, H., Ku, J., Sohn, J.I., Park, Y.J., Song, B.G., Jung, M.H., Lee, E.K., Choi, B.L. and Park, J.J., 2011. Porous PVDF as effective sonic wave driven nanogenerators. *Nano letters*, 11(12), pp.5142-5147.
- [2] Chang, C., Tran, V.H., Wang, J., Fuh, Y.K. and Lin, L., 2010. Direct-write piezoelectric polymeric nanogenerator with high energy conversion efficiency. *Nano letters*, 10(2), pp.726-731.
- [3] Choi, S.W., Jo, S.M., Lee, W.S. and Kim, Y.R., 2003. An electrospun poly (vinylidene fluoride) nanofibrous membrane and its battery applications. *Advanced Materials*, 15(23), pp.2027-2032.
- [4] Furukawa, T., 1989. Ferroelectric properties of vinylidene fluoride copolymers. *Phase Transitions: A Multinational Journal*, 18(3-4), pp.143-211.
- [5] Arokia, N. and Baltes, H., 1999. Microtransducer CAD, Physical and Computational Aspects.
- [6] Cain, M.G. ed., 2014. *Characterisation of ferroelectric bulk materials and thin films* (Vol. 2). Netherlands: Springer.
- [7] Fujisaki, S., Ishiwara, H. and Fujisaki, Y., 2007. Low-voltage operation of ferroelectric poly (vinylidene fluoride-trifluoroethylene) copolymer capacitors and metal-ferroelectric-insulator-semiconductor diodes. *Applied Physics Letters*, 90(16), p.162902.
- [8] Kepler, R.G. and Anderson, R.A., 1992. Ferroelectric polymers. *Adv. Phys*, 41, 1-57.

- [9] Xu, Y, 2013. Ferroelectric materials and their applications. *Elsevier*.
- [10] He, X. and Yao, K., 2006. Crystallization mechanism and piezoelectric properties of solution-derived ferroelectric poly (vinylidene fluoride) thin films. *Applied physics letters*, 89(11), p.112909.
- [11] Sodano, H.A., Inman, D.J. and Park, G., 2004. A review of power harvesting from vibration using piezoelectric materials. *Shock and Vibration Digest*, 36(3), pp.197-206.
- [12] Mohammadi, B., Yousefi, A.A. and Bellah, S.M., 2007. Effect of tensile strain rate and elongation on crystalline structure and piezoelectric properties of PVDF thin films. *Polymer testing*, 26(1), pp.42-50.
- [13] Carroll, A. and Heiser, G., 2010, June. An Analysis of Power Consumption in a Smartphone. In *USENIX annual technical conference* (Vol. 14, pp. 21-21).
- [14] Gao, S., Lai, J., Micou, C. and Nathan, A., 2016. Reduction of Common Mode Noise and Global Multivalued Offset in Touch Screen Systems by Correlated Double Sampling. *Journal of Display Technology*, 12(6), pp.639-645.
- [15] Gao, S., Lai, J. and Nathan, A., 2016. Fast Readout and Low Power Consumption in Capacitive Touch Screen Panel by Downsampling. *Journal of Display Technology*, 12(11), pp.1417-1422.
- [16] Mehendale, M., Das, S., Sharma, M., Mody, M., Reddy, R., Meehan, J., Tamama, H., Carlson, B. and Polley, M., 2012, February. A true multistandard, programmable, low-power, full HD video-codec engine for smartphone SoC. In *Solid-*

*State Circuits Conference Digest of Technical Papers (ISSCC), 2012 IEEE International* (pp. 226-228). IEEE.

[17] Sampson, A., Dietl, W., Fortuna, E., Gnanapragasam, D., Ceze, L. and Grossman, D., 2011, June. EnerJ: Approximate data types for safe and general low-power computation. In *ACM SIGPLAN Notices* (Vol. 46, No. 6, pp. 164-174). ACM.

[18] Gomez, C., Oller, J. and Paradells, J., 2012. Overview and evaluation of bluetooth low energy: An emerging low-power wireless technology. *Sensors*, 12(9), pp.11734-11753.

[19] Cuervo, E., Balasubramanian, A., Cho, D.K., Wolman, A., Saroiu, S., Chandra, R. and Bahl, P., 2010, June. MAUI: making smartphones last longer with code offload. In *Proceedings of the 8th international conference on Mobile systems, applications, and services* (pp. 49-62). ACM.

[20] Li, D. and Halfond, W.G., 2014, June. An investigation into energy-saving programming practices for android smartphone app development. In *Proceedings of the 3rd International Workshop on Green and Sustainable Software* (pp. 46-53). ACM.

[21] Fan, P.M.Y., Wong, O.Y., Chung, M.J., Su, T.Y., Zhang, X. and Chen, P.H., 2015, August. Energy harvesting techniques: Energy sources, power management and conversion. In *Circuit Theory and Design (ECCTD), 2015 European Conference on* (pp. 1-4). IEEE.

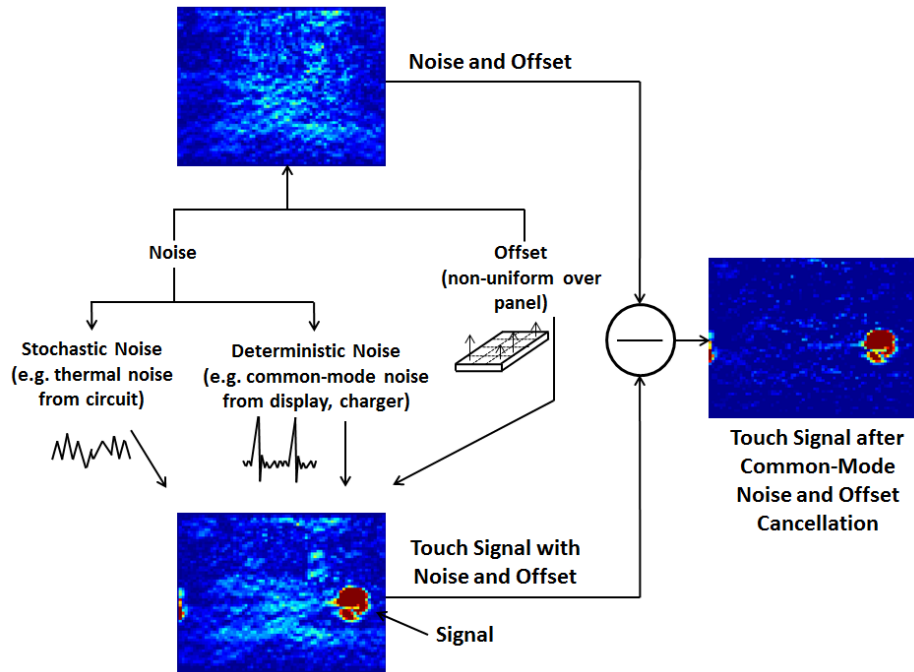
# **Chapter 6 Signal Processing Algorithms for Capacitive Touch Signal Optimization**

---

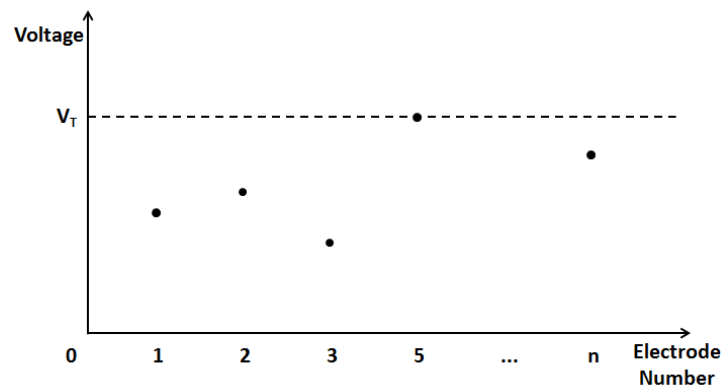
In the previous section, in our proposed force touch interpretation algorithms for static force touch detection and “fake” force touch elimination, the capacitive touch signal is a key factor. Both detection of static force touch and remove of “fake” force touch rely on the accuracy and readout speed of the capacitive signal. In capacitive touch panels, two main factors affecting detection accuracy and readout speed are noise and number of scanned electrodes. The detection accuracy can be represented by the system’s signal-to-noise ratio (SNR). Boosting the signal power or reducing the noise power can both give rise to an increment of SNR value. To avoid high power consumption, the reduction of noise power is more preferred. In this section, image processing based algorithms are proposed and implemented for noise reduction. For the purpose of applying the algorithms to commercial touch panel products, the algorithms developed are based on experimental data generated from a blackberry’s test-bed.

## **6.1 Reduction of Common Mode Noise and Global Multi-valued Offset in Touch Screen Systems by Correlated Double Sampling**

As shown in Fig. 6.1 (a), the noise in a TSP is generated from many sources. For example the charger induces common-mode noise including power supply spikes [1]. Under these conditions, the signal-to-noise ratio (SNR) is compromised, causing the touch detection to fail and/or lead to “fake touch”. In order to achieve a high SNR level,



(a)



(b)

Figure 6. 1 (a) Noise sources of touchscreen systems and concept of CDS algorithm. (b) The detection threshold ( $V_T$ ) is set by the highest offset value to avoid detection errors, resulting in increased power consumption.

\*Noise (or unwanted signal) comprises stochastic (thermal or  $1/f$ ) and deterministic (clock signal, power supply spike) components.

the normal way is to boost the excitation power of the touch panel. However, this increases power consumption. Thus, reducing the noise in a TSP is critical for reduction

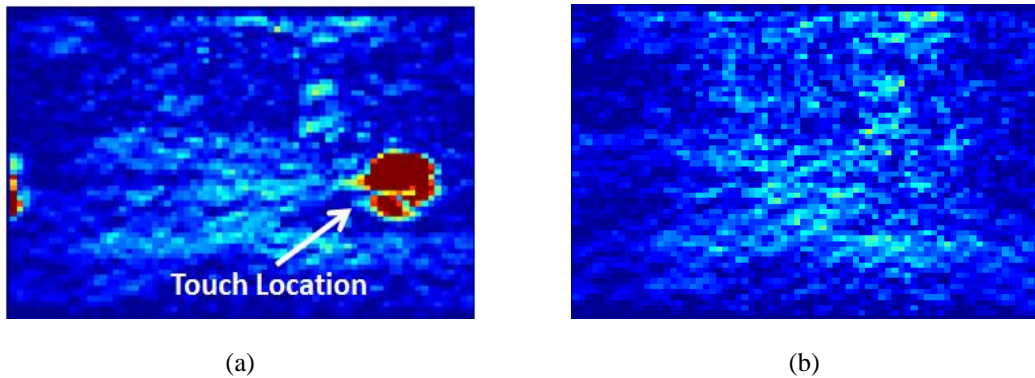
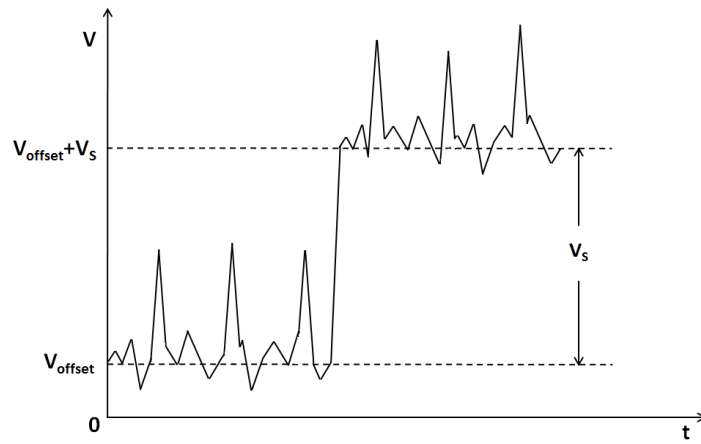


Figure 6. 2 Images of (a) single touch, (b) multi-touch, and (c) noise pattern. Red indicates high value region.

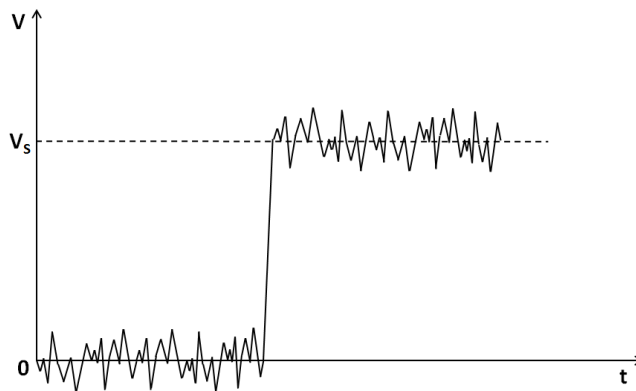
of errors and the power consumption. Furthermore, the offset on a single electrode can be canceled by deducting a fixed value. However, the non-uniformity of the offsets over the whole panel makes it difficult to cancel, giving rise to a high threshold to avoid detection errors. As illustrated in Fig. 6.1 (b), the detection threshold has to be set according to the highest offset voltage, thus requiring a high excitation power.

In this section, a technique to reduce common-mode noise and global multi-valued offset is proposed and implemented. In the proposed technique, the data associated with the whole frame after each scanning action is treated as an image [2]-[4]. Each electrode intersection constitutes a pixel and provides a capacitance value. In this way, image processing methods can be combined seamlessly with touch signal detection to remove any correlated noise and offset.

The touchscreen related images right after the single touch event is shown in Fig. 6.2. In an ideal case, only the pixels at the touch location have signal values larger than 0, and when no touch happens, the entire image pixels should be all equal to 0. However, as shown in Fig. 6.2 (b), almost all the pixels have positive values (i.e. non-blue), which indicate that the touch signal needs to be strong enough to overcome the noise. Here is where correlated double sampling (CDS) [5]-[21] can be used to cancel the global multi-valued offset and common-mode noise (or fixed pattern noise as referred to in imaging terminology).



(a)



(b)

Figure 6. 3 Conceptual outputs from an electrode of mutual capacitance TSP without and with touch. (a) Original output comprising offset and common-mode noise, and (b) the output after CDS.  $V_s$  is the signal voltage and  $V_{\text{offset}}$  is the offset voltage.

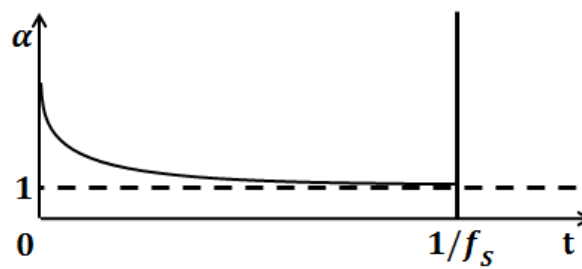


Figure 6. 4 Conceptual relationship between characterization factor  $\alpha$  and sampling interval.

### *Theoretical Analysis on CDS Based Noise Reduction Technique*

Signal-to-noise ratio (SNR) is widely used to represent a system's detection accuracy and resolution. The SNR is defined as the ratio of the signal power ( $P_s$ ) to the noise power ( $P_n$ ):

$$SNR = \frac{P_s}{P_n} ; \quad (6.1)$$

whereby  $SNR > 1$  implies that the touch signal surpasses the noise. The offset is not dealt with as a noise component, as it can be removed by deducting a fixed value. As depicted in Fig. 6.3 (a), the output from an electrode of a capacitance based TSP consists of the touch signal, the offset, and noise or unwanted signal. The offset together with common-mode noise can be canceled by CDS as shown in Fig. 6.3 (b), leaving signal and high frequency noise. After CDS, the SNR is expressed as:

$$SNR_{CDS} = \frac{P_s}{P_n'} = \frac{P_s}{P_n / \alpha} ; \quad (6.2)$$

where  $SNR_{CDS}$  represents the SNR after CDS,  $P_n'$  the noise power after CDS, and  $\alpha$  the ratio of  $P_n$  to  $P_n'$ . The range of  $\alpha$  values and corresponding implications are given in Table 6.1. In the ideal case, if two samples are obtained at the same time, the common-mode noise can be canceled completely. Thus it seems that faster sampling can provide higher SNR. However, this is not always true in practice. For example, if a single frequency waveform is considered, faster sampling doesn't imply higher SNR, as shown in the first two examples in Table 6.1. Thus, although CDS can cancel offset and reduce low-frequency common-mode noise, it may result in higher frequency noise. However this can be filtered by a low pass filter. If we assume that the sampling frequency ( $f_s$ ) is high enough compared to that of the noise (ensuring  $\alpha > 1$ ), then the conceptual relationship between the characterization factor  $\alpha$  and the sampling interval can be as depicted in Fig. 6.4.

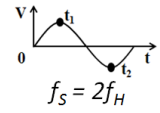
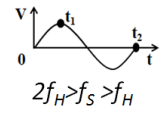
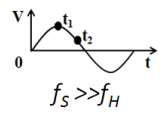
Range	SNR	Example
$0 < \alpha < 1$	SNR Degrades	 $f_S = 2f_H$
$\alpha = 1$	SNR Maintained	 $2f_H > f_S > f_H$
$1 < \alpha < +\infty$	SNR Boosted	 $f_S \gg f_H$

Table 6. 1 The ranges of characterization factor  $\alpha$  and corresponding implications.  $f_S$  and  $f_H$  are the sampling frequency and waveform frequency, respectively. In reality,  $f_H$  is the highest noise frequency within a system's noise bandwidth. If the system is a one-pole low-pass filter,  $f_H = (\pi/2)f_{3dB}$ , where  $f_{3dB}$  is system's -3dB bandwidth.

Parameter	Unit	Value
Diagonal	Inch	10.1
Aspect Ratio	None	16/9
Excitation Voltage	Volt	10
Display Pixel Size	(Micrometer) <sup>2</sup>	56×56
TX Electrode Size	Millimeter	3
RX Electrode Size	Micrometer	449
Refreshing rate	Hertz	60
Sensing Array Size	(Millimeter) <sup>2</sup>	3×3
Sensing Array Spacing	Millimeter	2

Table 6. 2 Parameters of the test bed.

### *Experimental Test Bed and Algorithm Description*

The experiments were carried out on an 80×80 touchscreen panel. Details of the test bed are given in Table 6.2. The system has an operating voltage of 10V and works with a refresh rate of 60Hz.

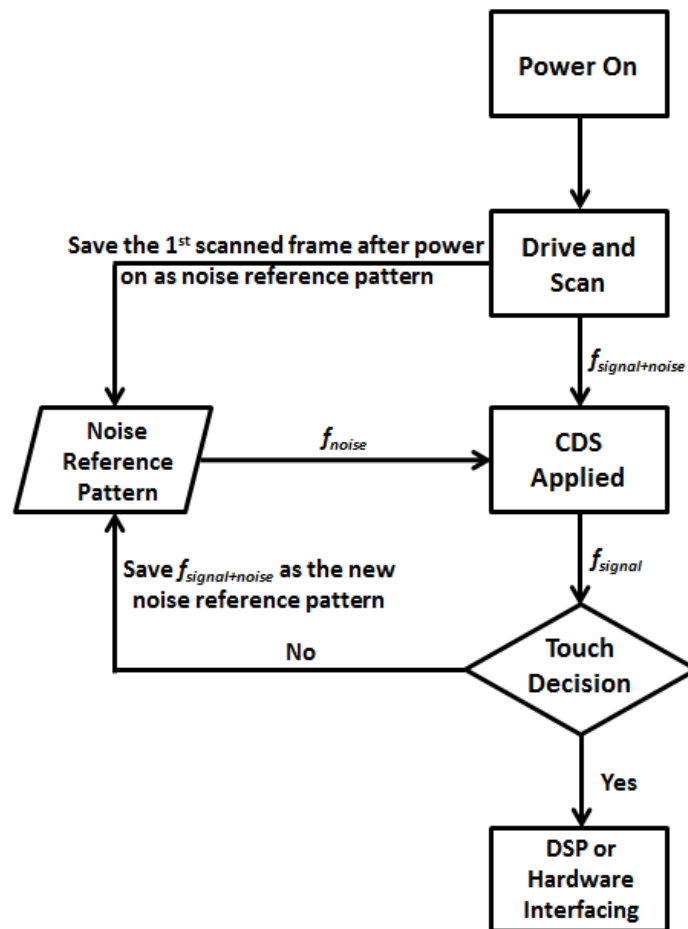


Figure 6. 5 Flowchart of the CDS based common-mode noise and global multi-valued offset reduction method.

The common-mode noise and offsets on electrodes don't change dramatically between adjacent frames. Thus, by saving the noise pattern (i.e. treating it as a noise reference frame) which is constantly updated as shown in Fig. 6.5, and deducting it from the touch signal image, the low frequency and common-mode noise and offset can be canceled. The algorithm's flowchart is shown in Fig. 6.5. After turning the device on, the drive lines are powered individually and sense lines work in sequence to measure the intersections' voltages. The first scanned frame is the noise frame (denoted as  $f_{noise}$ ), which has no touch signal but contains information of the noise and offset voltage value

on the electrode. This is saved as a reference pattern. Then the system scans the panel periodically. After each scan, the retrieved data (denoted as  $f_{signal+noise}$ ) is subject to the CDS algorithm, and a new frame (denoted as  $f_{signal}$ ) is generated. This procedure can be expressed as:

$$f_{signal}(x, y) = f_{signal+noise}(x, y) - f_{noise}(x, y) ; \quad (6.3)$$

where  $(x, y)$  represents the location of the electrode intersections. Then the frame  $f_{signal}$  is sent to the decision function to decide if a touch has happened or not. If the frame  $f_{signal}$  is interpreted as a touch event, the data will be used for further processing depending on the hardware/software environment. For example, the touch signal can be used to open a folder on desktop or close a webpage. If not, the frame  $f_{signal+noise}$  (prior to applying the CDS algorithm) will be saved as the new or replacement noise reference pattern. In this way, the noise reference pattern can be updated automatically with the most recent noise information.

### *Results and Discussion*

As explained above, CDS can efficiently cancel the global multi-valued offset as well as reduce the low-frequency common-mode noise. In the experiments, two separate sets of data from sampling frequencies of 30Hz and 60Hz are used. Examples of applying CDS to single and multi-touch related touch images are illustrated in Fig. 6.6. The normalized output (no touch event) PSD plots are used to analyze the effect of CDS. Based on Fig. 6.6, before CDS a strong DC component is observed due to the offset. In Fig. 6.6 (a), we observe that when below 8Hz, after applying CDS with the 60Hz sampling frequency, the noise power drops. But between 9Hz to 17Hz, the noise power is of a similar level as without CDS. Above 18Hz, the noise power increases. When the sampling frequency is down to 30Hz, only below 3Hz does the noise power drop after CDS. This is because the correlation of low-frequency noise between adjacent frames is relatively weak at low sampling frequencies. This correlation increases at higher

sampling frequencies at the expense of energy consumption. Since the offsets behave as DC, they can be canceled regardless of sampling frequency.

As mentioned earlier in Section 6.2.2, CDS introduces higher frequency noise within a certain bandwidth. This is related to the sampling frequency and explained by the example below. Consider a noise component with frequency  $f_s/2$ , which is subject to CDS of frequency  $f_s$ . The distance between the two adjacent sampling points is  $\pi$ . Thus after CDS, the output  $y$  is expressed as

$$y = A \sin(2\pi \frac{f_s}{2} t + \varphi + \pi) - A \sin(2\pi \frac{f_s}{2} t + \varphi) = -2A \sin(\pi f_s t + \varphi) ; \quad (6.4)$$

where  $A$  and  $\varphi$  are the amplitude and the initial phase of the waveform, respectively,  $t$  is the time to sample the waveform. This indicates that the absolute output is doubled after CDS. Similar analysis can be made for other sampling frequencies.

As the touch signal has a low frequency property, the increased high frequency noise power can be filtered. Within 10% of  $f_s$ , SNR is boosted by 5.9dB and 7.6dB when sampling frequencies are 30Hz and 60Hz, respectively. Beyond this frequency, the SNR starts degrading. Thus CDS is powerful in reducing common-mode noise, and is expected to further enhance the SNR in the TSPs.

#### *Algorithm Robustness*

The assignment of the most recent frame that does not generate a touch event to be the noise reference pattern might raise concerns that an unexpected ‘bad frame’ resulting from a temporary hardware malfunction might result in a deterioration of SNR in subsequent frames. This can be addressed by applying exponential smoothing:

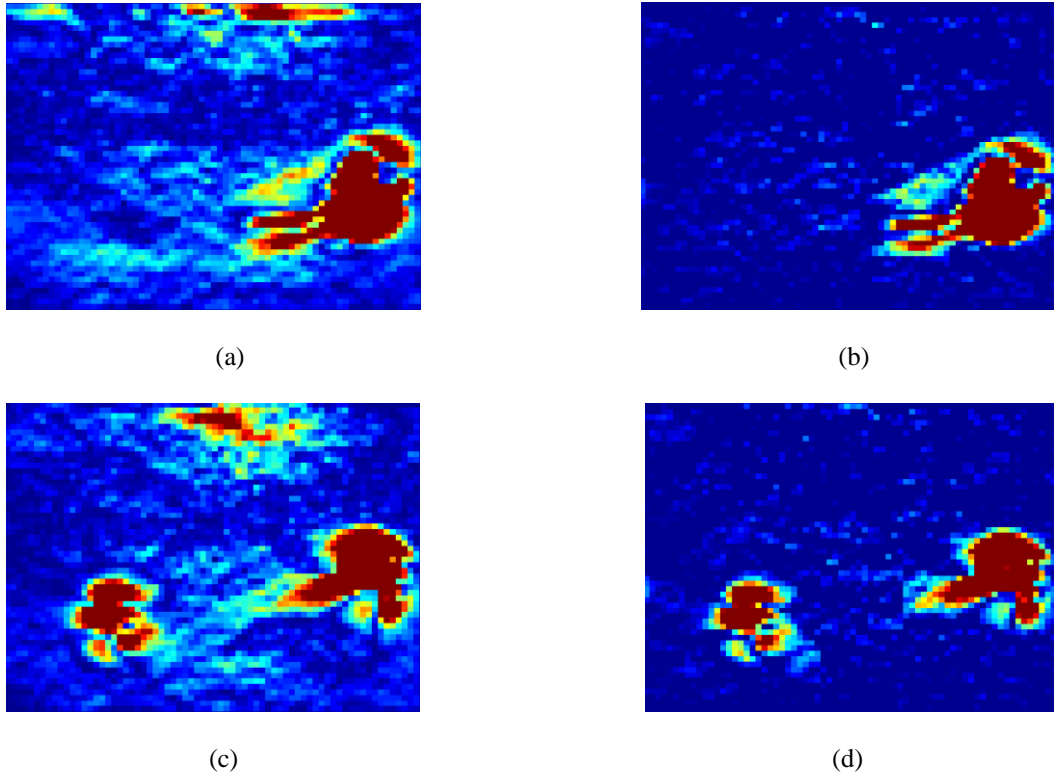


Figure 6. 6 The touch related images before and after CDS. (a) and (c) are raw images based on one and two touch events. (b) and (d) are the CDS processed images

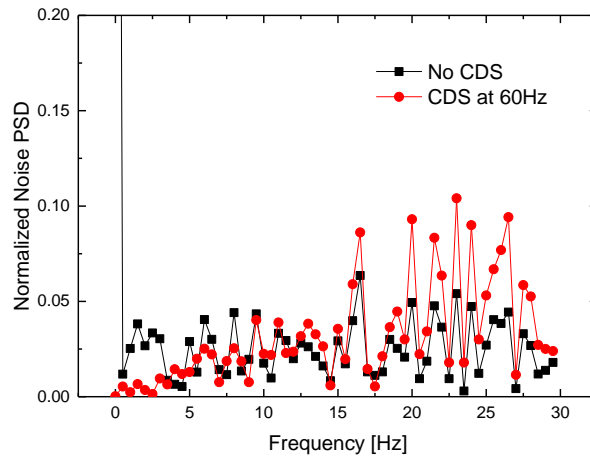
$$f_{noise}^{(n+1)}(x, y) = \alpha f_{noise}^{(n)}(x, y) + (1 - \alpha) f_{signal+noise}^{(n)}(x, y) ; \quad (6.5)$$

The weighting factor  $\alpha$  can be adjusted to optimize the system's performance. However, it should be noticed that this will slightly weaken the correlation between adjacent frames.

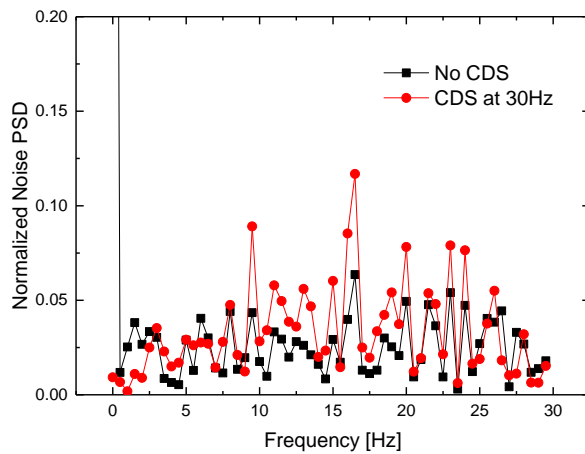
#### *Algorithm Time Budget*

Although CDS provides significant reduction of the common-mode noise and offset, the computational time and energy consumption of the algorithm are key considerations. As with many mainstream touchscreen systems [1], the system's scan rate is 60Hz, which implies that the computational time should not be longer than 16.7ms. The

computational time depends on the algorithm's complexity, which is  $O(N)$  in this work.



(a)



(b)

Figure 6. 7 Normalized PSD plots of the original output and CDS outputs with sampling frequency at (a) 60Hz and (b) 30Hz.

Here  $N$  is the number of pixels to be processed. In the case considered here,  $N$  equals 6400. The processors in many of the current PDAs have a computational ability in the

range of GHz. For example, a 1GHz processor would take  $\sim 6.4\mu\text{s}$  for the CDS algorithm, which is a much smaller time period compared to the system's refresh interval.

#### *Algorithm Energy Budget*

Current touchscreen controllers scan at 75kHz with a power consumption of 2.5mW [22]. The energy  $E$  for measuring each electrode intersection is

$$E = P / f_s ; \quad (6.6)$$

where  $P$  and  $f_s$  denote controller's power consumption and scan frequency, respectively. Thus,  $1/30 \mu\text{J}$  is needed for reading each electrode intersection. For a sensing matrix with  $M$  rows and  $N$  columns, the total power ( $P_{total}$ ) for scanning the whole panel can be expressed as

$$P_{total} = (EMN)f_s ; \quad (6.7)$$

Current commercial TSPs in mobile phones use 9 column electrodes and 16 row electrodes, which yield 144 electrode intersections. Thus the power consumption for measuring the whole panel once is 0.288mW (assuming a scan rate at 60Hz), and the energy consumption for scanning each frame is  $4.8\mu\text{J}$ .

Current embedded processors have a power efficiency ( $\eta$ ) of over 20MIPS/mW [23]. Thus the power consumption  $E_{CDS}$  for the algorithm

$$E_{CDS} = N / \eta ; \quad (6.8)$$

is roughly 7.2nW, and the computation time is  $0.14\mu\text{s}$ . Therefore the energy consumption is around 1fJ, which is much smaller than that of the touchscreen controller, and can thus be considered negligible.

## **6.2 Reduction of Noise Spikes in Touch Screen Systems by Spatial Low-pass Filtering**

In a previous section, the global multi-valued offset is removed along with the common-mode noise by the CDS based technique. However, when the correlation between the touch frames and the noise reference frame becomes weak, noise spikes still remain, giving rise to detection errors. By analyzing the characteristics of the touch signal and noise spikes, we learn that the touch signal is normally of a low spatial frequency compared to the surrounding noise spikes [24]-[43]. Therefore spatial low-pass spatial filters can be used for the reduction of noise spikes. As depicted in Fig. 6.8, the noise spike is averaged by adjacent pixel values. However, the touch signal is reduced by the low pass spatial filtering as well, called the smoothing effect, which may decrease the signal-to-noise ratio, depending on the bandwidth and the mask size of the spatial filter. The induced smoothing effect may also result in signal distortion in terms of touch presence and position, leading to detection errors, and thus requires further research.

In this section, we investigate the induced smoothing effect on touch detection. In particular, we analyze the following aspects: SNR, signal distortion (in terms of the change of touch position and the attenuation) and noise spike attenuation. The optimization of the above parameters can be achieved by tuning the mask size and bandwidth of the spatial filter. Based on the analysis, we present an adaptive bandwidth tuning algorithm for the dynamic optimization of spatial filter when the signal and noise conditions are changed. In the algorithm, we evaluate the attenuation of the signal and noise spike, and select a suitable bandwidth to maintain the desired performance. Below we start from a brief introduction of low pass spatial filtering techniques and its impact on noise reduction, and then followed by theoretical analysis, experimental results and corresponding discussion.

*Low-pass Spatial Filters and Corresponding Effect on Noise Reduction*

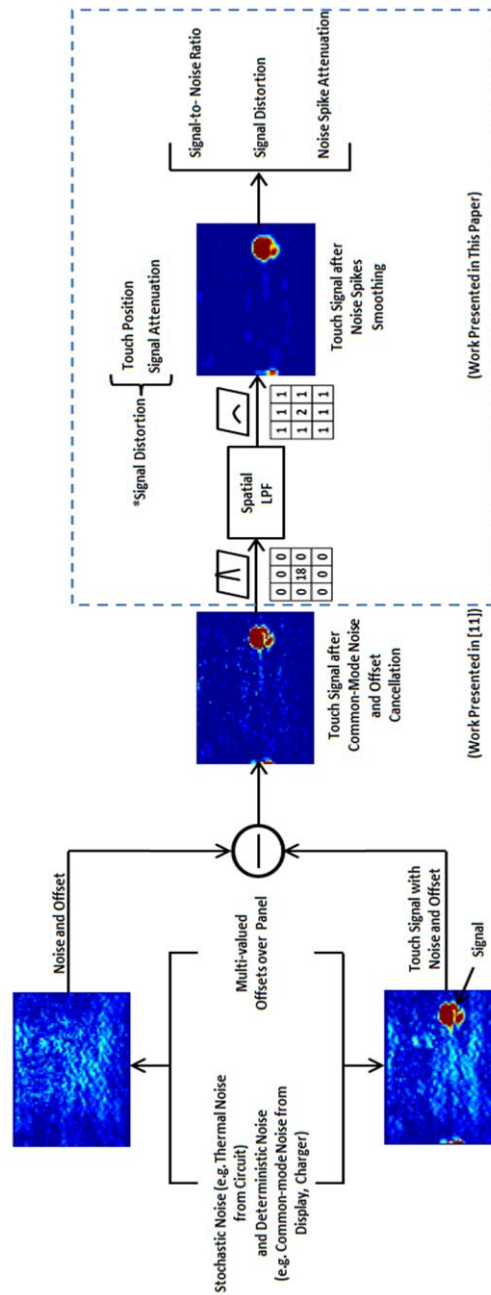


Figure 6. 8 Noise in touch screen systems; the CDS based technique for common-mode noise and global multi-valued offset cancellation; noise spikes attenuation by a spatial LPF and the corresponding smoothing effect.

Spatial LPFs are divided into two categories: linear (e.g. average filter) and non-linear types (e.g. median filter) [44]-[48]. A mask/kernel with size  $m \times n$  ( $m$  and  $n$  are normally odd positive integers to ensure that there is only one pixel in the center of the mask) is employed in the spatial filter, using the same or different coefficients to control the bandwidth. Each pixel in the original image is computed along with its neighboring pixels, and the outcome is produced in a new image at the same position.

Both linear and non-linear structures offer benefits and drawbacks to noise spikes reduction for different types of touch based interactivities (e.g. finger touch). For example, good noise spike attenuation is offered by non-linear LPFs, which unfortunately may remove a stylus touch completely and cannot effectively remove the noise on the electrode. Thus, linear filters (average and Gaussian filter) are employed and analyzed in this paper. An example of an average filter is described in Fig. 6.9, whose mask size is  $3 \times 3$  and the coefficients equal to 1. Each pixel is added to the surrounding 8 pixels. The sum is then divided by the scaling constant 9 to generate a new pixel value.

In practice, this algorithm can be implemented by constructing an intermediate image in which each pixel contains the sum of 3 pixels in the x-direction. The final filtered image is obtained by performing the same process in the y-direction on the intermediate image, and then dividing by the scaling constant 9. This process is equally valid for Gaussian-weighted filters. This is especially useful for higher resolution devices, which would require larger masks than  $3 \times 3$ , as this implementation scales linearly with mask size rather than quadratically. The presented algorithm in this section focuses on smoothing noise spikes to boost SNR while maintaining a desired signal strength level in order to avoid detection errors.

### *Theoretical Analysis on Smoothing Effect on Touch Signal*

#### *Mask Size and Touch Position*

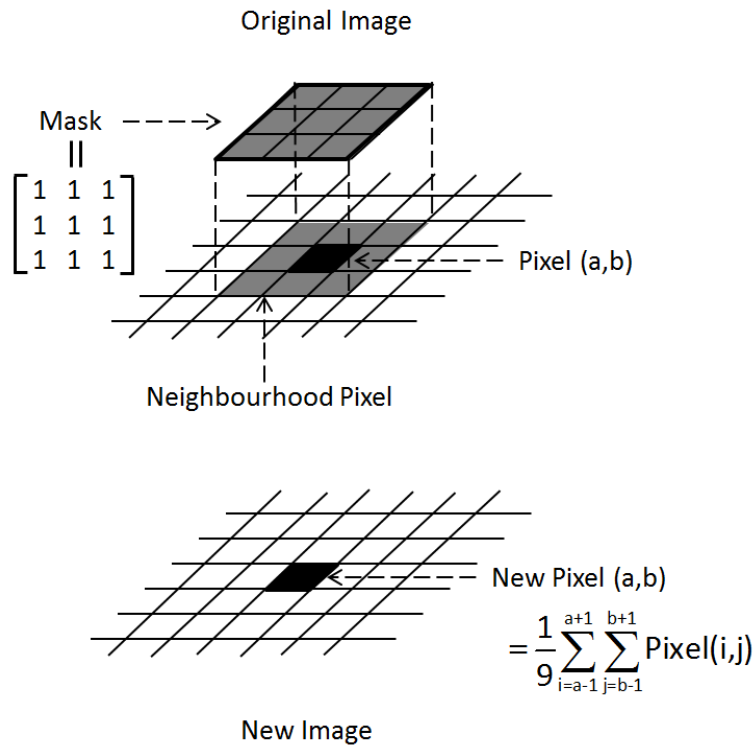


Figure 6. 9 Algorithm description of a spatially based average low-pass filter.

To avoid mis-registration at a wrong position and the interference from other touches, the mask size of the average filter is determined to be  $3 \times 3$ . This is because the touch event is limited in a certain region (e.g.  $3 \times 3$  electrodes for a finger touch). If a large mask size is used, noise in the non-touch area weakens the strength of the touch signal, resulting in a high probability of touch mis-registration. Below we mathematically analyze the relationship between the mask sizes and touch position registration. Fig. 6.10 shows that a perpendicular finger touch occurring in the red region only affects the adjacent 8 pixels (yellow and green regions). A represents the value at the touch point,  $B_1$  to  $B_4$  and  $C_1$  to  $C_4$  are the adjacent region values, and  $N_1$  to  $N_{40}$  indicate the surrounding noise values. When a  $3 \times 3$  average filter is applied, the output at the same position in the new image is:

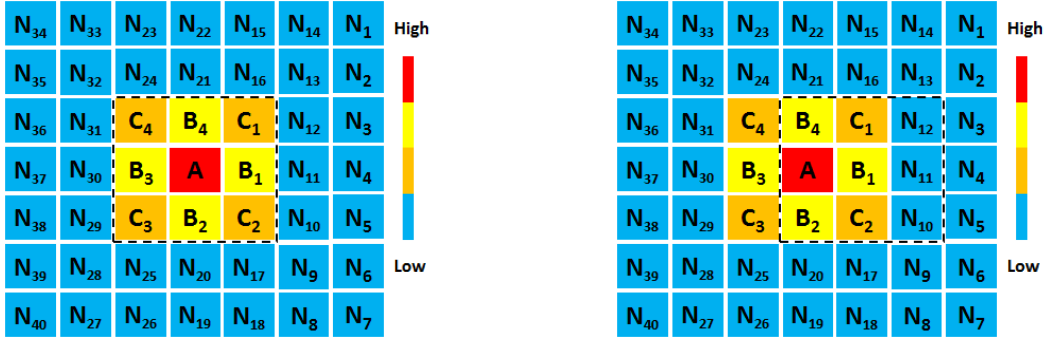


Figure 6. 10 Conceptual top-view of a finger touch on a mutual row-and-column capacitance TSP.  $A$ ,  $B_1$  to  $B_4$ ,  $C_1$ , to  $C_4$  and  $N_1$  to  $N_{40}$  indicate the values over the electrodes intersections. The average spatial filter is applied to the touch position pixel  $A$  (left) and the adjacent pixel  $B_1$  (right).

$$A' = (A + B_1 + B_2 + B_3 + B_4 + C_1 + C_2 + C_3 + C_4) / 9; \quad (6.9)$$

If we assume that pixels at equal distance from the touch point have similar values, then Eq. 6.9 is simplified as:

$$A' = (A + 4B_1 + 4C_1) / 9; \quad (6.10)$$

$B_1$  and  $C_1$  can be represented by  $A$  with scaling down factors ( $b$  and  $c$ ), expressed as:

$$B_1 = A / b, C_1 = A / c, (b > 1, c > 1); \quad (6.11)$$

thus  $A'$  is:

$$A' = (A + 4A / b + 4A / c) / 9 = A(bc + 4b + 4c) / 9bc; \quad (6.12)$$

If the registered touch position in the new image is shifted, this most likely happens within the yellow regions which are geographically closest to the red. The yellow region with value  $B_1$  is analyzed to explain when the mis-registration in terms of position takes place. The filtered value  $B_1'$  is expressed as:

$$\begin{aligned}
B_1' &= (A + B_1 + B_2 + B_4 + C_1 + C_2 + N_{10} + N_{11} + N_{12}) / 9 \\
&\approx (A + 3B_1 + 2C_1 + 3N_{11}) / 9 = (A(bc + 3c + 2b) + 3bcN_{11}) / 9bc;
\end{aligned} \tag{6.13}$$

To ensure that  $A' > B_1'$ , the following condition must be satisfied:

$$\frac{A}{N_{11}} > \frac{3bc}{2b + c}; \tag{6.14}$$

Normally  $N_{11}$  is about 2 orders smaller than  $A$ ; and  $b$  and  $c$  lie between 1 to 3. Hence, the condition expressed in Eq. 6.14 is satisfied. When the mask size increases to  $5 \times 5$ , the condition of  $A' > B_1'$  is completely determined by the surrounding noise values, resulting in a high probability of mis-registration.

#### *Spatial Frequency Properties of Signal and Noise Spikes*

The touch signal is normally at a low spatial frequency compared to the noise spikes. This is the fundamental assumption of the low pass spatial filtering technique. However, in some cases the touch signal can offer high spatial frequency as well. For example, only one electrode may be affected when a stylus touch is applied. In contrast, when a noise spike happens within the touch region, it may have low spatial frequency property. The low pass spatial filtering cannot remove noise spikes and may result in the decrement of SNR when the spatial frequencies of touch signal and noise spikes are very close or overlapped. A possible solution of this is the use of time domain low pass filtering at a pixel level.

In this section, finger touch is used and analyzed, as this is the most preferred touch activity for PDAs. Finger touch is of low spatial frequency, and the bandwidth relies on the contact area, which is highly individual dependent. Even for the same user, the touch property can be changed when different applications are used. Hence, the filter bandwidth should be dynamically adjusted to keep the desired touch information while maximally reducing noise spikes.

### *Algorithm Description*

To reduce the noise spikes in the frame after CDS, a spatial LPF with an initial bandwidth is used. Since the touch and noise properties are dynamically changed, the bandwidth of the spatial LPF is required to be adjusted in order to optimize the performance. As described in Fig. 6.11, the frame after CDS (denoted as  $f_{CDS}$ ) is sent to the spatial LPF for the noise spikes reduction. Then the filtered frame (denoted as  $f_{LPF}$ ) enters into the touch decision function to determine if a touch happens or not. If a touch is registered, then the frame (denoted as  $f_{Touch}$ ) is evaluated in terms of the signal and noise spike attenuation by the bandwidth decision function, to analyze if the bandwidth of the spatial LPF needs to be changed. If no touch is registered, the scanned frame ( $f_{scan}$ ) is updated as a new reference noise pattern, which will be used by CDS algorithm, as shown in Fig. 6.11.

### *Results and Discussion*

To evaluate the smoothing effect, three factors are considered here: SNR, signal and noise attenuation. The normalized output (no touch event) PSD plots (Fig. 6.12) are used to analyze the noise behavior after the average LPF. It can be observed that the high frequency noise generated by the CDS is suppressed. The SNR is boosted by 15.6dB. The signal and noise spike are attenuated by 4.51dB and 19.25dB respectively. The attenuation of the signal strength is undesirable, thus different coefficients are used for the bandwidth adjustment to retain more signal information. The coefficients of the filter mask follow Gaussian distribution with different standard deviations ( $\sigma$ ), representing various bandwidths of the LPF. Four Gaussian distribution based filter masks are illustrated in Fig. 6.13. Here small standard deviation indicates that more information about the pixel itself is maintained. In contrast, large standard deviation implies that the pixel is strongly affected by the adjacent neighborhoods. The simulation results of applying spatial filter with different bandwidths are illustrated in Fig. 6.14. Due to the spatial high frequency property, noise spike suffers severer attenuation compared to the touch signal. From Fig. 6.14 (a), the signal and noise spike are

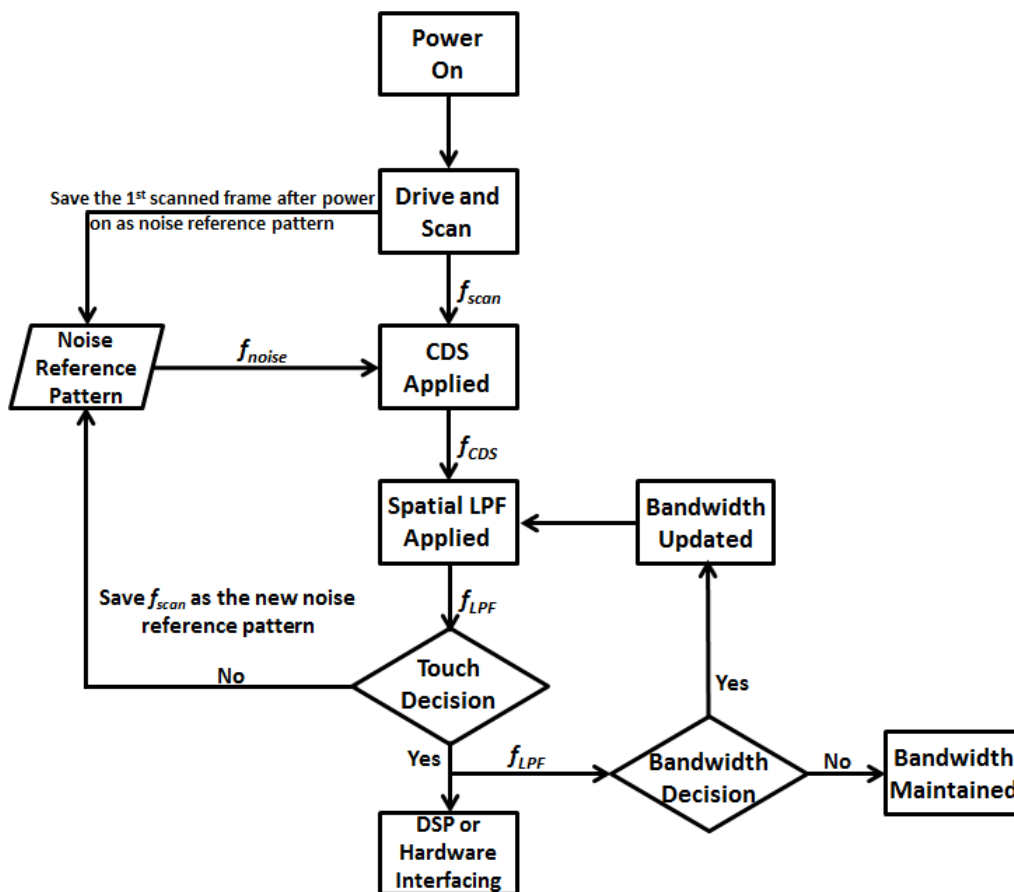


Figure 6. 11 Flowchart of the CDS and spatial LPF based noise reduction algorithm.

attenuated dramatically when  $\sigma$  is within the range of 0.5 to 1. After  $\sigma > 1.5$ , the trends of attenuation are reaching saturation. Thus the range of  $0.5 < \sigma < 1$  is further investigated, and the results are illustrated in Fig. 6.14 (b). By evaluating the signal and noise spike attenuation dynamically, the filter bandwidth is updated. For example, if the accepted signal attenuation is 2dB, then the initial Gaussian distribution based mask with standard deviation at 0.6 would be used to maximally attenuate the noise spike. Later, when the signal attenuation is found to be 1dB, then a bigger standard deviation can be selected to further smooth noise spikes and boost SNR.

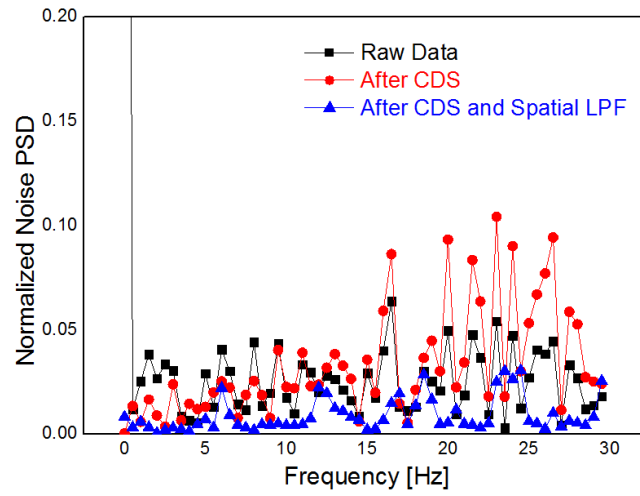


Figure 6. 12 Normalized PSD plots of the original output, CDS output with sampling frequency at 60Hz and spatial average LPF output with mask size of 3×3.

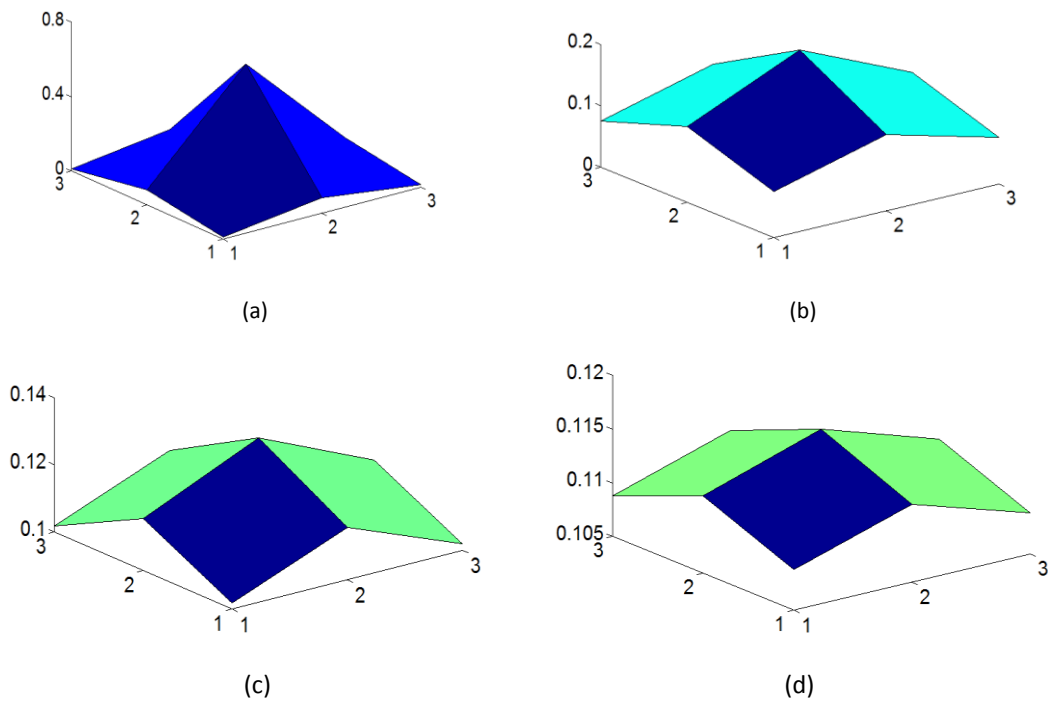


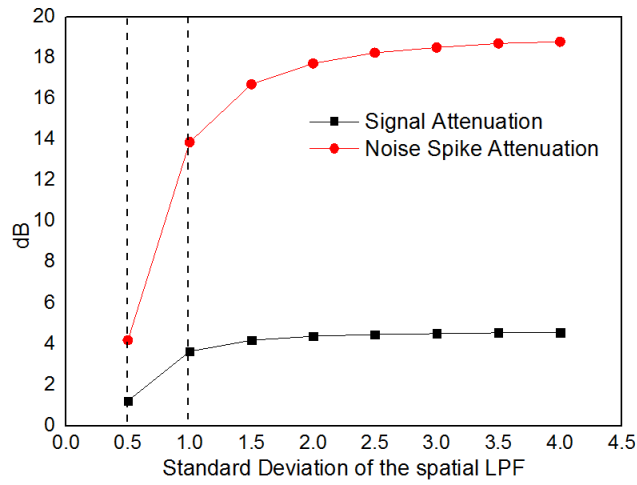
Figure 6. 13 Four Gaussian distribution based masks with different bandwidths (represented by standard deviations). (a)  $\sigma = 0.5$ ; (b)  $\sigma = 1$ ; (c)  $\sigma = 2$ ; (d)  $\sigma = 4$ .

It is also important to investigate the computational time and energy consumption of the presented algorithm. Our system's scanning rate is 60Hz, thus the computational time of the algorithm should be much lower than 16.7ms. The required computational time depends on the complexity of the algorithm and the performance of the processor. The complexity of the spatially based algorithms used in this research is around  $O(3N)$ , where  $N$  is equal to 6400. Current commercial processors in mobile phones can operate in the range of GHz. Hence, a computational time of approximately 19.2 $\mu$ s is required when a 1GHz processor is equipped. As stated before, commercial processors can work at 20MIPS/mW, therefore the power consumption of the algorithm is 21.6nW which is negligible compared to that of scanning the whole panel.

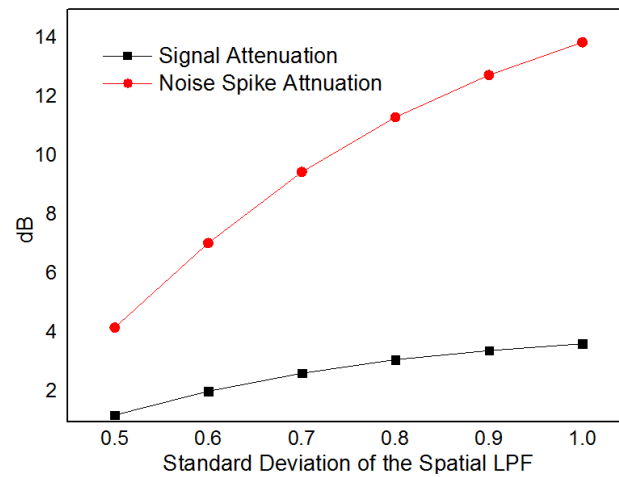
The noise spikes in TSPs give rise to "fake" touch, resulting in the high power consumption. In section, we present a low pass spatial filtering based technique for the noise spike reduction. By the approach of evaluating the spatial LPF induced smoothing effect, the filter bandwidth is dynamically adjusted to optimize the performance. Based on the experiment, a SNR enhancement of 15.6dB and a noise spike attenuation of 19.25dB are obtained. The filtered signal improves detection accuracy, thus less energy is required to maintain a desired performance.

### **6.3 Down-sampling Techniques for Capacitive Touch Panels**

In the previous section, touch event related frames are processed as images, and the noise is eliminated by correlated double sampling and spatial low-pass filtering related techniques. In this section, by employing the sparse, low spatial frequency and distribution property of touch signals, compressive sensing [49]-[55] and averaging based down-sampling techniques are presented to reduce power consumption while maintaining detection accuracy. Furthermore, as the number of scanned touch sensors is reduced, the touch panel's readout speed is also boosted. As illustrated in Fig. 6.15, instead of scanning all the sensors, only a portion of them are selected with a random or



(a)



(b)

Figure 6. 14 Results of signal and noise spike attenuation by applying spatial LPFs with different standard deviations. (b) is the dashed part of (a).

fixed pattern. A compressive sensing or other reconstruction algorithm is then applied to the down-sampled signal, depending on the down-sampling pattern. However, after interpretation of the signal, the detected touch position may differ from the original one, thus requiring a suitable regional scan around the reconstructed touch position to

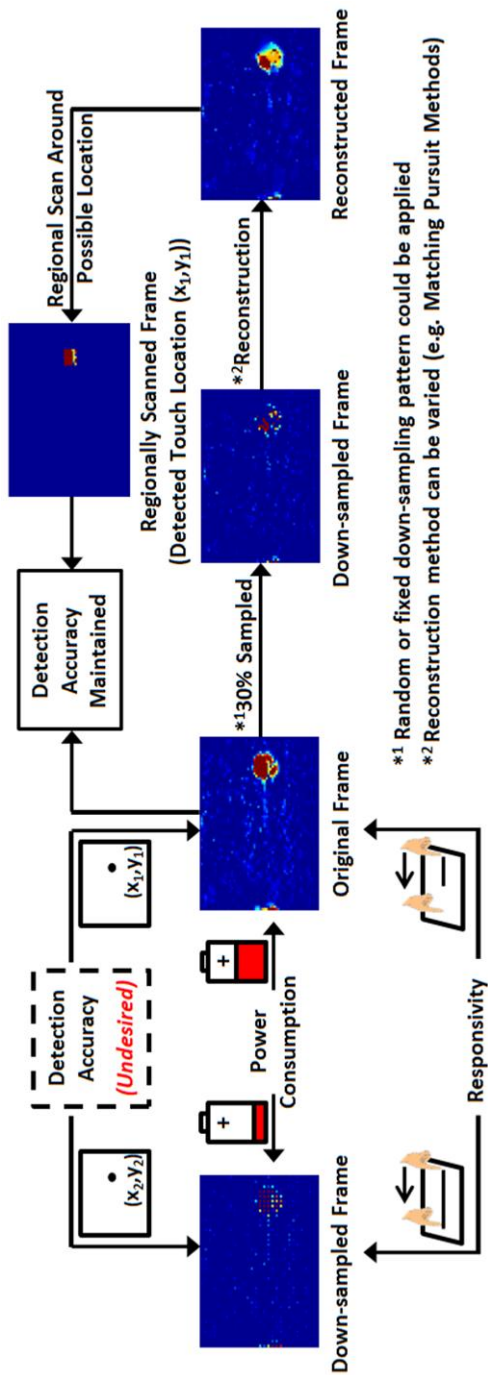


Figure 6. 15 Merits and drawbacks of the down-sampled signal, and compressive sensing based fast readout technique.

retrieve accurate touch information. The regional scan range is determined by the reconstruction quality, which mainly depends on the percentage of the sampled sensors and the touch signal property. Through this method fewer sensors are scanned, therefore the readout speed is boosted and power consumption lowered.

*Algorithm Description*

Instead of scanning all electrode pads or intersections, only a small portion (e.g. 25%) were selected and measured, and then the collected data was processed by the reconstruction algorithms to recover the touch event related image. However, the touch location of the reconstructed signal may differ from the original one. The shifted distance mainly depends on both the percentage of the electrode pads sensed by the processor and the reconstruction algorithm. Pixel is defined as the unit of distance as shown in Fig. 6.16 (a). Thus, considering the changed distance, a regional scan within a certain range is performed to acquire the accurate touch location and relevant information. For example, if the changed distance is  $d$ , then the regional scan range will be a square centered at the reconstructed touch position, with a side length of  $2d$ . This is illustrated in Fig. 6.16 (b). In this case, the side length is 2, and the square covers 9

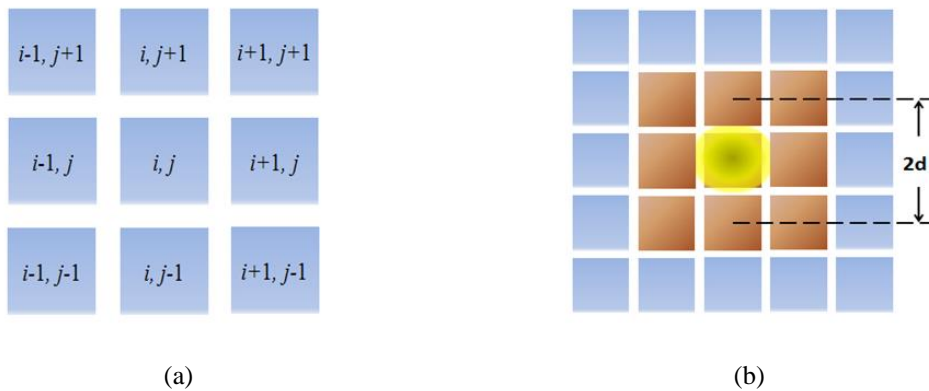


Figure 6. 16 (a) The distance from one pixel  $(i,j)$  to other pixels (e.g.  $(i+1, j+1)$  )can be expressed by Euclidean distance. The unit of the distance is pixel. (b) Regional scan method for the multi-pad capacitance TSP. Red pads will be scanned rapidly after the reconstruction. The yellow point is the reconstructed touch position.

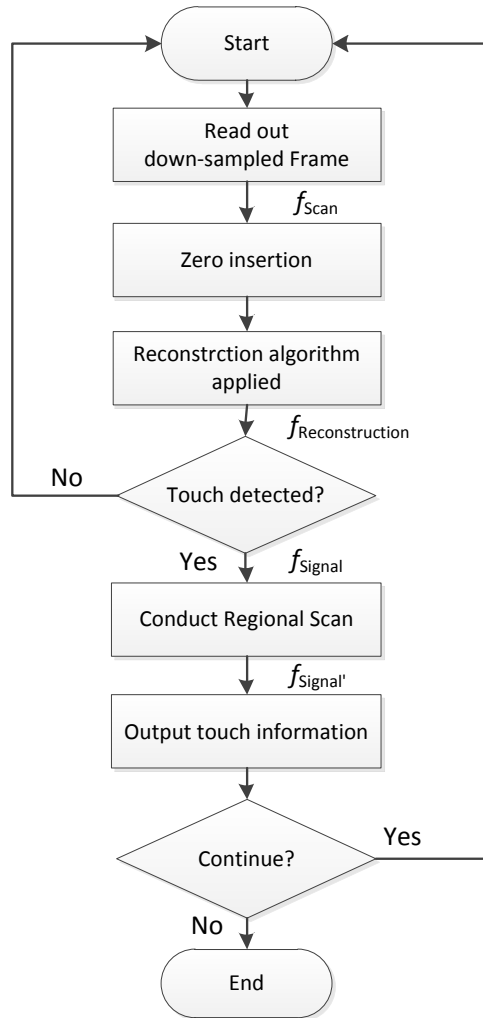


Figure 6. 17 Flowchart of the down-sampling based fast readout technique.

electrode pads, which indicates that these 9 electrode pads will be scanned after the reconstruction to obtain accurate touch information.

The flowchart of the algorithm is described in Fig. 6.17. After selecting a portion of sensors, the scanned frame ( $f_{scan}$ ) is applied with reconstruction method (e.g. averaging), yielding the frame  $f_{reconstruction}$ . The reconstructed frame is then sent into the touch decision function to determine if a touch happens or not. On a positive determination, a

regional scan is performed to obtain the accurate touch location and relevant touch information.

Below the results and discussions are divided into two sections, according to the type of the down-sampling pattern.

#### *Results and Discussion of Random Pattern Down-sampling*

Three sets of simulations are investigated by randomly collecting 10%, 30%, and 50% of the original electrode pads. The Monte Carlo method is applied to have the random distribution for the sampled touch electrodes. Each set had 1000 simulations. Three reconstruction results are depicted in Fig. 6.18 as examples. As expected, the least sampled data offered the highest probability of poor reconstruction result. The reconstructed touch positions followed a Gaussian distribution, and the distribution of the 10% sampled set is shown in Fig. 6.19 (a). Taking the cross-section of the direction with the largest variance (Fig. 6.19 (b)), we analyze the probability of the changed distance modeled as:

$$f(d) = 101.4 \exp(-((d) / 2)^2); \quad (6.15)$$

Here  $d$  is the distance between the reconstructed touch position and the original touch position. We assume that the reconstructed results out of  $[\mu-3\sigma, \mu+3\sigma]$  ( $\mu$  and  $\sigma$  are the mean and variance of the Gaussian distribution) [42] rarely happens, thus the maximum changed distance is 5 pixels. Under the same analysis, the maximum changed distances of 30% and 50% sampled data sets in our simulations were 4 and 3 pixels, respectively. To ensure the regional scan range can cover the original touch location, the scan side length is determined to be twice the maximum changed distance. The number of actual covered sensors within the square is expressed as:

$$N_{\text{Regional-scan}} = (2d + 1)^2; \quad (6.16)$$

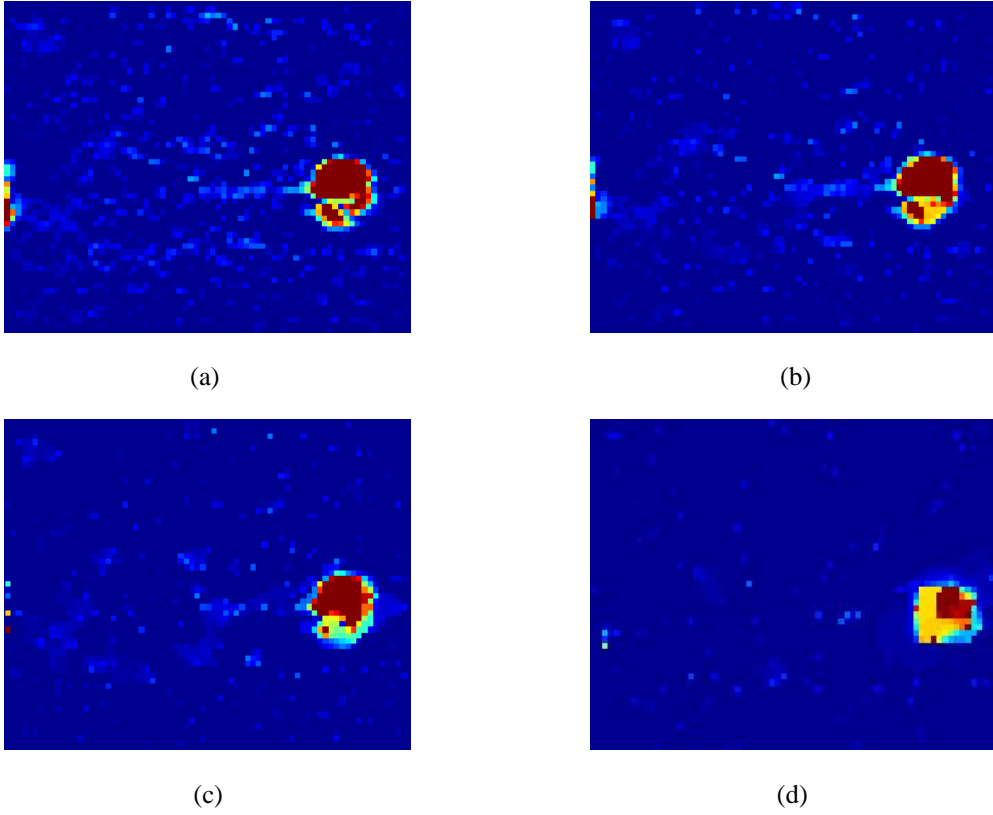
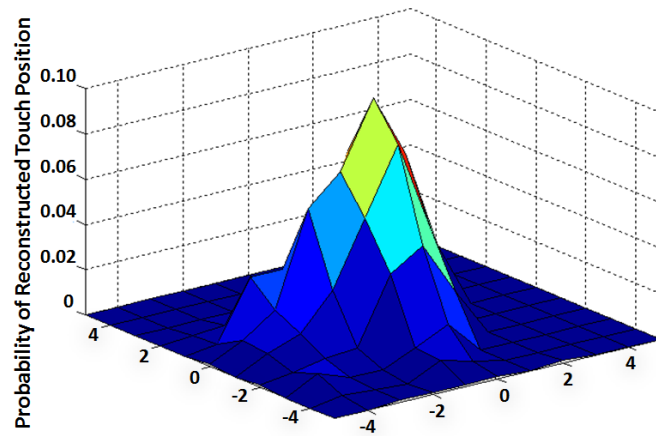


Figure 6. 18 (a) Original signal; (b), (c) and (d) are reconstructed signals with 50%, 30% and 10% of original electrode pads.

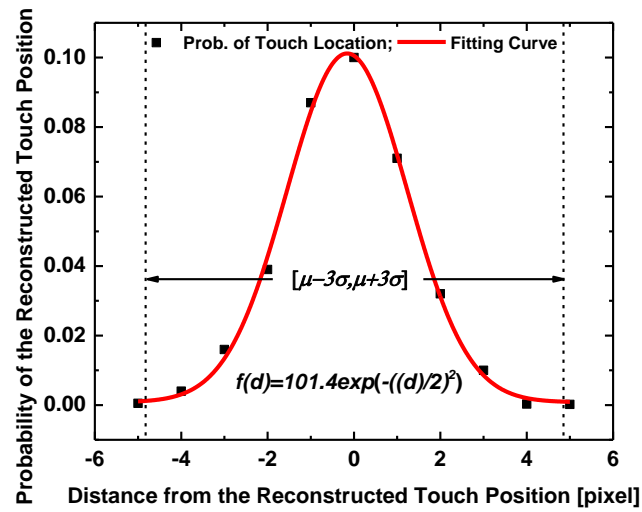
where  $N_{Regional-scan}$  is the number of measured sensors at the regional scan stage. Increasing the percentage of the sensed sensors gives rise to a higher probability of maintaining the touch location.

For example, taking 10% sampled data to acquire the accurate single touch position, only 121 electrode pads centered at the peak touch value location are required to be regionally scanned. The number of totally measured sensors is 761. In contrast, 6400 sensors are needed to be read using the traditional method. When multi-touch occurs, the number of measured sensors is expressed as:

$$N_{Total} = N_{Down-sampled} + M_{Touch} \times N_{Regional-scan} ; \quad (6.17)$$



(a)



(b)

Figure 6. 19 (a) Distribution of the reconstructed touch positions; X-Y coordinates indicate the distance between the reconstructed touch position and original touch position. (b) The cross-section with the largest variance of (a).

TABLE II  
MULTI-PAD TSP

$P_{Down-sampled}$	$N_{Down-sampled}$	$N_{Regional-scan}$
10%	640	121
30%	1920	81
50%	3200	49

Table 6. 3 Relationship between sampling percentage and regional scan range.

$$N_{Down-sampled} = P_{Down-sampled} \times N_{Sensor} ; \quad (6.18)$$

where  $N_{Total}$  denotes the total number of measured sensors and  $N_{Down-sampled}$  is the number of randomly selected sensors.  $P_{Down-sampled}$  and  $N_{sensor}$  are the percentage of sampled sensors and total number of sensors in a touch panel, respectively, and  $M_{Touch}$  is the number of touch events. The relationship between  $P_{Down-sampled}$ ,  $N_{Regional-scan}$  and  $N_{Down-sampled}$  in this work is illustrated in Table II.

It is observed that the presented algorithm is more suited to large-scale touch panels. For example, for a small-scale touch panel there are 320 (20×16) touch sensors and 50% sensors are randomly selected, if greater than 4 touch events happen  $N_{Total}$  may be bigger than  $N_{Sensor}$ .

#### *Results and Discussion of Fixed Pattern Down-sampling*

In this section, the spatial low-frequency property of capacitive touch signals is used for fixed pattern down-sampling and reconstruction. Below in this section, the algorithm proposed and implemented based on this property are explained, following with the discussion on experimental and simulation results. By analyzing the characteristic of the frame after zero-insertion ( $f_{zero-insertion}$ ), the filter size for averaging purpose has to be  $(2n+3) \times (2n+3)$ , where  $n$  is a positive odd integer. In this section, a 5×5 average filter is employed.

A swipe touch frame is illustrated in Fig. 6.20 with the corresponding reconstructed frames using a low-pass spatial filter as an example, based on which it can be observed that the touch event's spatial low frequency property is reconstructed. After applying the spatial low-pass filter, an additional benefit is the boost in ratio between the touch signal to the peak noise spike, which in our experiments is 5.4 dB on average. The regional scan range is determined by the reconstruction quality, which is related to the touch signal properties (shape and position) and the size of spatial LPF. In the above, the determined filter size to reconstruct the touch signal and smooth the noise spikes is  $5 \times 5$ , based on which the distribution of the estimated touch positions is shown in Fig. 6.21. It can be observed that the distribution shape follows a Gaussian (Fig. 6.21 (a)) distribution. Taking the cross-section of the direction with the largest variance (Fig. 6.21 (b)), we analyze the probability of the changed distance, which can be modeled as

$$f(d) = 6.87 \exp(-((d + 0.6)/1.07)^2); \quad (6.19)$$

where  $d$  is the distance between the reconstructed touch position and the original touch position. Aligned to the assumption made above, the maximum changed distance is 2. From Eq. 6.16, it can be shown that to acquire the accurate single touch position, only 25 electrode pads centered at the peak touch value location are required to be regionally scanned. The number of totally measured sensors is 1625. In contrast, 6400 sensors need to be read previously. The analysis of the number of measured sensors for multi-touch events is the same as discussed in random pattern down-sampling section.

#### *Algorithm Time and Energy Budget*

If the minimum  $l_1$  norm reconstruction algorithm is employed, the computation complexity is  $O(N \log_2 N)$  [53], which indicates that approximately 80K multiplications are needed to reconstruct the signal. For a GHz range processor, the calculation time is about 80  $\mu$ s. Compared to the duration of a touch event, which is assumed to be 0.1 s, and the scanning interval (17 ms), the calculation time is negligible. As mentioned

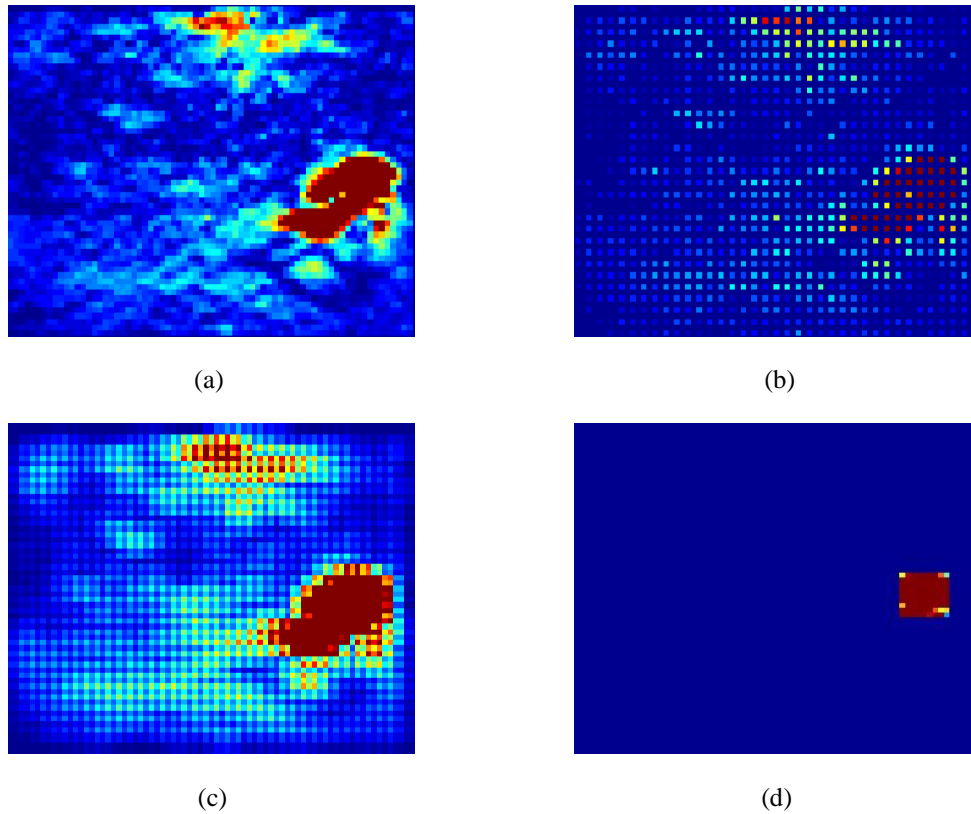
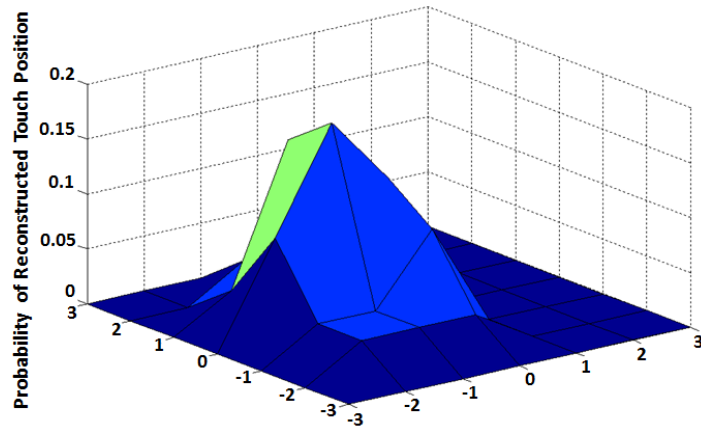


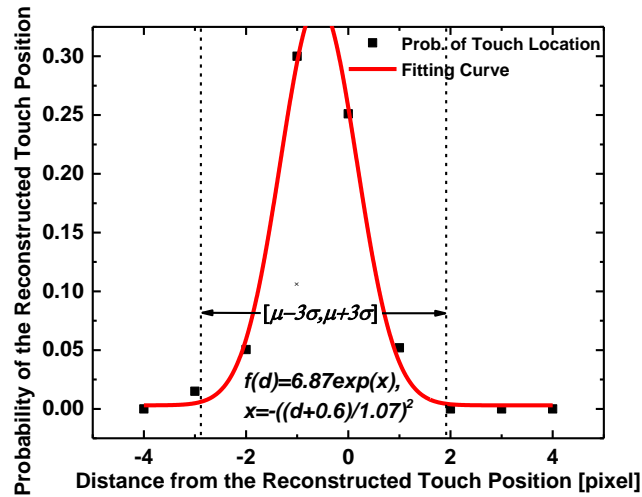
Figure 6.20 (a) original swipe touch based frame, (b) down-sampled touch signal, (c) reconstructed touch signal by using low-pass spatial filtering, (d) regional scanned touch signal.

above, commercial embedded processors achieve a power efficiency of over 20 MIPS/mW, which means that the power consumption is around  $25 \mu\text{W}$ . The energy required for measuring one sensor is approximately  $1/30 \mu\text{J}$ . For the experiment test-bed, the power consumption is around 12.8 mW. Therefore, the power consumption of the compressive sensing reconstruction is insignificant. If only 30% of the electrodes are measured, then around 8.79 mW can be saved. As for the fixed pattern based down-sampling technique, the algorithm complexity is lower than the random pattern based technique, thus the discussion is neglected.

If touch information is the most important consideration then iterations of regional scans can be performed to obtain more detailed information. For example, our experiment was carried out on an  $80 \times 80$  touch screen panel with a scan rate of 60 Hz,



(a)



(b)

Figure 6. 21 (a) Distribution of the reconstructed touch positions; X-Y coordinates indicate the distance between the reconstructed touch position and original touch position. (b) The cross-section with the largest variance of (a).

thus around 2.6  $\mu\text{s}$  was required to read one sensor. If in the down-sampled stage 50% of the sensors are measured, roughly 8.4 ms is needed to use the reconstruction algorithm, after which the rest of the time can be used for a regional scan. One regional scan takes about 0.2 ms, thus during one touch event approximately 40 regional scans

can be performed. As more time is used to read the sensors, noise can be averaged. The above relationship can be expressed as:

$$T_{Frame} \geq T_{Down-sampled} + M_{Touch} N_{Times} N_{Regiona-scan} T_{Sensor} ; \quad (6.20)$$

where  $T_{Frame}$  is the time to scan the original frame (e.g. 16.7 ms in this paper),  $T_{Down-sampled}$  the time to read the down-sampled sensors and  $T_{Sensor}$  the time to measure one sensor.

It should be noted that stylus touches were used in our experiments (multi-pad and rows-and-columns), which cover more sensors than a typical finger touch (e.g. 3×3). The radius of the regional scan area for a finger touch can be limited to 1 pixel. Details of this are currently being investigated.

## 6.4 Conclusion

Capacitive touch signal detection is a key factor in both 3D (force) touch detection and 2D (x-y) touch detection. Thus the quality of capacitive signal detection is of significant meaning. Here, quality mainly refers to two performance metrics: detection accuracy and readout speed. In this chapter, the SNR of the capacitive touch signal is boosted by 15.6 dB by using correlated double sampling and spatial low-pass filtering related techniques, indicating improved detection accuracy. In terms of the readout speed, fixed pattern and random pattern related down-sampling techniques are applied, giving rise to reductions in both readout time and power consumption.

## Bibliography

- [1] Gao, S., Lai, J., Micou, C. and Nathan, A., 2016. Reduction of common mode noise and global multivalued offset in touch screen systems by correlated double sampling. *Journal of Display Technology*, 12(6), pp.639-645.
  
- [2] Hotelling, S., Strickon, J.A. and Huppi, B.Q., Apple Inc., 2010. *Multipoint touchscreen*. U.S. Patent 7,663,607.
  
- [3] Baharav, Z. and Kakarala, R., 2011, February. Capacitive touch sensing: signal and image processing algorithms. In *IS&T/SPIE Electronic Imaging* (pp. 78730H-78730H). International Society for Optics and Photonics.
  
- [4] Mohamed, M.G.A., Jang, U., Seo, I., Kim, H., Cho, T.W., Chang, H.K. and Lee, S., 2014, June. Efficient algorithm for accurate touch detection of large touch screen panels. In *Consumer Electronics (ISCE 2014), The 18th IEEE International Symposium on* (pp. 1-2). IEEE.
  
- [5] White, M.H., Lampe, D.R., Blaha, F.C. and Mack, I.A., 1974. Characterization of surface channel CCD image arrays at low light levels. *IEEE Journal of Solid-State Circuits*, 9(1), pp.1-12.
  
- [6] Enz, C.C. and Temes, G.C., 1996. Circuit techniques for reducing the effects of op-amp imperfections: autozeroing, correlated double sampling, and chopper stabilization. *Proceedings of the IEEE*, 84(11), pp.1584-1614.
  
- [7] Ohta, J., 2007. *Smart CMOS image sensors and applications*. CRC press.

- [8] Ahn, Y.S., Ahn, T.J., Lee, K. and Kang, J.K., 2014. Avoiding noise frequency interference with binary phase pulse driving and CDS for capacitive TSP controller. *IEICE Electronics Express*, 11(21), pp.20140837-20140837.
- [9] Souchkov, V., Pixart Imaging Inc., 2012. *Capacitive touchscreen signal acquisition without panel reset*. U.S. Patent 8,274,491.
- [10] Lim, D.H., Lee, S.Y., Choi, W.S., Park, J.E. and Jeong, D., 2012. A digital readout IC with digital offset canceller for capacitive sensors. *J. Semicond. Technol. Sci*, 12, pp.278-85.
- [11] Park, J.E., Lim, D.H. and Jeong, D.K., 2013, November. A 6.3 mW high-SNR frame-rate scalable touch screen panel readout IC with column-parallel  $\Sigma$ - $\Delta$  ADC structure for mobile devices. In *Solid-State Circuits Conference (A-SSCC), 2013 IEEE Asian* (pp. 357-360). IEEE.
- [12] Lowles, R.J., Robinson, J.A. and Wu, K., Research In Motion Limited, 2008. *System and method of integrating a touchscreen within an LCD*. U.S. Patent 7,388,571.
- [13] Yang, J.H., Jung, S.C., Woo, Y.J., Jeon, J.Y., Lee, S.W., Park, C.B., Kim, H.S., Ryu, S.T. and Cho, G.H., 2010, September. A novel readout IC with high noise immunity for charge-based touch screen panels. In *Custom Integrated Circuits Conference (CICC), 2010 IEEE* (pp. 1-4). IEEE.
- [14] Middleton, A., Rella, B., Kim, H. J., Baily, M., Coleman, A. and Garavuso, G, 2012. FTIR multi-touch screen technology. *Rochester Institute of Technology*. Project No. P12302.

- [15] Aras, S., Nihei, T. and Rahman, A, 2011, Jan. Touch sensing method and apparatus, U.S. Patent 20130015867 A1.
- [16] Nys, O., Ballan, H., Chappatte, N. and Vuadens, F., Advanced Silicon Sa, 2015. *Circuit for capacitive touch applications*. U.S. Patent 8,970,227.
- [17] Ballan, H., Chappatte, N., Nys, O. and Vuadens, F, 2012, Mar. Circuit for capacitive touch applications. W.O. Patent WO2012034714 A1.
- [18] Guedon, Y., Tan, K.B., Ningrat, K.A. and Guo, D., Stmicroelectronics Asia Pacific Pte Ltd, 2016. *Capacitive sensing analog front end*. U.S. Patent 9,244,569.
- [19] Cypress Semiconductor Corp. “Using correlated double sampling to reduce offset, drift and low frequency noise”, [Online]. Available: <http://www.cypress.com/?rID=2894>
- [20] Korobeynikov, O., Kulinets, J.M., Protasov, V. and Nuytkens, P.R., Custom One Design, Inc., 2008. *Methods and apparatus for reducing non-ideal effects in correlated double sampling compensated circuits*. U.S. Patent Application 12/113,731.
- [21] Bussat, J.M. and Hotelling, S.P., Apple Inc., 2015. *Redundant sensing element sampling*. U.S. Patent 9,035,895.
- [22] Luo, C., Borkar, M.A., Redfern, A.J. and McClellan, J.H., 2012. Compressive sensing for sparse touch detection on capacitive touch screens. *IEEE Journal on Emerging and Selected Topics in Circuits and Systems*, 2(3), pp.639-648.
- [23] ARM, “Cortex-a5 processor performance”, [Online]. Available: <http://www.arm.com/products/processors/cortex-a/cortex-a5.php>.

- [24] Westerman, W., Hotelling, C. S., 2010, Jan. Peripheral pixel noise reduction. U.S. Patent US7643010 B2.
- [25] Hotelling, S., Strickon, J.A., Huppi, B.Q., Chaudhri, I., Christie, G., Ording, B., Kerr, D.R. and Ive, J.P., Apple Inc., 2013. *Gestures for touch sensitive input devices*. U.S. Patent 8,479,122.
- [26] Land, B.R. and Hotelling, S.P., Apple Inc., 2010. *Error compensation for multi-touch surfaces*. U.S. Patent 7,692,638.
- [27] Akhtar, H. and Kakarala, R., 2014. A methodology for evaluating accuracy of capacitive touch sensing grid patterns. *Journal of Display Technology*, 10(8), pp.672-682.
- [28] Wang, T.Y., Ko, Y.R. and Lai, C.C., Novatek Microelectronics Corp., 2012. *Gesture detecting method capable of filtering panel mistouch*. U.S. Patent Application 13/350,826.
- [29] Hagermoser, S., 2014. Harnessing the power of projected capacitive technology using unfiltered touchscreen data. *3M Touch Systems*.
- [30] Jordan, J., Synaptics Incorporated, 2012. *Sensing and defining an input object*. U.S. Patent 8,269,511.
- [31] Guarneri, I., Capra, A., Farinella, G.M. and Battiato, S., 2013, March. Shape recognition for capacitive touch display. In *IS&T/SPIE Electronic Imaging* (pp. 86610R-86610R). International Society for Optics and Photonics.

- [32] Westerman, W.C., Apple Inc., 2016. *Image jaggedness filter for determining whether to perform baseline calculations*. U.S. Patent 9,372,576.
- [33] Westerman, W.C., Apple Inc., 2012. *Multi-touch input discrimination*. U.S. Patent 8,243,041.
- [34] Guarneri, I., Capra, A., Castorina, A., Battiato, S. and Farinella, G.M., 2013, January. PCA based shape recognition for capacitive touch display. In *Consumer Electronics (ICCE), 2013 IEEE International Conference on* (pp. 596-597). IEEE.
- [35] Yang, J.H., Jung, S.C., Son, Y.S., Ryu, S.T. and Cho, G.H., 2013. A noise-immune high-speed readout circuit for in-cell touch screen panels. *IEEE Transactions on Circuits and Systems I: Regular Papers*, 60(7), pp.1800-1809.
- [36] Hotelling, S.P., Amm, D.T., Lammers, M., Orchard, J.T., King, B.M., Leung, O. and Teoman, D., Amm David T and Orchard John T, 2009. *Ground detection for touch sensitive device*. U.S. Patent Application 12/504,639.
- [37] Lee, H.S., Park, T.J. and Kim, K.J., Samsung Electro-Mechanics Co., Ltd., 2013. *Touch sensing method and touch sensing device*. U.S. Patent Application 13/764,042.
- [38] Zhang, J., Guo, Y. and Mo, L., Focaltech Systems Ltd., 2011. *Multi-touch detection method for capacitive touch screens*. U.S. Patent Application 13/065,024.
- [39] Land, B.R., Yousefpor, M. and Hotelling, S.P., Apple Inc., 2013. *Negative pixel compensation*. U.S. Patent 8,482,544.

- [40] Liu, J.M., Liu, L.L., Chang, C.W. and Tai, S.F., Himax Technologies Limited, 2012. *Touch device and driving method of touch panel thereof*. U.S. Patent Application 13/686,046.
- [41] Philipp, H., 2002. *Capacitive sensor and array*. U.S. Patent 6,452,514.
- [42] Hwang, T.H., Cui, W.H., Yang, I.S. and Kwon, O.K., 2010. A highly area-efficient controller for capacitive touch screen panel systems. *IEEE Transactions on Consumer Electronics*, 56(2).
- [43] Yang, J.H., Choi, J.M., Kim, Y.S. and Oh, H.S., Silicon Works Co., Ltd., 2013. *Control circuit of touch screen and noise removing method*. U.S. Patent Application 13/869,784.
- [44] McAndrew, A., 2004. An introduction to digital image processing with matlab notes for scm2511 image processing. *School of Computer Science and Mathematics, Victoria University of Technology*, pp.1-264.
- [45] Jensen, J.R. and Lulla, K., 1987. *Introductory digital image processing: a remote sensing perspective*.
- [46] Russ, J.C., Matey, J.R., Mallinckrodt, A.J. and McKay, S., 1994. The image processing handbook. *Computers in Physics*, 8(2), pp.177-178.
- [47] Lim, J.S., 1990. *Two-dimensional signal and image processing*. Englewood Cliffs, NJ, Prentice Hall, 1990, 710 p.
- [48] Lee, J.S., 1980. Digital image enhancement and noise filtering by use of local statistics. *IEEE transactions on pattern analysis and machine intelligence*, (2), pp.165-168.

- [49] Lustig, M., Donoho, D.L., Santos, J.M. and Pauly, J.M., 2008. Compressed sensing MRI. *IEEE signal processing magazine*, 25(2), pp.72-82.
- [50] Tsaig, Y. and Donoho, D.L., 2006. Extensions of compressed sensing. *Signal processing*, 86(3), pp.549-571.
- [51] Figueiredo, M.A., Nowak, R.D. and Wright, S.J., 2007. Gradient projection for sparse reconstruction: Application to compressed sensing and other inverse problems. *IEEE Journal of selected topics in signal processing*, 1(4), pp.586-597.
- [52] Baraniuk, R.G., 2007. Compressive sensing [lecture notes]. *IEEE signal processing magazine*, 24(4), pp.118-121.
- [53] Luo, C., McClellan, J., Borkar, M. and Redfern, A., 2012, March. Sparse touch sensing for capacitive touch screens. In *Acoustics, Speech and Signal Processing (ICASSP), 2012 IEEE International Conference on* (pp. 2545-2548). IEEE.
- [54] Chenchi, L.U.O., Borkar, M.A. and Redfern, A.J., Texas Instruments Incorporated, 2014. *System and method for sparse touch sensing on capacitive touch screen*. U.S. Patent 8,692,801.
- [55] Yaghoobi, M., McLaughlin, S. and Davies, M.E., 2013. Super-resolution sparse projected capacitive multitouch sensing.

# Chapter 7 Conclusion

---

This chapter summarizes the work that has been done in this study, which includes: a review of piezoelectric materials and capacitive touch panel related techniques; a theoretical analysis of the proposed technique, from aspects of the mechanical and electrical properties; fabrication and measurement of the graphene and PVDF based multi-functional touch panel; interpretation algorithms for force touch detection, and optimization algorithms for capacitive touch detection. Finally, this chapter ends with a brief discussion of a number of recommendations for future work, based on the results obtained from this work.

## 7.1 Conclusion

This dissertation has presented a multi-functional capacitive touch panel for multi-dimensional sensing. The properties of piezoelectric materials, techniques related to capacitive touch panels, theoretical analysis of the mechanical and electrical properties of the multi-functional touch panel, touch panel fabrication and measurement, and interpretation and optimization algorithms, have been discussed.

Design considerations for detecting force touch in capacitive touch panels were discussed based on the literature review of piezoelectric materials and techniques related to capacitive touch panels. From the discussion, we learned that the characteristics of capacitive touch panels, such as pre-stress, temperature and environmental EMI, don't strongly affect the accuracy of force touch detection. In contrast, the characteristics of force touch events, such as force touch speed, touch direction and finger geometry can heavily influence the detection accuracy. These design considerations are of significant meaning in designing and calibrating a piezoelectric material based touch panel.

A theoretical analysis was conducted in terms of the mechanical and electrical properties of the proposed multi-functional touch panel. In the mechanical analysis, four widely used capacitive touch panel stack-ups were investigated. From the investigation, we learned that the proposed technique can provide enhanced z-axis touch detection resolution and sensitivity compared to the existing force touch technique, which relies on changes to force induced capacitance. In the electrical analysis, both the readout SNR and the frequency property of the force touch signal were studied. A high SNR of 59.1 dB was obtained based on the theoretical SNR estimation, indicating high detection accuracy. From analysis of the frequency of the force touch signal, we learned that conventional tapping force touches occupy the frequency band with 10 kHz, thus can be separated from capacitive excitation signals which are normally above 90 kHz in capacitive touch panels.

After the theoretical analysis, a multi-functional touch panel was fabricated. To ensure that the fabricated multi-functional touch panel has good flexibility, graphene electrodes were selected and grown by the conventional CVD method. Two types of measurements (capacitive and force touch measurement) were performed. In the capacitive touch measurement, the minimum changed capacitance value was 0.2 pF, indicating a good detection resolution. In the force touch measurement, the force-voltage sensitivity was 92 mV/N, satisfying applications where high force touch sensitivity is needed.

A touch panel system was then assembled. Two force touch detection issues related to piezoelectric materials were addressed by employing information provided by capacitive touch signals. More specifically, static force touch detection and propagated stress elimination were achieved by incorporating the presence of capacitive touch signals. The capacitive touch signal is very important for interpreting force touch signals. Optimization algorithms were developed in terms of SNR and readout speed. The numerical and experimental results showed that, after CDS and Spatial LPF related

noise reduction techniques were used, the SNR was boosted by 15.6 dB. Using down-sampling related techniques, the readout time was reduced by 11.3 ms.

## **7.2 Future Work**

The aim of this work was to design a multi-functional touch panel for concurrent multi-dimensional sensing for interactive displays, to provide customers with a new and advanced user experience. However, due to time limits and facility constraints, there are still additional tasks that need to be undertaken to further increase the performance of the system. Recommendations are given here as part of this future work.

As described in this dissertation, non-uniformity of force touch detection over the panel scale limits the resolution of force touch detection. One way to solve this issue is to model the relationship between the location of a force touch and the architecture and geometry of the touch panel, which requires deeper mechanical analysis and plenty of experiments. Furthermore, absolute force touch detection has not yet been achieved, due to the existence of triboelectricity. To address this, the mechanism and characteristics of triboelectric noise need to be investigated.

# Publications

## Journal Publications

- [1] **Gao, S.**, Wu, X., Ma, H., Robertson, J. and Nathan, A., 2017. Ultrathin Multi-functional Graphene-PVDF Layers for Multi-dimensional Touch Interactivity for Flexible Displays. *ACS Applied Materials & Interfaces*, 9(22), pp.18410-18416.
  
- [2] Nathan, A. and **Gao, S.**, 2016. Interactive Displays: The Next Omnipresent Technology [Point of View]. *Proceedings of the IEEE*, 104(8), pp.1503-1507.
  
- [3] **Gao, S.**, Arcos, V. and Nathan, A., 2016. Piezoelectric vs. Capacitive Based Force Sensing in Capacitive Touch Panels. *IEEE Access*, 4, pp.3769-3774.
  
- [4] **Gao, S.**, Lai, J. and Nathan, A., 2016. Fast Readout and Low Power Consumption in Capacitive Touch Screen Panel by Downsampling. *Journal of Display Technology*, 12(11), pp.1417-1422.
  
- [5] **Gao, S.**, McLean, D., Lai, J., Micou, C. and Nathan, A., 2016. Reduction of noise spikes in touch screen systems by low pass spatial filtering. *Journal of Display Technology*, 12(9), pp.957-963.
  
- [6] **Gao, S.**, Lai, J., Micou, C. and Nathan, A., 2016. Reduction of common mode noise and global multivalued offset in touch screen systems by correlated double sampling. *Journal of Display Technology*, 12(6), pp.639-645.

## Conference Publications

- [1] **Gao, S.** and Nathan, A., 2017. Augmenting Capacitive Touch with Piezoelectric Force Sensing. Accepted in *SID Symposium Digest of Technical Papers* .

[2] **Gao, S.** and Nathan, A., 2016, May. P-180: Force Sensing Technique for Capacitive Touch Panel. *SID Symposium Digest of Technical Papers* (Vol. 47, No. 1, pp. 1814-1817).

## **Patent Articles**

[1] A. Nathan, **S. Gao** and J. Lai, 2016. Processing Signals from A Touchscreen Panel. PCT/GB2016/053489, US20170139527 A1, May 18, 2017.

[2] **S. Gao**, A. Nathan and J. Lai, 2017. Touchscreen Panel Signal Processing. PCT/GB2017/050156, US20170228096 A1, Aug 10, 2017.

# Appendix I

Derivation of Eq 3.1 and Eq3.2

Following sign convention will be followed:

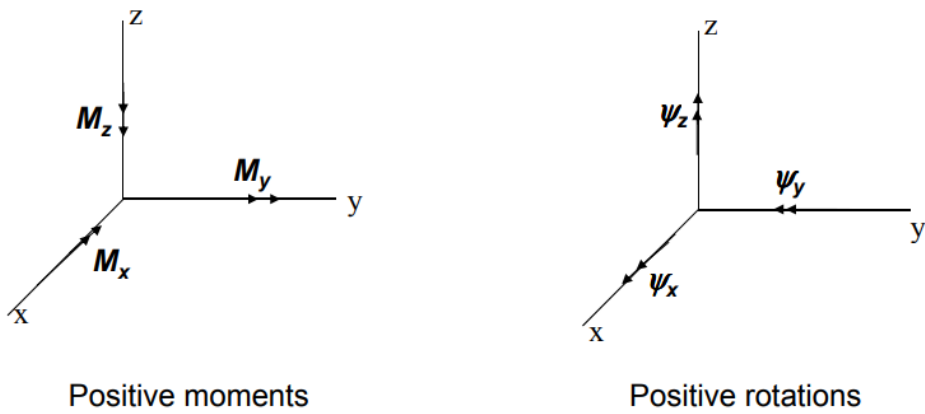


Figure Appendix 1. Definition of positive moments and rotations.

When deformation in  $x$  and  $y$  directions

$$u(x,y,z) = -z\Psi_y(x,y)$$

$$v(x,y,z) = -z\Psi_x(x,y)$$

when vertical deformation takes place:

$$w = w(x,y)$$

As explained in Chapter 3, an assumption for thin plate is that the out of plane shear strain is negligible. Hence,

$$\gamma_{xz} = \partial u / \partial z + \partial w / \partial x = 0$$

as

$$\gamma_{xz} = -\Psi_y + \partial w / \partial x = 0$$

hence

$$\Psi_y = \partial w / \partial x$$

$$\gamma_{yz} = \partial v / \partial z + \partial w / \partial y = 0$$

as

$$\gamma_{yz} = -\Psi_x + \partial w / \partial y = 0$$

hence

$$\Psi_x = \partial w / \partial y$$

For non-zero strains:

$$\varepsilon_{xx} = \partial u / \partial x = -z \partial \Psi_y / \partial x = -z \partial^2 w / \partial x^2$$

$$\varepsilon_{yy} = \partial v / \partial y = -z \partial \Psi_x / \partial y = -z \partial^2 w / \partial y^2$$

$$\gamma_{yz} = \partial u / \partial y + \partial v / \partial x = -2z \partial^2 w / \partial x \partial y$$

For thin plate, when out of plane shear strains vanish, the out of plane shear stresses also vanish:

$$\tau_{xz} = 0, \tau_{yz} = 0,$$

The out of plane normal stress is also assumed to be zero.

Non-zero stress components can be described as shown Fig. A2,

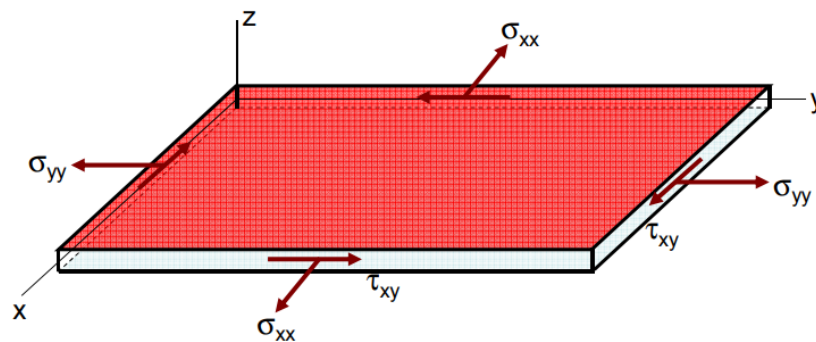


Figure Appendix 2. All three in plane stress components.

If we assume the thin plate is linear elastic isotropic, then three stress and strain components can be written as:

$$\varepsilon_{xx} = \sigma_{xx}/E - \nu\sigma_{yy}/E$$

$$\varepsilon_{yy} = \sigma_{yy}/E - \nu\sigma_{xx}/E$$

$$\gamma_{yz} = \tau_{xy}/G = 2(1+\nu)\tau_{xy}/E$$

expressed in matrix form

$$\begin{pmatrix} \sigma_{xx} \\ \sigma_{yy} \\ \tau_{xy} \end{pmatrix} = \frac{E}{1-\nu^2} \begin{bmatrix} 1 & \nu & 0 \\ \nu & 1 & 0 \\ 0 & 0 & \frac{1-\nu}{2} \end{bmatrix} \begin{bmatrix} \varepsilon_{xx} \\ \varepsilon_{yy} \\ \tau_{xy} \end{bmatrix}$$

expressed strains in terms of curvatures:

$$\begin{pmatrix} \sigma_{xx} \\ \sigma_{yy} \\ \tau_{xy} \end{pmatrix} = \frac{-Ez}{1-\nu^2} \begin{bmatrix} 1 & \nu & 0 \\ \nu & 1 & 0 \\ 0 & 0 & \frac{1+\nu}{2} \end{bmatrix} \begin{bmatrix} \frac{\partial^2 \omega}{\partial x^2} \\ \frac{\partial^2 \omega}{\partial y^2} \\ 2 \frac{\partial^2 \omega}{\partial x \partial y} \end{bmatrix}$$

Hence eq 3.2 is obtained.

if assume the point load acts over an infinitesimal area  $u \times v$ , corresponding to uniformly distributed load [xx],

$$q_0 = P/uv$$

we can obtain

$$q_{mn} = \frac{16}{mn} \frac{q_0}{\pi^2} \sin \frac{m\pi x_0}{a} \sin \frac{n\pi y_0}{b} \sin \frac{m\pi u}{2a} \sin \frac{n\pi v}{2b}$$

$$\Rightarrow q_{mn} = \frac{16}{mn} \frac{P}{uv\pi^2} \sin \frac{m\pi x_0}{a} \sin \frac{n\pi y_0}{b} \sin \frac{m\pi u}{2a} \sin \frac{n\pi v}{2b}$$

$$\Rightarrow q_{mn} = \frac{4P}{ab} \sin \frac{m\pi x_0}{a} \sin \frac{n\pi y_0}{b} \begin{pmatrix} \sin \frac{m\pi u}{2a} \\ \frac{m\pi u}{2a} \end{pmatrix} \begin{pmatrix} \sin \frac{n\pi v}{2b} \\ \frac{n\pi v}{2b} \end{pmatrix}$$

$$\Rightarrow q_{mn} = \frac{4P}{ab} \sin \frac{m\pi x_0}{a} \sin \frac{n\pi y_0}{b}$$

When deflection is due to a point load

$$w(x, y) = \frac{4P}{\pi^4 abD} \sum_m \sum_n \frac{S'_{mn} \sin \frac{m\pi x}{a} \sin \frac{m\pi y}{b}}{\left[ \left( \frac{m}{a} \right)^2 + \left( \frac{n}{b} \right)^2 \right]^2}$$

$$S'_{mn} = \sin \frac{m\pi x_0}{a} \sin \frac{m\pi y_0}{b}$$

as  $q_{mn} = 16/mn$ , we can obtain

$$w(x, y, \xi, \eta) = \frac{\sum_{n=1}^{\infty} \sum_{m=1}^{\infty} \frac{4}{\pi^4 abD} \sin \frac{n\pi x}{a} \sin \frac{m\pi y}{b} \sin \frac{n\pi \xi}{a} \sin \frac{n\pi \eta}{b}}{\left[ \left( \frac{m}{a} \right)^2 + \left( \frac{n}{b} \right)^2 \right]^2}$$

$$D = \frac{Et^3}{12(1-\nu^2)}$$

hence Eq 3.1 is proved.